Keele University

Hydrodynamic simulations of convection and nucleosynthesis in the late phases of massive stars to constrain and guide stellar evolution theory

Federico Rizzuti

Doctor of Philosophy

December 2023

Abstract

The present knowledge of stellar evolution is still limited today by large uncertainties that derive from the complex multi-dimensional processes occurring in stars. Among them, the turbulent motions of the stellar fluid control the size and evolution of convective zones, deeply affecting the structure and evolution of the star. The weaknesses of the current theories include determining the extent of the convective regions, the amount of mixing at the convective boundaries, and the exact evolution and death of convection.

Convection and its effects are normally included in one-dimensional stellar evolution models by means of simplifying prescriptions, that need to be calibrated from observations or numerical simulations to correctly represent the stellar physics. Hydrodynamic models of stars can improve these prescriptions by studying realistic multi-D processes in great detail, but only for a short time range compared to the entire stellar evolution.

In this thesis, I present the results from three new sets of 3D hydrodynamic simulations, each exploring a different stellar environment, with the aim of studying turbulent motions and nucleosynthesis in convective regions of evolved massive stars. The analysis has been performed by studying both the dynamics of the fluid and the evolution of the chemical abundances. The results show that late convective phases of massive stars present very strong boundary mixing, but the overshooting prescription calibrated from the new 3D data displays a new-found convergence towards 1D models results. The analysis of the abundances and their evolution shows the production and consumption by nuclear reactions, in addition to the transport of species and their dispersion across the layers.

These conclusions help answer some open questions in stellar evolution theory, and they can have an important impact on our understanding of stellar structure and evolution.

Acknowledgements

I wish to express my sincere gratitude to my supervisor Professor Raphael Hirschi, who has been my guiding light throughout the challenges and wonders of my academic and personal journey at Keele, providing much more than simple professional guidance. With patience and generosity, he guided me through the difficult and exciting paths of scientific research, and his example inspires me to pursue a career in the academic world.

This work would have never been possible without the help and support of my exceptional collaborators, who actively contributed to discussing and shaping this work: David Arnett, Cyril Georgy, Casey Meakin, Miroslav Mocák, Alex Murphy, Thomas Rauscher. I am particularly grateful to the members of our collaboration group at Keele University: Laura Scott, Etienne Kaiser, Vishnu Varma, James Keegans.

There is a number of UK and international organizations that have contributed and supported the work I present here in different ways, to whom I express my gratitude: the STFC DiRAC HPC Facility at Durham University; the European cooperation ChETEC COST Action; the European H2020 programme ChETEC-INFRA; the international IReNA AccelNet network for Nuclear Astrophysics.

I finally express my sincere thanks to my family and friends, particularly to my wonderful parents who have always encouraged me to chase my dreams, and to my extraordinary friends and colleagues at Keele, for making my years at Keele truly unforgettable.

Contents

1 Introduction

The term "massive stars" is typically used to refer to stars with mass larger than ~ 8 $M_\odot$ (Smartt et al., 2009). These objects are of great interest for astrophysics, since their large luminosity makes them easy to observe, and they host or take part in a wide range of astrophysical processes, such as nuclear burning and nucleosynthesis, supernova explosions, black hole formation, interaction with other stars and planetary systems.
Therefore, it is crucial that we have a precise understanding and reliable predictions of how massive stars form, evolve and die. Unfortunately, at the moment our knowledge of the physics of massive stars is undermined by a lack of both individual and comprehensive understanding of the many phenomena that take place in stellar interiors. This ignorance results in severe limitations on the predictive power of the stellar evolutionary models.
In this chapter, I will summarize the properties and evolutionary history of massive stars, including their final fate. I will also introduce the topic of convection in massive stars, and the way observations can help improve theoretical research.

1.1 Massive stars and their evolution

Stars are self-gravitating masses of gas: their own gravitational force holds themselves together. Specifically, gravity tends to compress the star, while the force arising from the pressure gradient opposes this compression (see Phillips, 1994). During the formation phase of a star, a mass of gas, mostly molecular hydrogen, is collapsing under its own gravity. The virial theorem relates the potential and kinetic energy of a system of particles, and it states that when the system is contracting half of its gravitational potential is converted into the kinetic energy of its individual components, while the other half is radiated

away. This causes the hydrogen molecules to gain kinetic energy and therefore increase their temperature, until they are dissociated into hydrogen atoms and later into ions, and when the temperature exceeds 10^7 K nuclear hydrogen-burning is enabled in the stellar core, converting hydrogen into helium. The burning becomes possible because the high energy of the nuclei allow them to overcome the repulsive electromagnetic barrier between each other, thanks to the quantum-mechanical tunnelling effect. The thermonuclear fusion that converts hydrogen into helium releases enough energy to oppose the gravitational force and the collapse halts. The star is now in hydrostatic equilibrium, in a phase known as "zero age main sequence" or ZAMS. I show in Fig. 1.1 the stellar evolution in a Hertzsprung-Russell diagram of stars with different initial mass from the non-rotating, solar-metallicity models of Ekström et al. (2012): the starting point of these tracks represents the ZAMS.

All stars spend most of their life burning hydrogen during the main sequence phase. The amount of time it takes them to complete their nuclear burning, i.e. their lifetime, is determined primarily by their mass (see e.g. Ekström et al., 2012). Massive stars contain more hydrogen than low-mass stars, but they also burn it much faster, therefore their lives are shorter (in fact, the stellar luminosity scales approximately as $L \sim M^3$, Phillips, 1994). This is because more massive stars reach higher temperatures in their core and the nuclear rates for hydrogen burning are strongly temperature dependent: $\sim T^4$ for low-mass stars and $\sim T^{18}$ for intermediate and massive stars (Phillips, 1994). Indicatively, non-rotating stars of 1 $M_\odot$ live for 10 Gyr, 10 $M_\odot$ for 20 Myr, 100 $M_\odot$ for 3 Myr (Maeder & Meynet, 1989).

The fate of the star after the main-sequence phase also depends on the stellar mass. The larger the mass, the more advanced burning stages the star can undergo. When stars exhaust hydrogen in their core, which is now mostly composed of helium, the energy released from the nuclear reactions cannot balance the gravitational collapse of the star any longer, so the star begins contracting and it leaves the main sequence (see Salaris & Cassisi, 2005). While the in-

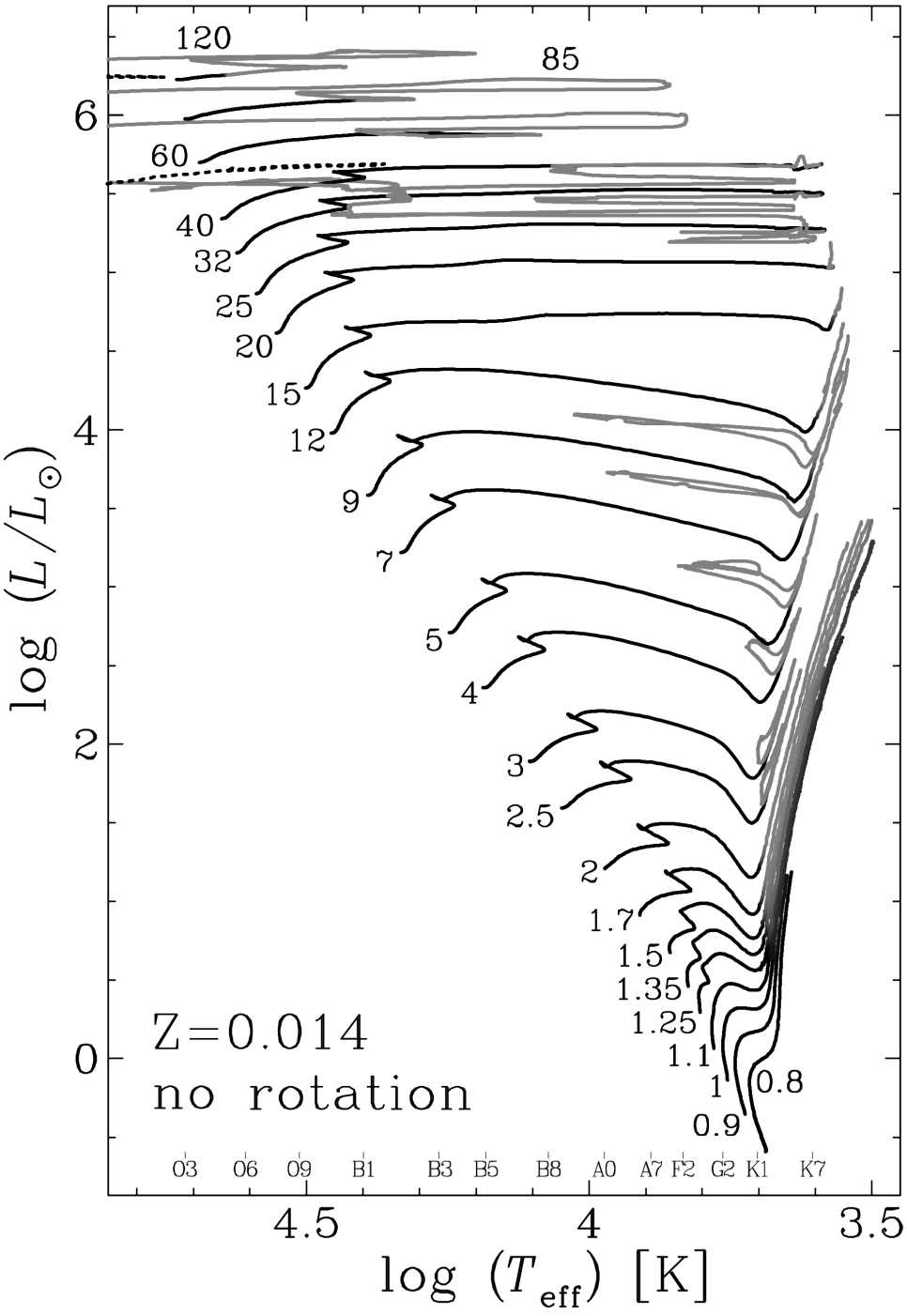

Figure 1.1: Hertzsprung-Russell diagram for stellar models with different initial mass, zero rotation and solar metallicity. Adapted from Ekström et al. (2012).

ner layers are contracting, the temperature of the hydrogen shell immediately above the helium core starts increasing, and therefore nuclear reactions occur again. This release of energy heats the outer layers of the star and determines their expansion, increasing the luminosity but decreasing the surface temperature of the star. The star then enters the red-giant phase. If the stellar mass is smaller than 0.5 $M_\odot$ this is the end of its life: its outer envelope is expelled and it ends its life as a helium white dwarf. However, the lifetime of such small stars is expected to be longer than the age of the Universe, therefore probably no star has reached this phase yet.

If the stellar mass is larger than 0.5 $M_\odot$, the central temperature keeps rising until at 10^8 K helium is ignited in the core, with helium converted into carbon and oxygen. If the mass is < 2 $M_\odot$ the ignition takes place explosively in the degenerate core, and this is known as a "helium flash", with the possibility of an off-centre ignition (see e.g. Mocák et al., 2010). Otherwise, for more massive stars the core is not degenerate so the helium ignition does not exhibit a flash. Now the nuclear energy released in the core counterbalances the gravitational pressure once more, so the star is again in a stable phase burning helium in its core and hydrogen in a thin shell surrounding the core. When this phase is over, the star is left with a carbon-oxygen core. If $M \lesssim 8$ $M_\odot$, the star does not reach a temperature sufficient to ignite carbon in the core, so the last burning phase is a double-shell burning phase that takes place in a helium and a hydrogen shell above the core. This is known as the "asymptotic-giant-branch" (AGB) phase. Finally, the star dies as a carbon-oxygen white dwarf, expelling its envelope as a planetary nebula, and enriching the interstellar medium with freshly-synthesized elements.

On the other hand, if the star is massive ($M \gtrsim 8$ $M_\odot$), after the helium-burning phase the core temperature approaches 5×10^8 K and triggers the following burning phase, carbon burning. As the evolution proceeds, neutrino losses start replacing radiation as the main energy transport mechanism, becoming dominant for $T > 5 \times 10^8$ K (Arnett, 1996) i.e. since carbon ignition

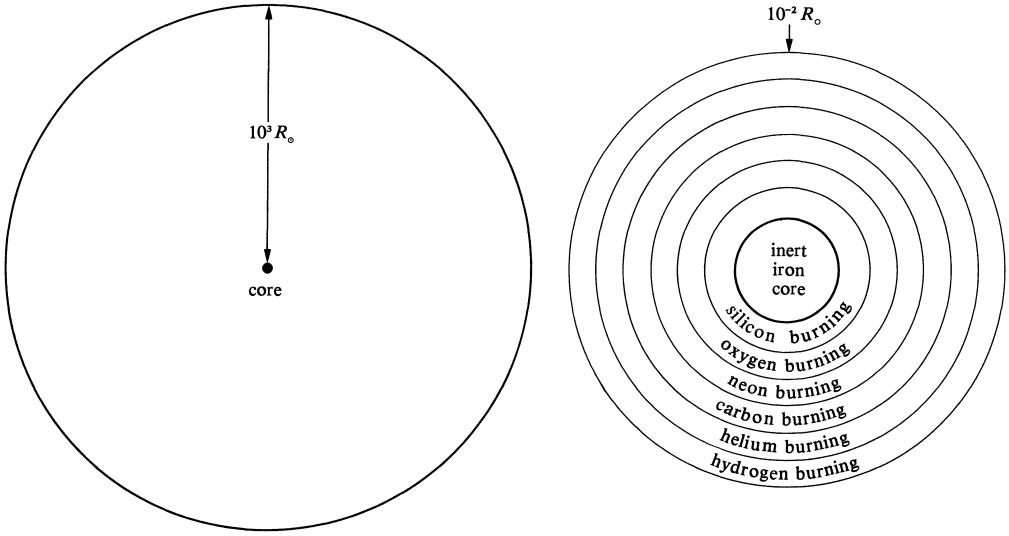

Figure 1.2: "Onion-ring" structure of a pre-supernova star: on the left, a representation of the entire star; on the right, the shell-burning regions surrounding the inert iron core, a volume contained entirely within the core shown on the left. Figure taken from Shu (1982).

(see Limongi et al., 2000), determining an acceleration in the stellar evolution. Stars above 8 $M_\odot$ evolve following all the advanced burning stages after carbon burning, including neon burning ($T > 10^9$ K), oxygen burning ($T > 2 \times 10^9$ K) and silicon burning ($T > 3 \times 10^9$ K) (see Salaris & Cassisi, 2005). This evolution is so rapid that the outer layers do not have time to adjust to the changes in the stellar interiors. Therefore, it is extremely difficult to constrain these phases with observations. At this point, the star presents the typical "onion-ring" structure, where the core is surrounded by concentric shells of different chemical composition, that can host different shell-burning stages. This is shown in Fig. 1.2, where the shell-burning structure of a massive star is schematically represented; it is important to note the actual dimensions of the core and the shells compared to the rest of the star, which consists mostly of an inert hydrogen envelope.

At the end of silicon burning, the star achieves the so-called "nuclear statisti-

Table 1.1: The nuclear burning stages of a 25 $M_\odot$ star and relevant properties: nuclear burning time-scale, central temperature and density, main ashes. Adapted from Phillips (1994), who takes the data from Rolfs & Rodney (1988).

Stage	Time-scale	Temperature (K)	Density (kg m^{-3})	Products
Hydrogen burning	7 Myr	6.0×10^7	5×10^4	Helium
Helium burning	0.5 Myr	2.3×10^8	7×10^5	Carbon, oxygen, neon
Carbon burning	600 yr	9.3×10^8	2×10^8	Neon, sodium, magnesium
Neon burning	1 yr	1.7×10^9	4×10^9	Oxygen, magnesium, silicon
Oxygen burning	6 months	2.3×10^9	1×10^{10}	Magnesium to sulphur
Silicon burning	1 day	4.1×10^9	3×10^{10}	Iron-peak elements

cal equilibrium" (NSE), when all nuclear reactions are perfectly balanced with their inverses, without generating any net product (a small flow can still occur but it is much smaller than either the forward or reverse rate, see Weaver, Zimmerman & Woosley, 1978). The NSE marks the end of the evolution of a massive star, followed only by its conclusive fate. I summarize in Table 1.1 the burning stages of a massive star alongside their most important properties.

1.2 The fate of massive stars

I mentioned that stars with $M \lesssim 8$ $M_\odot$ end their lives as white dwarfs after their nuclear burning phases. The fate of more massive stars is different. Silicon burning produces elements up to the iron peak as ashes, resulting in the formation of an iron core. These elements cannot undergo further nuclear burning, because they have the largest binding energy per nucleon among all elements (Fewell, 1995), as shown in Fig. 1.3. This means that the nuclear fusion of the iron-peak elements requires more energy than that released (except for neutron capture processes, which are not energetic enough to support the

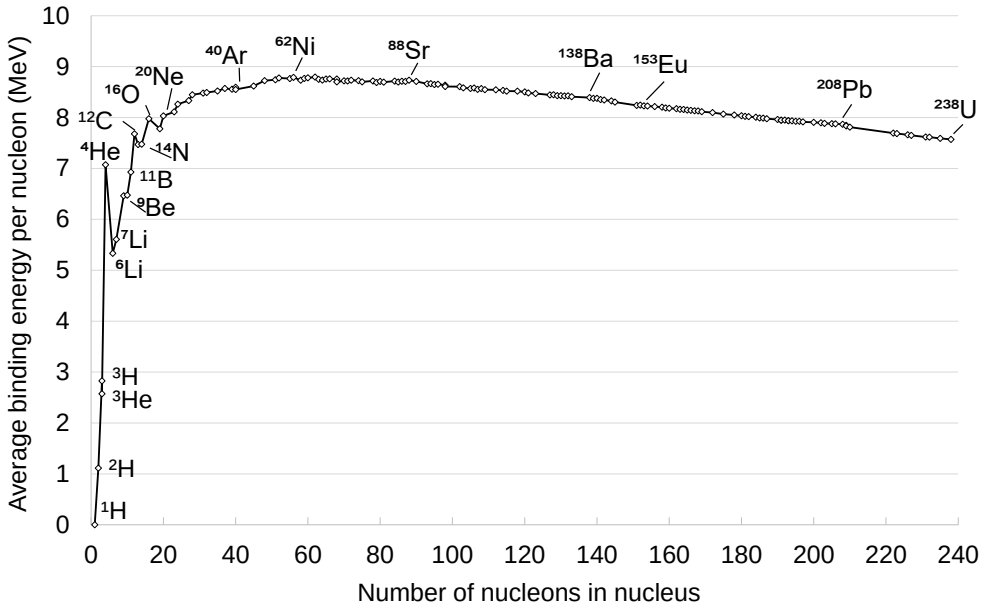

Figure 1.3: Binding energy curve: average binding energy per nucleon versus atomic mass number. Some important isotopes are highlighted. ^{62}Ni has the largest binding energy per nucleon, making it the most stable (Fewell, 1995).

star), making it impracticable and marking this as the endpoint of stellar nuclear burning. Initially, the iron core can sustain the star thanks to the pressure coming from the gas of degenerate electrons, a state of matter characterized by such high density that the greatest contribution to its pressure is given by the Pauli exclusion principle. However, as the iron core mass grows larger, the degenerate electron gas becomes increasingly relativistic, until it reaches the ultrarelativistic limit and cannot sustain the core any longer. This happens when the core mass reaches the "Chandrasekhar limit" (Chandrasekhar, 1931), calculated by equating the pressure from the relativistic degenerate electron gas to the one from the gravitational potential in hydrostatic equilibrium state, and obtaining $M_{\rm Ch} = 5.73\ \mu_{\rm e}^{-2}\ {\rm M}_\odot$ (Chandrasekhar, 1935), where $\mu_{\rm e}$ is the mean molecular weight per electron. In case of an iron core, made of heavy nuclei with approximately two nucleons per electron, $\mu_{\rm e} = 2$ and therefore $M_{\rm Ch} = 1.4\ {\rm M}_\odot$. Beyond this limit, the iron core starts collapsing and other physical processes take over.

The extremely high temperatures reached in the collapsing core ($T > 7 \times 10^9$ K) trigger the photodisintegration of the iron nuclei into α-particles, and the latter into free neutrons and protons (see Phillips, 1994), according to:

$$\gamma + {}^{56}{\rm Fe} \rightarrow 13\ {}^{4}{\rm He} + 4n \tag{1.1}$$

$$\gamma + {}^{4}{\rm He} \rightarrow 2p + 2n \tag{1.2}$$

The extreme density in the core ($\varrho \sim 10^9$ g cm^{-3}) also compresses the proton-electron gas in the core and enables the conversion of protons into neutrons ("neutronization") according to electron capture:

$$e^- + p \rightarrow n + \nu_e \tag{1.3}$$

The net effect is that the iron core is converted into a non-degenerate gas of neutrons, which becomes degenerate as density increases. The free neutrons do not decay into protons as it happens in normal conditions, because

the high density and low kinetic energy of the gas prevent the release of free electrons. Both photodisintegration and neutronization are endothermic processes, the former absorbing kinetic energy to unbind nuclei and the latter releasing neutrinos that carry away the kinetic energy. This reduces the pressure and accelerates the gravitational collapse of the stellar core (see Weaver et al., 1978; Langanke et al., 2003).

When density gets larger than 10^{14} g cm^{-3}, a value comparable with the nuclear density, the neutron gas becomes incompressible due to the repulsive component of the strong interaction at short distances, and the core collapse halts (see Arnett, 1996). The fate of the core now depends on its mass: if this is smaller than the limit of stability for a degenerate neutron gas, the core ends its life as a neutron star, whose structure can be seen as an enormous nucleus of neutrons; otherwise, the collapse continues and the core, subject to extreme pressure, collapses into a black hole. This limit of stability between neutron stars and black holes, known as the "Oppenheimer-Volkoff mass" (Oppenheimer & Volkoff, 1939), ranges between 1 - 3 $M_{\odot}$, but is very difficult to constrain due to uncertainties in the neutron-gas equation of state at such high density.

I have described so far the fate of the massive-star core, but we shall now see what happens to the rest of the stellar structure. While the core is collapsing, the external layers are contracting as well. But when core collapse halts, these layers impact with the incompressible matter and this produces a shockwave (Colgate et al., 1961; Bethe et al., 1979). In the past, it has been thought that this "core-bounce" mechanism would be sufficient to eject the entire stellar envelope, in a so-called "prompt explosion" scenario that would result in the production of type-II supernovae. However, today we know it is difficult to achieve a successful explosion with such mechanism, because the energy of the shockwave is largely dissipated by the photodisintegration of material through the infalling layers and the emission of neutrinos (Myra & Bludman, 1989; Bethe, 1990).

For these reasons, alternative processes have been suggested in order to explain how core-collapse supernovae are produced. Colgate & White (1966) introduced the "neutrino-powered" explosion mechanism, which is commonly recognised today as one of the most important sources of energy for supernova explosions. Due to the high density of the collapsing core $\varrho \sim 10^{14}$ g cm^{-3}, the neutrinos generated by the neutronization have a mean free path much smaller than the core radius, so scattering processes are very frequent and neutrinos are trapped inside a "neutrinosphere", up to the point where $\varrho \sim 10^{11}$ g cm^{-3} and the interaction with matter becomes negligible, allowing them to finally escape the star. This extremely energetic neutrinosphere is able to revive the shockwave, and even a small fraction of its energy can sustain the explosive event of a core-collapse supernova. However, the details of how these processes actually occur in stars are still largely unknown, due to uncertainties associated with the interplay between neutrinos, convection, the explosion mechanisms and other physical processes (Liebendörfer et al., 2001; Woosley & Janka, 2005; O'Connor & Ott, 2011). Numerical simulations of supernova explosions are currently contributing to shed light on these aspects (Lentz et al., 2015; Janka, Melson & Summa, 2016; Burrows & Vartanyan, 2021).

Finally, it is also possible that sometimes these mechanisms are not successful and an explosion does not take place. In these cases, the core mass continues accreting until the Oppenheimer-Volkoff limit is exceeded and the entire star collapses into a black hole.

1.3 Stellar convection

There is a large number of multi-dimensional processes that shape the life of massive stars; these include rotation, magnetic fields, mass loss, and convection. Among these mechanisms, the primary focus of my work is on stellar

convection.

During most of the stellar lifetime, energy is produced in the core due to nuclear reactions, then it is transported across the star and finally released through the surface in the form of radiation. It is interesting to consider how this energy is transported. Two processes are responsible for energy transport in stars: radiative diffusion and convection (see Kippenhahn et al., 2012). The third fundamental mode of heat transfer, i.e. thermal conduction, is very inefficient during stellar evolution; however, it can play an important role in other high-density stellar environments, such as the degenerate gas of electrons in a white dwarf, or conduction in planets.

Which energy transport mechanisms dominates in a stellar region depends on the properties of the fluid stratification. Convection can only occur in the presence of a force field and a strongly stratified medium. In stars, the force field is provided by gravity, while the temperature gradient indicates the strength of the stratification. For these reasons, the structure of a star is dependent on its mass. During the main sequence, low-mass stars (like the Sun) have radiative cores and convective envelopes, while more massive stars ($M \gtrsim 1.3$ $M_\odot$) have convective cores and radiative envelopes (see Clarke & Carswell, 2007). This is because, even though all stars burn hydrogen in the core during the main sequence, the burning takes place through the proton-proton (pp) chains in low-mass stars and via the carbon-nitrogen-oxygen (CNO) cycle in intermediate and massive stars. As mentioned in Sec. 1.1 (see also Phillips, 1994), the pp chains have a temperature dependence of $\sim T^4$, while the CNO cycle depends on $\sim T^{18}$: this means that the latter generates a very steep temperature gradient in the core. On the other hand, in low-mass-star envelopes it is the partially ionised regions associated with large opacities that produce the steep temperature gradients required to trigger convection. It is also possible to have fully convective stars, in the case of very low mass stars with $M < 0.35$ $M_\odot$ (Chabrier & Baraffe, 1997; Browning, 2008), or pre-MS stars with mass no larger than 3 $M_\odot$, corresponding to the Hayashi line in the

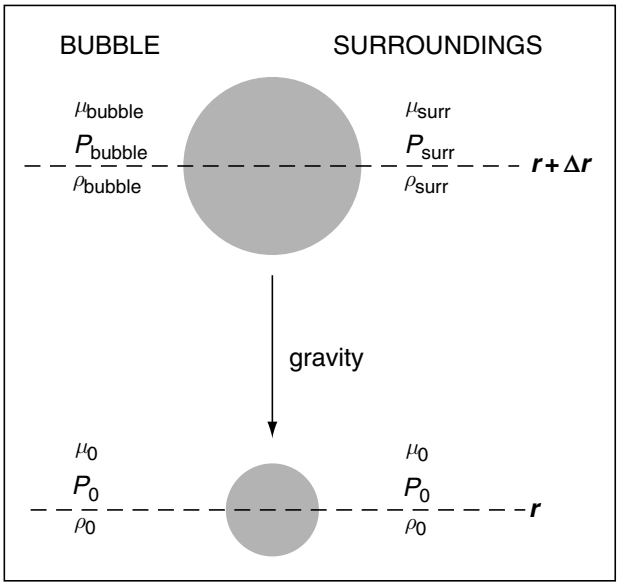

Figure 1.4: Schematic representation of the physical mechanism for the generation of a convective instability. Figure taken from Salaris & Cassisi (2005).

Hertzsprung-Russell diagram (Hayashi, 1961).

We shall now see how a convective instability develops and propagates in a stellar medium (see also Clarke & Carswell, 2007). Let us consider a fluid element from a stratification at hydrostatic equilibrium with a radial temperature gradient and under a uniform gravitational field. This situation is illustrated in Fig. 1.4. If the fluid element, whose density ϱ_0 and pressure P_0 are the same as its surroundings, is displaced upwards by a small distance Δr due to random fluctuations, it would have to change its own density $\varrho_{\rm bubble}$ to be in pressure equilibrium with the surrounding environment ($P_{\rm bubble} = P_{\rm surr}$). Since the moving element would generally not have had time to exchange heat with the surroundings, we can assume that the process is adiabatic. The new density of the fluid element can be either larger or smaller than the one in the new surroundings. In the first case, the element would sink back to its initial

position and the system would be stable against convection. But in the second case, the element would be buoyant and keep rising upwards, so the system is convectively unstable. The element would keep travelling until radiative transport becomes dominant, therefore it cools and is not accelerated upwards any more. This does not imply that the element immediately halts its motion, as we shall later see. Obviously, the same happens if the fluid element is displaced downwards from its original position instead: in this case, a convective instability is triggered if it has larger density than the surroundings.

1.4 Observational constraints

Observational measurements infer quantities derived from the stellar surface. Therefore, it is not trivial to investigate physical processes happening in deep stellar interiors, especially for late phases when the evolution is so rapid that the external layers do not have time to react to the internal changes. The most approachable way of relating theory and observations is through stellar models, where the theoretical knowledge is applied to specific situations and environments. Stellar models follow the evolution of the entire star computing key quantities from the core to the surface, thus producing predictions that can be constrained from observations. As an example, the width of the main sequence for difference mass ranges (Castro et al., 2014) can be used to calibrate the amount of mixing in the convective core (Scott et al., 2021). The chemical abundances measured from stellar atmospheres and in the interstellar medium can also provide constraints to stellar models through galactic chemical evolution studies (Matteucci, 2012; Cescutti et al., 2013; Rizzuti et al., 2019, 2021). Furthermore, observations of supernova light curves, neutrino and γ-ray detections (Woosley & Bloom, 2006) can help understand the stellar structure before the collapse, employing supernova numerical simulations (Müller, 2020).

Recently, information on the inner structure of stars can also be derived from asteroseismic measurements.

1.4.1 Asteroseismology

Asteroseismology is the study and interpretation of stellar pulsations in light curves. This is a powerful tool that can be used to investigate the inner stellar structure. Different types of pulsations can occur in a star, depending on the force that restores the equilibrium: gravity modes (g-modes), pressure modes (p-modes), inertial modes, mixed modes (see Aerts et al., 2019). While p-modes have high frequency and probe regions of space close to the surface, low-frequency g-modes can travel long distances through the radiative medium, probing the deep near-core regions of intermediate and massive stars. Additionally, pulsating stars can have very different properties and nature: from low-mass γ Doradus and δ Scuti variables, to more massive slowly-pulsating B-type (3 - 8 $M_{\odot}$) and β Cephei (up to 25 $M_{\odot}$) stars (see Bowman, 2020). Recently, it has been suggested (Bowman et al., 2019a, 2019b) that nearly all OB-type stars pulsate with low-frequency due to stochastic variability.
In Fig. 1.5, I show as an example the asteroseismic analysis presented in the review of Bowman (2020). The figure describes how it is possible to constrain the interior rotation of a star through gravity modes. The plot on the left presents the light curve of a slowly pulsating star; by computing the amplitude spectrum and fitting the period spacing that decreases with increasing period due to the effects of the Coriolis force (plots on the right), it is possible to measure the rotation rate near the core (see Bowman, 2020 for more details).
More generally, in order to reproduce the observed stellar pulsations, theoretical models of the pulsating star need to be computed. First, the structure of the star is predicted using a 1D stellar evolution model. Then, the pulsation modes are numerically computed with an oscillation code (e.g. `GYRE`, Townsend

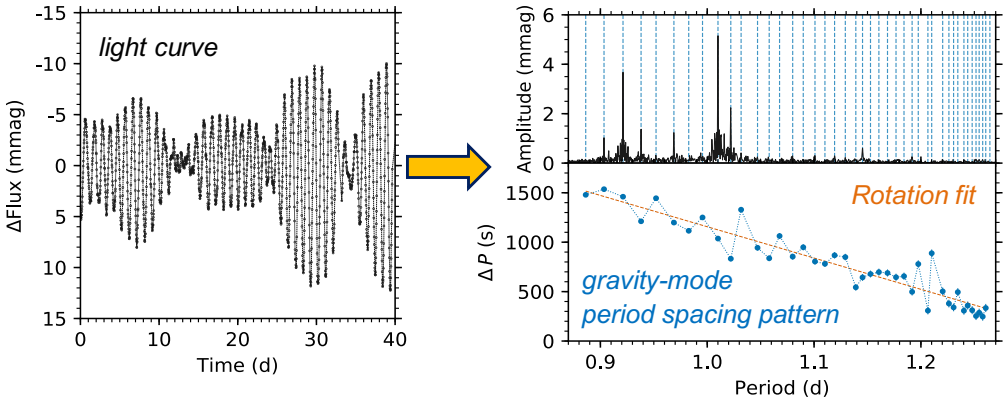

Figure 1.5: Methodology for asteroseismic analysis: light curve of a pulsating star (left panel), amplitude spectrum (right, top) and period spacing (right, bottom). Figure taken from Bowman (2020).

& Teitler, 2013). To estimate the stellar parameters, a grid of 1D models can be produced and compared to the observed pulsations until the best fit is found (e.g. Pedersen et al., 2021). The situation is further complicated by the effects of rotation and magnetic fields on the internal waves. The role of the theoretical studies of stellar evolution in this framework is to improve the 1D models used for asteroseismology, to test the different prescriptions, and to guide the choice of realistic stellar parameters.

2 Theory of convection

In the previous chapter, I presented an overview of the general concepts necessary to appreciate the work of this thesis and place it within the appropriate context. Overall, my work is largely based on the modelling and analysis of convective motions in stellar interiors. It is therefore essential now to review the theory of convection in more detail in order to gain a better understanding of the results presented later.

In this chapter, I show how it is possible to model convective instabilities in stellar environments, with particular attention to their implementation in stellar evolutionary models and the possibility of including additional mixing processes near the convective boundaries.

2.1 A simple treatment of convection

I briefly introduced in Sec. 1.3 the topic of convection in stellar interiors. It is worth now examining the question in a more rigorous way. There is a number of textbooks that describe the approaches and derivations in detail (Salaris & Cassisi, 2005; Kippenhahn et al., 2012). Let us go back to the case of a buoyant fluid element in a steep stratification. We shall now try to solve the equation of motion for an element that was displaced from its original position of equilibrium. Intuitively, we will have to take into account the contributions from the quantities that vary across the stratification, which are temperature T, density ϱ, pressure P, and the chemical composition, all expressed as a function of the stellar radius r. This requires to solve five independent equations including these variables; they later reduce to four equations thanks to the assumption of pressure balance.

To track the chemical composition, the mean molecular weight μ is normally

used, which can be defined as:

$$\mu = \left(\sum_i \frac{x_i \left(1 + Z_i\right)}{A_i} \right)^{-1} \tag{2.1}$$

where x_i, Z_i and A_i are the mass fraction, atomic number and mass number of a species i, respectively.

We have already seen that as a result of a small displacement Δr the fluid element would quickly adjust its pressure to remain in pressure balance with the surroundings, thus a difference of density would arise between the element (e) and the surroundings (s). We can write these two conditions as:

$$\begin{aligned} \Delta P &:= P_\mathrm{e} - P_\mathrm{s} = 0 \\ \Delta \varrho &:= \varrho_\mathrm{e} - \varrho_\mathrm{s} \neq 0 \end{aligned} \tag{2.2}$$

The first equation of our system is the equation of motion for an element of unit volume under a small displacement Δr, given the contribution from gravity and the Archimedean force:

$$\varrho \frac{\mathrm{d}^2 \Delta r}{\mathrm{d}t^2} = -g\varrho_\mathrm{e} + g\varrho_\mathrm{s} = -g\Delta\varrho \tag{2.3}$$

The second equation we use involves the chemical composition, under the assumption that the element does not change its composition but the stratification does:

$$\Delta\mu := \mu_\mathrm{e} - \mu_\mathrm{s} = \left[\left(\frac{\mathrm{d}\mu}{\mathrm{d}r} \right)_\mathrm{e} - \left(\frac{\mathrm{d}\mu}{\mathrm{d}r} \right)_\mathrm{s} \right] \Delta r = -\frac{\mathrm{d}\mu}{\mathrm{d}r} \Delta r \tag{2.4}$$

where by μ we indicate now the composition of the surroundings. If we differentiate with respect to time and introducing the following definitions for the gradient notation and the pressure scale height:

$$\nabla_\mu := \frac{\mathrm{d}\ln(\mu)}{\mathrm{d}\ln(P)}; \quad H_\mathrm{P} := -\frac{\mathrm{d}r}{\mathrm{d}\ln(P)} \tag{2.5}$$

we obtain:

$$\frac{\mathrm{d}\Delta\mu}{\mathrm{d}t} = -\frac{\mathrm{d}\mu}{\mathrm{d}r}\frac{\mathrm{d}\Delta r}{\mathrm{d}t} = -\mu\nabla_\mu \frac{\mathrm{d}\ln(P)}{\mathrm{d}r}\frac{\mathrm{d}\Delta r}{\mathrm{d}t} = \frac{\mu}{H_\mathrm{P}}\nabla_\mu \frac{\mathrm{d}\Delta r}{\mathrm{d}t} \tag{2.6}$$

For the next equation we consider the temperature difference, and assuming that the element is adiabatic, so ignoring any heat loss, we can write:

$$\Delta T := T_{\rm e} - T_{\rm s} = \left[\left(\frac{{\rm d}T}{{\rm d}r}\right)_{\rm e} - \left(\frac{{\rm d}T}{{\rm d}r}\right)_{\rm s}\right]\Delta r \tag{2.7}$$

whose time derivative is, using again the gradient notation $\nabla := \dfrac{{\rm d}\ln(T)}{{\rm d}\ln(P)}$ and indicating $\nabla_{\rm ad}$ as the element and ∇ as the surroundings:

$$\frac{{\rm d}\Delta T}{{\rm d}t} = T\left(\nabla_{\rm ad} - \nabla\right)\frac{{\rm d}\ln(P)}{{\rm d}r}\frac{{\rm d}\Delta r}{{\rm d}t} = -\frac{T}{H_{\rm P}}\left(\nabla_{\rm ad} - \nabla\right)\frac{{\rm d}\Delta r}{{\rm d}t} \tag{2.8}$$

Finally, the last equation that closes our system is the gas equation of state, that we can write in the general form $\varrho = \varrho(P, T, \mu)$ and use it to obtain the differential form:

$$\Delta\varrho = \left(\frac{\partial\varrho}{\partial P}\right)_{{\rm T},\,\mu}\Delta P + \left(\frac{\partial\varrho}{\partial T}\right)_{{\rm P},\,\mu}\Delta T + \left(\frac{\partial\varrho}{\partial\mu}\right)_{{\rm P},\,{\rm T}}\Delta\mu \tag{2.9}$$

from which we derive, keeping in mind that $\Delta P = 0$ in our case:

$$\frac{\Delta\varrho}{\varrho} = \alpha\frac{\Delta P}{P} - \delta\frac{\Delta T}{T} + \varphi\frac{\Delta\mu}{\mu} = -\delta\frac{\Delta T}{T} + \varphi\frac{\Delta\mu}{\mu} \tag{2.10}$$

having defined the three partial derivatives α, δ, φ:

$$\alpha := \left(\frac{\partial\ln(\varrho)}{\partial\ln(P)}\right)_{{\rm T},\,\mu};\quad \delta := -\left(\frac{\partial\ln(\varrho)}{\partial\ln(T)}\right)_{{\rm P},\,\mu};\quad \varphi := \left(\frac{\partial\ln(\varrho)}{\partial\ln(\mu)}\right)_{{\rm P},\,{\rm T}} \tag{2.11}$$

We have now all the equations necessary to solve the motion of our fluid element. From (2.3), (2.6), (2.8) and (2.10) we have a system of second order differential equations:

$$\begin{cases} \varrho\dfrac{{\rm d}^2\Delta r}{{\rm d}t^2} + g\Delta\varrho = 0 \\ \dfrac{{\rm d}\Delta\mu}{{\rm d}t} - \dfrac{\mu}{H_{\rm P}}\nabla_\mu\dfrac{{\rm d}\Delta r}{{\rm d}t} = 0 \\ \dfrac{{\rm d}\Delta T}{{\rm d}t} + \dfrac{T}{H_{\rm P}}\left(\nabla_{\rm ad} - \nabla\right)\dfrac{{\rm d}\Delta r}{{\rm d}t} = 0 \\ \dfrac{\Delta\varrho}{\varrho} + \delta\dfrac{\Delta T}{T} - \varphi\dfrac{\Delta\mu}{\mu} = 0 \end{cases} \tag{2.12}$$

We want now to solve the equations of motion assuming that the fluid element is stable against convection. This means that the displaced element will be oscillating around the position of equilibrium. We can solve this assuming an oscillating solution of the type $\Delta x = A_{\rm x}\ e^{iNt}$ for each $x \in (T, \varrho, \mu, r)$, where $A_{\rm x}$ is the amplitude of the oscillation and N its frequency.
The coefficient matrix associated with the system (2.12) is therefore:

$$\begin{bmatrix} 0 & g & 0 & -\varrho\, N^2 \\ 0 & 0 & i\,N & -i\dfrac{\mu}{H_{\rm P}}\nabla_\mu\, N \\ i\,N & 0 & 0 & i\dfrac{T}{H_{\rm P}}\left(\nabla_{\rm ad}-\nabla\right) N \\ \dfrac{\delta}{T} & \dfrac{1}{\varrho} & -\dfrac{\varphi}{\mu} & 0 \end{bmatrix} \tag{2.13}$$

whose determinant we set equal to zero in order to solve the system:

$$-g\left[-N^2\left(\nabla_{\rm ad}-\nabla\right)\frac{\delta}{H_{\rm P}} - N^2\ \nabla_\mu\ \frac{\varphi}{H_{\rm P}}\right] - N^4 = 0 \tag{2.14}$$

and rearranging we obtain:

$$N^2\ = \frac{g\cdot\delta}{H_{\rm P}}\left(\nabla_{\rm ad}-\nabla+\frac{\varphi}{\delta}\nabla_\mu\right) \tag{2.15}$$

This equation represents the condition for stability of a displaced fluid element; N is commonly known as the "Brunt-Väisälä frequency". If $N^2 > 0$, then N is real and the element keeps oscillating around its original position, according to the solution $\Delta r = A_{\rm r}\ e^{i|N|t}$. But if $N^2 < 0$, N would be imaginary, therefore $\Delta r = A_{\rm r}\ e^{|N|t}$ and the element will move exponentially away from its original position, giving rise to a convective instability (for more details about the derivation, see Salaris & Cassisi, 2005).
Thanks to this simple treatment, we can formally express the condition for stability against convection, assuming that the surroundings are dominated by radiative transport:

$$\nabla_{\rm ad} + \frac{\varphi}{\delta}\nabla_\mu > \nabla_{\rm rad} \tag{2.16}$$

which is known as the "Ledoux criterion" (Ledoux, 1947). In case of a chemically homogeneous stratification ($\nabla_\mu = 0$), the criterion simplifies to the

"Schwarzschild criterion" (Schwarzschild, 1958):

$$\nabla_{\rm ad} > \nabla_{\rm rad} \tag{2.17}$$

for a dynamically stable stratification.

This simple treatment represents a simplification that does not take into account all the physical phenomena involved in generating convection. Whether a stratification is convectively unstable or not depends on the relative importance of the buoyancy driving and the stabilizing effect of viscous and thermal diffusion. One way of taking these effects into account is to compute the so-called "Rayleigh number" (or Ra) for the stratification. Ra is defined as the ratio between the diffusive and convective thermal transport time-scales in a fluid, and its value represents the flow regime: above a critical Ra, the fluid is unstable to convection. The threshold is commonly placed around 10^3 (Chandrasekhar, 1961). In stellar interiors, the Rayleigh number ranges around 10^{15} - 10^{25} (see Jermyn et al., 2022).

Overall, the formalism described in this section, developed in the mid-twentieth century, represented at the time a real turning point for modelling the stellar evolution: once the profile of the stratification is known, i.e. the variables P, T, ϱ, μ as function of the radius, the criteria above automatically say whether the layers become convective or not. This is a very powerful way of modelling convection within a simplified framework such as 1D stellar modelling. In the following section, we shall see how this is implemented.

2.1.1 1D implementation: the mixing length theory

I described in the previous section how it is possible to determine if a stratification is convectively unstable thanks to the Ledoux and Schwarzschild criteria (i.e. $\nabla_{\rm ad} < \nabla_{\rm rad}$). The critical assumption behind them is that the element is purely adiabatic, and the surroundings purely radiative, but of course this is not the case in real stars. The fluid elements actually undergo some cooling,

thus changing both their temperature and the stratification. In this perspective, the situation in a convective environment is more accurately:

$$\nabla_{\rm ad} < \nabla_{\rm e} < \nabla_{\rm s} < \nabla_{\rm rad}$$

where the temperature gradients of the element and the surroundings are intermediate between the adiabatic and the radiative ones (see Kippenhahn et al., 2012). Therefore, the question of how to compute the correct temperature gradients arises. This problem is normally approached employing the so-called "mixing-length theory" (Böhm-Vitense, 1958), that provides a simple formalism for the local treatment of convection, with the possibility of computing the temperature gradients along the stellar radius at any time.

$\nabla_{\rm ad}$ and $\nabla_{\rm rad}$ can be both expressed analytically (see Kippenhahn et al., 2012). Starting from the usual thermodynamic relations, one can show that for constant entropy and assuming fixed chemical composition, the temperature gradient is

$$\nabla_{\rm ad} = \frac{P\,\delta}{T\,\varrho\,c_{\rm P}} \tag{2.18}$$

where $c_{\rm P}$ is the specific heat capacity at constant pressure. On the other hand, if radiative transport is treated as a diffusive process, and assuming hydrostatic equilibrium, the temperature gradient can be expressed as:

$$\nabla_{\rm rad} = \frac{3}{16\pi a\,c\,G}\frac{\kappa\,L\,P}{M\,T^4} \tag{2.19}$$

where κ is the mean absorption coefficient (also known as opacity), L the luminosity at that radius, a the radiation density constant, c the speed of light, G the gravitational constant, and M the mass contained within the radius.

The mixing-length theory is based on the assumption that fluid elements are transported by convective motions over a certain distance $\ell_{\rm m}$ (the mixing length), before they mix again with the surroundings and dissolve. Thanks to this assumption, it is possible to derive a set of equations that can be used to compute the correct temperature gradient for the surroundings ∇, for the

element $\nabla_{\rm e}$, the average velocity of the element v and other quantities, assuming that $P, T, \varrho, \nabla_{\rm ad}, \nabla_{\rm rad}, c_{\rm P}, g$ are known.

I refer to Kippenhahn et al. (2012) for a rigorous derivation of the equations and their solution. It is worth presenting here the results. The following is a cubic equation in ξ with one real solution, that allows to compute ∇ given the following definitions for ξ, U, W:

$$\begin{gathered}(\xi - U)^3 + \frac{8}{9} U \left(\xi^2 - U^2 - W\right) = 0 \\ \xi^2 := \nabla - \nabla_{\rm ad} + U^2; \quad U := \frac{3acT^3}{c_{\rm P}\varrho^2 \kappa \ell_{\rm m}^2} \sqrt{\frac{8H_{\rm P}}{g\delta}}; \quad W := \nabla_{\rm rad} - \nabla_{\rm ad}\end{gathered} \tag{2.20}$$

Once ∇ is found, it can be used to derive also $\nabla_{\rm e}$ from the equation:

$$(\nabla - \nabla_{\rm e})^{3/2} = \frac{8}{9} U \left(\nabla_{\rm rad} - \nabla\right) \tag{2.21}$$

and with ∇ and $\nabla_{\rm e}$ known, the velocity of the element can be derived:

$$v^2 = g\delta \left(\nabla - \nabla_{\rm e}\right) \frac{\ell_{\rm m}^2}{8H_{\rm P}} \tag{2.22}$$

The mixing-length theory is an exceptional method in its simplicity, perfect for stellar-structure computations. However, its biggest limitation is the uncertainty on the parameter $\ell_{\rm m}$, which is not an output of the theory but it needs to be fixed by hand. It is usually expressed as a fraction of the local pressure scale height $\ell_{\rm m} = \alpha_{\rm m} H_{\rm P}$ with $\alpha_{\rm m}$ assumed constant and calibrated to observations through stellar models. Indicatively, values for $\alpha_{\rm m}$ span between 1.5 - 2.0 (Arnett et al., 2018; Ekström et al., 2012; Ludwig et al., 1999; Schaller et al., 1992). Additionally, the mixing-length theory still requires to know the extent of the convective zone, which is obtained from the Schwarzschild or Ledoux criterion, and when convection begins and ends.

2.2 Convective boundary mixing

The treatment of convection described in Sec. 2.1 allows us to determine the extent of convective regions in stars. In particular, the Schwarzschild and

Ledoux criteria are used to define the location of the convective boundaries. However, this simplified approach does not take into account the additional mixing effects that occur close to the convective boundaries. These effects, that can have different features depending on the regime (see Zahn, 1991; Viallet et al., 2015), are usually grouped under the name of "convective boundary mixing" (CBM). CBM cannot be neglected in stellar modelling because it affects the size of the convective regions, and this can have a critical effect on the evolution of the star, such as the predictions on its lifetime (Kaiser et al., 2020). Thus, it is important to include CBM in 1D stellar models as well as to study its features with multi-D numerical simulations.

2.2.1 1D modelling and overshooting

Historically, convective boundary mixing has been introduced in 1D stellar models to make up for an important deficiency in the theory of convection (e.g. Shaviv & Salpeter, 1973; Maeder, 1975). Stellar evolutionary models employ the Schwarzschild or Ledoux criterion to define the convective boundary location, i.e. where $\nabla_{\rm rad} = \nabla_{\rm ad}$ or $\nabla_{\rm rad} = \nabla_{\rm ad} + \frac{\varphi}{\delta}\nabla_{\mu}$ respectively. However, the boundaries defined in such a way are used to separate regions of the star where the convective velocity, v, is $v > 0$ from where it is $v = 0$, without accounting for the fact that the fluid elements need to be decelerated before their velocity is null (see e.g. Renzini, 1987). In other words, the element is accelerated in the convective region by the buoyancy force until it reaches the boundary, then the acceleration suddenly changes sign but the element can keep travelling into the external stable layers under its own inertia, carrying momentum and chemical species as it moves. Clearly, the theory of convection needs to be improved in order to account for such effect.

First of all, a word on the terminology. Often in the literature, the terms "overshooting", "penetration", and "convective boundary mixing" are used as synonyms, potentially generating confusion. Zahn (1991) pointed out that

"overshooting" should be used for an inefficient penetration, that can still transport chemicals and momentum but does not alter the temperature gradient of the stable region, while "penetrative convection" should be used for when convection is strong and can induce changes in the subadiabatic stratification of the stable region, i.e. transporting efficiently also entropy. In this work, I use "convective boundary mixing" as an umbrella term to refer to all prescriptions that provide an extension of the region affected by mixing of chemicals and momentum beyond the convective boundary. The question of whether the temperature gradient of the stable region should be modified in each prescription or not, although crucial, is complex and still object of debate today.

Some of the earliest studies on the issue by Roxburgh (1978, 1989) showed that it is possible to constrain the maximum size of a convective region by simple analytical considerations. Assuming a time-independent (stationary) convection, and integrating the equations of motions for a fluid over the volume of the convective region, the following integral constraint can be derived:

$$\int_V \left(\overline{F}_\mathrm{r} - \overline{\Gamma}_\mathrm{r}\right) \frac{1}{T_0^2} \frac{\mathrm{d}T_0}{\mathrm{d}r} \, \mathrm{d}V = \int_V \frac{\Phi_0}{T_0} \, \mathrm{d}V \geq 0 \tag{2.23}$$

where F_r is the radial radiative flux, Γ_r is the radial energy flux from nuclear sources, T is the temperature, and Φ is the viscous dissipation rate. The subscript 0 represents the mean part of a variable, while the overline represents the average done over turbulent fluctuations: by construction, $\overline{q} = q_0$ for a variable q. The integral constraint comes from the fact that the right hand side of (2.23) is necessarily positive. Taking zero as a lower bound, the integral must have both positive and negative contributions. Since generally $\mathrm{d}T_0/\mathrm{d}r < 0$, this requires that the convective zone includes both regions where $\overline{F}_\mathrm{r} < \overline{\Gamma}_\mathrm{r}$, which is the usual nearly-adiabatic stratification predicted by the mixing length theory, but also where $\overline{F}_\mathrm{r} > \overline{\Gamma}_\mathrm{r}$: this means that convection extends further into the stable region. In this way, Roxburgh (1978) obtains the maximum size for a convective region. For a more modern discussion, see

e.g. Anders & Pedersen (2023).

In the following years, researchers started developing various prescriptions for implementing CBM in 1D stellar models. First proposed, and still largely used today, is the "step overshoot" prescription (Zahn, 1991): beyond the convective boundary, the convective region is extended by a fraction of the pressure scale height $d_{\rm ov} = \alpha_{\rm ov} H_{\rm P}$. The temperature gradient of the "overshooting" region is assumed to be adiabatic, like in the convective region: in this way, both the convective and the overshooting regions are part of the same turbulent environment, and a new convective boundary is defined. However, this simple approach has the same problem as the mixing-length theory: the free parameter $\alpha_{\rm ov}$ needs to be calibrated. Early works (Schaller et al., 1992; Stothers & Chin, 1992) suggested values for $\alpha_{\rm ov}$ in the range 0.1 - 0.2; however, more recent studies have proposed a dependence of $\alpha_{\rm ov}$ on the stellar mass (Claret & Torres, 2016; Scott et al., 2021), and recent asteroseismic measurements of $\alpha_{\rm ov}$ indicate that these values might be underestimated in stellar models (see Bowman, 2020).

A different prescription that has been suggested for CBM comes from the study of Freytag et al. (1996). Based on 2D hydrodynamic simulations of different stellar environments, they noticed that convective velocities extend well beyond the convective boundary and decay exponentially with the radius; thus, a finite overshoot distance is inaccurate for modelling CBM. This led to the suggestion of treating CBM as a diffusive process, introducing the exponentially-decaying diffusion coefficient:

$$D_{\rm ov}(z) = t_{\rm c} v_{\rm rms}^2(z) = t_{\rm c} v_0^2 \exp\left(\frac{-2z}{f_{\rm ov} H_{\rm P,0}}\right) \tag{2.24}$$

where z is the distance from the convective boundary, determined using e.g. the Schwarzschild criterion, $t_{\rm c}$ the convective time-scale, $v_{\rm rms}$ the root-mean-square velocity as function of z, v_0 the velocity inside the convective zone, and $H_{\rm P,0}$ the pressure scale height at the boundary location. Usually, for stellar modelling the factor $t_{\rm c} v_0^2$ is replaced by D_0, which is the diffusion coefficient in-

side the convective zone near the boundary location, given by the MLT. Once again, $f_{\rm ov}$ is a parameter that needs calibration. Stellar modelling studies (Herwig, 2000; Jones et al., 2015) suggest values between 0.01 - 0.02 to match the results of stellar models that use the step-overshoot prescription, although just like for $\alpha_{\rm ov}$ a mass dependence and larger values are likely.

It is worth mentioning also a modified approach derived from the one just described, which is often called "double-f" because it assumes two separate exponential decays with different slopes, the first one representing the shear mixing below the convective boundary, and the second the shallower decay of mixing efficiency outside the boundary. This approach has been introduced by Herwig et al. (2007) and further tested by Battino et al. (2016).

Further approaches for studying convection and CBM processes in stars include "double-diffusive convection", for when the fluid stratification depends on two components with different rates of diffusion (Garaud, 2018); a dependence of the overshooting distance on the luminosity and extent of the convective zone (Baraffe et al., 2023); alternative diffusion coefficients (Baraffe et al., 2017); effects of stellar rotation on overshoot (Browning et al., 2004; Rogers et al., 2013).

Despite the extensive studies, many uncertainties remain on how to correctly implement CBM in 1D evolutionary codes. The problem comes from the disagreement on CBM prescriptions between theoretical studies, 1D models, hydrodynamic simulations, and observations. Further studying is necessary to shed more light on the question, and multi-D modelling of the fluid dynamics can play a major role in this context.

2.2.2 Multi-D simulations and entrainment

Ever since the advancements in computing resources allowed it, multi-D simulations of stellar environments have been investigating the question of convective boundary mixing. The details and limitations of this methodology will be

discussed in the following chapter, but the critical advantage of this approach is that it is not necessary to assume any prescription for CBM as the ones discussed above for 1D stellar models, because the fluid motions are followed explicitly. Instead, it is possible to use results coming from hydrodynamic simulations to improve the prescriptions, calibrate the free parameters, and possibly suggest new implementations.

Some of the first works in this direction include Hurlburt et al. (1994), Singh et al. (1995) and Brummell et al. (2002), who ran multi-D simulations of convection in stellar-type layers in order to study penetration and overshooting in the stable stratification, basing only on local properties of the convective zone. Their work showed that the extent of the CBM region is inversely proportional to the relative stability, or "stiffness", of the convective boundary, defined from the polytropic indices of the fluids.

This research has been further advanced by the aforementioned Freytag et al. (1996), and more recently by Meakin & Arnett (2007), who suggested a new prescription for CBM based on 3D hydrodynamic simulations. This approach was rather different from what had been used before, because it is based on the assumption, supported by the numerical simulations, that the location of the convective boundary is expected to move further into the radiative region as time passes. This happens because stable material is transported into the convective zone through the boundary due to shear mixing. The net effect is that more fluid becomes convective, and the convective region grows with time.

In order to parametrize this effect, Meakin & Arnett (2007) employed the so-called "entrainment law", originally developed for geophysical studies (Fernando, 1991). The law relates the entrainment rate E to the physical properties of the boundary:

$$E = \frac{v_{\mathrm{e}}}{v_{\mathrm{c}}} = A\ Ri_{\mathrm{B}}^{-n} \tag{2.25}$$

where $v_{\rm e}$ is the entrainment velocity, i.e. the speed at which the boundary moves under entrainment, $v_{\rm c}$ the convective velocity, $Ri_{\rm B}$ the bulk Richardson number, and A, n are free parameters. The dimensionless bulk Richardson number, defined as the ratio between buoyancy stabilization and shear kinetic energy, can be expressed as

$$Ri_B = \frac{\ell\ \Delta b}{v_{\rm c}^2}\ ; \quad \Delta b = \int_{r_1}^{r_2} N^2 dr \tag{2.26}$$

with ℓ the length scale of turbulent motions, Δb the buoyancy jump, N the Brunt-Väisälä frequency, r_1 and r_2 two radii that encompass the boundary location. A common choice is $r_1 = r_{\rm b} - \ell/2$ and $r_2 = r_{\rm b} + \ell/2$ with $r_{\rm b}$ being the boundary location, so that the integration length of N^2 around $r_{\rm b}$ is exactly ℓ. There is no strict definition for ℓ, so it is usually taken to be large enough to include completely the peak in N^2 during the integration, as we shall later see. $Ri_{\rm B}$, that depends on both local $(\ell, r_{\rm b}, N)$ and non-local $(v_{\rm c})$ properties, can be also seen as a measure of the "stiffness" of the boundary, since it assumes larger values for boundaries that are more difficult to penetrate. For these reasons, the dependence of CBM on the bulk Richardson number is more important than the one on other numbers introduced to categorize convection (e.g. the Reynolds number, the Rayleigh number), which are based on large-scale properties of the convective region and often fail to represent the physics at the interface between different layers.

The entrainment law can be used in 1D stellar models to predict the location of the convective boundary and how it moves with time. So far in the literature, only two works have included the entrainment law in stellar modelling (Staritsin, 2013; Scott et al., 2021). Of course, similarly to the other prescriptions, the important question is what values to use for the free parameters. It is possible to calibrate A and n through 1D evolutionary simulations, fine-tuning the parameters by comparing results to observations, as well as from multi-D hydrodynamic simulations, measuring the properties of the fluid and estimating the parameters in the law.

In the first case, both Staritsin (2013) and Scott et al. (2021) fix $n = 1$ according to what was found by Fernando (1991), and estimate A using asterosismic measurements and the observed main sequence width. Staritsin (2013) finds $A = 4.05$ - 4.43×10^{-4} for models of 24 and 16 $M_\odot$ respectively, while Scott et al. (2021) find $A = 2 \times 10^{-4}$ for a range of models 8 - 32 $M_\odot$. On the other hand, the entrainment law parameters have been estimated also from hydrodynamic simulations, such as Meakin & Arnett (2007), Cristini et al. (2019). I report here in Fig. 2.1 the summary plot of the entrainment law estimations from Cristini et al. (2019). The value of n starts deviating from 1, but most importantly A is estimated between 0.03 - 0.05, which is two orders of magnitude larger than what is expected from 1D stellar modelling calibrations. So far in the literature, hydrodynamic simulations have always found estimates for A much larger than the values assumed in 1D models. The reason for this disagreement is still obscure. The prevailing idea is that CBM in 1D stellar models is currently underestimated, so when the same configuration is studied with hydrodynamic simulations the layers react by rapidly entraining material as a form of compensation. However, theoretical and numerical difficulties in computing 1D and multi-D simulations make this point extremely difficult not only to prove, but even to explore in more detail. The best approach to the question is to improve both 1D and multi-D models by adjusting one according to the predictions of the other, until after a certain number of iterations a convergence of results is reached. This is exactly what has been done for the simulations presented in Chapter 5.

Finally, it must be noted that there is still no universal agreement about the role of entrainment as a CBM mechanism in the different phases of stellar evolution. This comes from the opposite views of CBM as either a quasi-steady state of the stratification, typical of the traditional prescriptions, or a dynamical process, described by the entrainment law that predicts a migration of the boundary over time. The disagreement originates from the fact that multi-D hydrodynamic simulations measure very large entrainment rates in stars, often

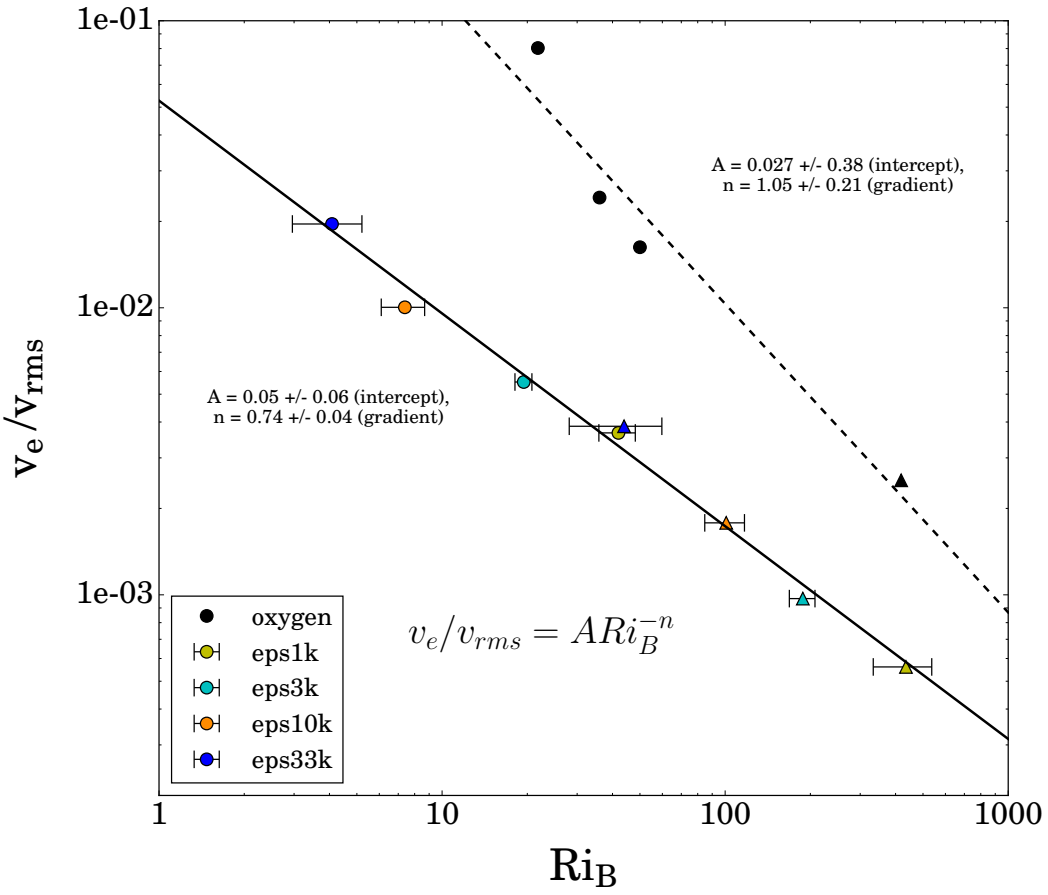

Figure 2.1: Entrainment rate versus bulk Richardson number in log scale, measurements from hydrodynamic simulations and respective linear regressions: Meakin & Arnett (2007) (black points, dashed line), Cristini et al. (2019) (coloured points, solid line). Figure taken from Cristini et al. (2019).

predicting the engulfment of a large part of the star in a short time. This issue calls for a mechanism that stops the entrainment of additional material after a certain time, whether by reaching a new thermal equilibrium that is statistically constant in time (see Andrassy et al., 2023), or by a rapid extinction of fuel and death of convection more typical of the late burning phases (see Rizzuti et al., 2023). In the following section, I will present how it is possible to distinguish between CBM prescriptions based on the different environments.

2.2.3 Choosing the appropriate CBM prescription

We have seen that prescriptions for reproducing CBM in 1D stellar models are many and diverse. One may then wonder in which context it is more correct to apply one rather than another. The question is complex and still an object of discussion, but fortunately some studies have approached the problem. I already mentioned a first distinction done by Zahn (1991), at least in the terminology. A more rigorous work has been done by Viallet et al. (2015), who distinguish three different regimes of CBM based on the Péclet number Pe, defined as the ratio of radiative over advective time-scale for heat transport.
The three regimes are the following. When $\mathrm{Pe} < 1$, the environment is dominated by radiative diffusion, which has a shorter time-scale therefore is more efficient, so we are in a "diffusion-dominated regime", where only chemicals can be mixed. It is reasonable to treat this mixing with the diffusive approach of Freytag et al. (1996). This is applicable to stellar surface convection, where radiative effects are important.
On the opposite, when $\mathrm{Pe} > 1$ radiative effects are negligible, so the mixing can be considered adiabatic. This results in strong CBM that mixes both composition and entropy, and cannot be slowed down or stopped by radiative cooling: this is the "entrainment regime", and it is appropriate to employ here the entrainment law. This regime takes place in late burning phases of massive stars, where neutrino loss is the dominant cooling mechanism and radiative diffusion

(i.e. photon cooling) can be ignored.

Finally, the third regime is intermediate between the previous two, a transition Pe $\sim$ 1 where radiative diffusion is still important but not always dominant. Consequently, the structure of the boundary is also split in two parts: an inner adiabatic one that can be described by step overshoot, plus an outer one more dominated by radiation where diffusive mixing can be used. This picture, that Viallet et al. (2015) call "penetrative regime", describes the situation of burning phases in deep stellar interiors where photons dominate the cooling, such as the main-sequence core burning. The Viallet et al. (2015) suggestions for CBM prescriptions may not describe all regimes accurately, but they are useful for providing an idea of what the relevant parametrization may be for different situations.

Finally, it is worth mentioning here that when convective burning takes place in shells above the core, during late-phase stellar evolution, two convective boundaries are present, an upper and a lower one. Therefore, it is important to remember that CBM is expected to occur at both boundaries, thus requiring to apply CBM prescriptions to both. Recent hydrodynamic simulations are starting to shed more light on this situation, which is sometimes referred to as "undershooting", confirming that CBM occurs and is important at both convective boundaries, and that the lower one usually moves $\sim$ 5 - 10 times slower than the upper one, due to its larger stiffness (see Cristini et al., 2019; Rizzuti et al., 2022).

3 Methodologies

Recent advances in computing resources have enabled the production of increasingly detailed and accurate stellar simulations. This results, on the one hand, in large grids of 1D models that explore a range of stars with different properties (mass, metallicity, rotation, binarity), and on the other hand in highly-detailed simulations of the fluid dynamics in stellar interiors.
In this chapter, I will present the software tools that I employed in my work for modelling convection and nucleosynthesis in stars. I will describe the computational software used for stellar modelling and fluid dynamics, including a description of the possible options that can be employed in order to simulate the most realistic stellar environments.

3.1 Stellar modelling: 1D versus multi-D

It is possible to approach stellar modelling in two radically different ways: one-dimensional (1D) and multi-dimensional (multi-D). 1D stellar models rely on the assumption of spherical symmetry, so the simulations follow the evolution of variables that are only a function of the radius. This approximation, although it simplifies the complex multi-dimensional physical processes of the star, makes the computation extremely efficient, so most 1D stellar codes are able to follow the evolution of the entire star, centre to surface, for most of its life, from the ZAMS to the final phases just before its death.
Modelling the stellar evolution consists of computing how some key variables, functions of the mass coordinate m, evolve with time: radius r, density ϱ, pressure P, temperature T, luminosity l, and mass fraction X_i for all species $i = 1, \ldots, I$ involved in nuclear reactions. In order to solve this problem, a set of $5 + I$ equations is required, one per variables. The equations are (see

Kippenhahn et al., 2012):

$$\begin{cases} \dfrac{\partial r}{\partial m} = \dfrac{1}{4\pi r^2 \varrho} & \text{mass continuity} \\ \dfrac{\partial P}{\partial m} = -\dfrac{Gm}{4\pi r^4} - \dfrac{\partial^2 r}{\partial t^2}\dfrac{1}{4\pi r^2} & \text{pressure balance} \\ \dfrac{\partial l}{\partial m} = \varepsilon_{\mathrm{n}} - \varepsilon_{\nu} - c_{\mathrm{P}}\dfrac{\partial T}{\partial t} + \dfrac{\delta}{\varrho}\dfrac{\partial P}{\partial t} & \text{energy conservation} \\ \dfrac{\partial T}{\partial m} = -\dfrac{GmT}{4\pi r^4 P}\nabla & \text{energy transport} \\ \varrho = \varrho\left(P, T, X_i\right) & \text{equation of state} \\ \dfrac{\mathrm{d}X_i}{\mathrm{d}t} = \dfrac{\partial X_i}{\partial t} + \dfrac{\partial}{\partial m}\left(D' \dfrac{\partial X_i}{\partial m}\right) & \text{nuclear species, } i \in [1, I] \end{cases} \tag{3.1}$$

where ε_{n} is the nuclear energy release rate, ε_{ν} the neutrino loss rate, ∇ the temperature gradient defined as $\nabla := \mathrm{d}\ln(T)/\mathrm{d}\ln(P)$, and D' the diffusion coefficient. For completeness, it is worth mentioning that also $\varepsilon_{\mathrm{n}}, \varepsilon_{\nu}$ and other quantities in (3.1) are function of P, T, X_i, but their values are known and tabulated.

The nuclear species equation in (3.1) describes the time evolution of the abundances, which depends both on the nuclear reactions (first term on the right-hand side) and on the various transport processes (second term). More extensively, the equation can be written as:

$$\frac{\mathrm{d}X_i}{\mathrm{d}t} = \frac{m_i}{\varrho}\left(\sum_j R_{j,i} - \sum_k R_{i,k}\right) + \frac{\partial}{\partial m}\left[\left(4\pi r^2 \varrho\right)^2 D_{\mathrm{tot}} \frac{\partial X_i}{\partial m}\right] \tag{3.2}$$

with m_i the species mass, $R_{a,b}$ the rate of the reaction that transforms species $a \to b$, and D_{tot} the total diffusion coefficient. The first term on the right-hand side of (3.2) represents the production and destruction of species from nuclear reactions. The second term expresses the transport of species in spherical coordinates (see Eggenberger et al., 2008), and the diffusion coefficient D_{tot} can include contributions from e.g. convection, shear mixing, meridional circulation.

The set of equations in (3.1) can be further simplified. If we assume that the stellar evolution is slow $\partial^2 r/\partial t^2 \sim 0$, as normally happens in stars, the pressure balance equation in (3.1) reduces to the hydrostatic equilibrium equation

$$\frac{\partial P}{\partial m} = -\frac{Gm}{4\pi r^4} \tag{3.3}$$

Likewise, in some cases the energy variations are also slow, as during stellar burning phases, so the time derivatives can be neglected and the energy conservation equation becomes

$$\frac{\partial l}{\partial m} = \varepsilon_{\mathrm{n}} - \varepsilon_{\nu} \tag{3.4}$$

In this case, we talk of a system in complete equilibrium, both mechanical and thermal. It is important to note that under these assumptions the only time-dependent equations in (3.1) are the nuclear burning ones.

The set of equations is now solved in the following way. First, the boundary conditions for the system are imposed; in a simplified case for example, we have in the centre and at the surface of a star with total mass M, radius R and luminosity L:

$$\begin{cases} m = 0 & \rightarrow \quad r = 0; \qquad l = 0 \\ m = M & \rightarrow \quad r = R; \qquad l = L; \quad \varrho = P = T = 0; \end{cases} \tag{3.5}$$

As I said, in case of complete equilibrium the only equations in (3.1) with a time dependence are the nuclear burning ones; therefore, during the computation they are solved separately, with an "equations-split" approach (see Kippenhahn et al., 2012). At each time-step, the chemical composition X_i is updated thanks to the nuclear burning equations, and then the remaining structure equations are solved to find r, ϱ, P, T, l, which determine the stellar structure.

Stellar evolution modelling has drastically changed with the advent of computing facilities. Since Henyey et al. (1959) up until today, electronic computers have allowed to solve the stellar structure system (3.1) rapidly and efficiently.

The variables are discretized on a one-dimensional, non-uniform grid that allows to introduce higher resolution where the variables change abruptly; the grid itself may vary over time to increase or decrease the resolution as needed. These techniques made it possible to create many numerical codes for following the stellar evolution, much more complex than what I have described in this section, including the most updated stellar physics and allowing to investigate the evolution of stars with a range of different masses and properties (e.g. Heger & Woosley, 2002; Paxton et al., 2011; Ekström et al., 2012).

At the other end of the spectrum, we have stellar modelling with multi-D simulations (2D or 3D). This approach is radically different from the 1D stellar modelling just described. Relaxing the assumption of spherical symmetry, it is possible to simulate multi-dimensional processes in stellar interiors (e.g. convection, rotation, magnetic fields) without any need for prescription as in the 1D case, but explicitly witnessing these phenomena occurring naturally in the simulations. However, the higher dimensionality makes the code much more expensive to run, requiring a detailed grid to resolve the fluid scale, but most importantly very small time-steps in order to follow the fluid motions. For these reasons, multi-D models can only reproduce small sections of a star for a small fraction of its burning time-scales. But in return, they can achieve an incredible degree of detail and realism that is useful for testing our understanding of the physical processes that characterize stellar interiors, and possibly extract theoretical knowledge and prescriptions to improve the 1D models.

Both 1D and multi-D stellar models present advantages and limitations. The most effective way for making progress in stellar evolution studies is to develop synergies between the two. Indeed, one approach is intrinsically linked to the other: multi-D simulations need to assume initial conditions from 1D models, which are more general, while 1D models can be improved from the results of multi-D simulations, which are far more detailed.

3.2 Fluid dynamics and Navier-Stokes equations

Multi-dimensional stellar codes are designed to model the time evolution of the dynamics of a stellar fluid, usually in a convective environment. This is done by solving the equations of motion for the fluid elements using numerical methods. We shall see now what the relevant equations are, and how they are derived (see Landau & Lifshitz, 1987 for more details).
First, the equation of motion for a fluid element is given by the force balancing, in this case the pressure gradient and the gravitational force:

$$\varrho \frac{\mathrm{d}\boldsymbol{v}}{\mathrm{d}t} = -\boldsymbol{\nabla} P + \varrho\, \boldsymbol{g} \tag{3.6}$$

and since the differential expression for $\mathrm{d}\boldsymbol{v}$ is:

$$\mathrm{d}\boldsymbol{v} = \frac{\partial \boldsymbol{v}}{\partial t}\mathrm{d}t + \frac{\partial \boldsymbol{v}}{\partial x}\mathrm{d}x + \frac{\partial \boldsymbol{v}}{\partial y}\mathrm{d}y + \frac{\partial \boldsymbol{v}}{\partial z}\mathrm{d}z = \frac{\partial \boldsymbol{v}}{\partial t}\mathrm{d}t + (\mathrm{d}\boldsymbol{r} \cdot \boldsymbol{\nabla})\, \boldsymbol{v} \tag{3.7}$$

therefore (3.6) becomes:

$$\varrho \left(\frac{\partial \boldsymbol{v}}{\partial t} + (\boldsymbol{v} \cdot \boldsymbol{\nabla})\, \boldsymbol{v} \right) = -\boldsymbol{\nabla} P + \varrho\, \boldsymbol{g} \tag{3.8}$$

This is known as the "Euler's equation", which describes the motion of a fluid assuming no heat exchange between its parts (adiabatic motion). However, this equation does not take into account the energy dissipation that comes from the internal viscosity of the fluid. To include this contribution, I first express (3.8) employing the Einstein notation[1]:

$$\varrho \left(\frac{\partial v_i}{\partial t} + v_j \frac{\partial v_i}{\partial x_j} \right) = -\frac{\partial P}{\partial x_i} + \varrho\, g_i \tag{3.9}$$

[1] The Einstein notation implies a summation over dummy indices (i.e. indices that appear only on one side of an equation) but not over free indices (i.e. indices that appear on both sides of an equation); here the indices i, j, k range over the set $\{x, y, z\}$.

One can rearrange this equation to be expressed in the form (see Landau & Lifshitz, 1987):

$$\frac{\partial \varrho v_i}{\partial t} = -\frac{\partial \Pi_{ij}}{\partial x_j} + \varrho\, g_i \quad ; \quad \Pi_{ij} := P\delta_{ij} + \varrho\, v_i v_j \tag{3.10}$$

where Π_{ij} is the "momentum flux density tensor", that represents the reversible transfer of momentum between different points in space due to mechanical transport and pressure force. If we consider that viscosity contributes to the fluid motion with an irreversible transfer of momentum from points with larger velocity to ones with smaller velocity, then we can correct the momentum flux density tensor to account for viscosity by adding a term σ'_{ij} that represents the irreversible viscous transfer of momentum (see Landau & Lifshitz, 1987):

$$\Pi_{ij} \to \Pi_{ij} - \sigma'_{ij} = P\delta_{ij} + \varrho\, v_i v_j - \sigma'_{ij} \tag{3.11}$$

This correction can be implemented in equations (3.10) and therefore in (3.9), producing:

$$\varrho \left(\frac{\partial v_i}{\partial t} + v_j \frac{\partial v_i}{\partial x_j} \right) = -\frac{\partial P}{\partial x_i} + \frac{\partial \sigma'_{ij}}{\partial x_j} + \varrho\, g_i \tag{3.12}$$

The term σ'_{ij} is called the "viscous stress tensor", and it can be expressed in a general way imposing that σ'_{ij} satisfies certain conditions:

- friction occurs if and only if the fluid has different velocities in different points of space: σ'_{ij} depends on and only on space derivatives of the velocity;

- friction does not occur for rigid body rotation: σ'_{ij} has only terms of the kind $\partial v_k/\partial x_k$ and $\partial v_i/\partial x_j + \partial v_j/\partial x_i$, because they vanish for fixed angular velocity $\boldsymbol{\omega}$ (since $\boldsymbol{v} = \boldsymbol{\omega} \times \boldsymbol{r}$).

Under these assumptions, the viscous stress tensor assumes the form:

$$\sigma'_{ij} = \eta \left(\frac{\partial v_i}{\partial x_j} + \frac{\partial v_j}{\partial x_i} - \frac{2}{3}\delta_{ij} \frac{\partial v_k}{\partial x_k} \right) + \zeta \delta_{ij} \frac{\partial v_k}{\partial x_k} \tag{3.13}$$

written in this way so that the terms between the brackets are equal to zero over tensor contraction of σ'_{ij}, i.e. when computing the trace σ'_{ii}. The quantities η and ζ, known as the first and second "coefficients of viscosity", are scalars if we assume that the fluid is isotropic, and it is possible to show they are always positive due to energy dissipation and entropy increase (see Landau & Lifshitz, 1987). We can then replace this definition into (3.12) to obtain the general equation of motion for a viscous fluid:

$$\begin{aligned}\varrho\left(\frac{\partial v_i}{\partial t}+v_j\frac{\partial v_i}{\partial x_j}\right)=&-\frac{\partial P}{\partial x_i}+\frac{\partial}{\partial x_j}\left[\eta\left(\frac{\partial v_i}{\partial x_j}+\frac{\partial v_j}{\partial x_i}-\frac{2}{3}\delta_{ij}\frac{\partial v_k}{\partial x_k}\right)\right]+\\&+\frac{\partial}{\partial x_i}\left(\zeta\frac{\partial v_k}{\partial x_k}\right)+\varrho\, g_i\end{aligned} \tag{3.14}$$

This equation can be simplified assuming that η, ζ do not vary significantly throughout the fluid, so they can be extracted from the space derivatives:

$$\varrho\left(\frac{\partial v_i}{\partial t}+v_j\frac{\partial v_i}{\partial x_j}\right)=-\frac{\partial P}{\partial x_i}+\eta\frac{\partial^2 v_i}{\partial x_j^2}+\left(\frac{1}{3}\eta+\zeta\right)\frac{\partial^2 v_j}{\partial x_i\partial x_j}+\varrho\, g_i \tag{3.15}$$

This can also be written employing the usual vector notation:

$$\varrho\left(\frac{\partial \boldsymbol{v}}{\partial t}+(\boldsymbol{v}\cdot\boldsymbol{\nabla})\,\boldsymbol{v}\right)=-\boldsymbol{\nabla}P+\eta\nabla^2\boldsymbol{v}+\left(\frac{1}{3}\eta+\zeta\right)\boldsymbol{\nabla}\,(\boldsymbol{\nabla}\cdot\boldsymbol{v})+\varrho\,\boldsymbol{g} \tag{3.16}$$

The three equations described by (3.16) are called the "Navier-Stokes equations", and they represent the equations of motion for a compressible viscous fluid. The equations simplify if the fluid can be approximated to be incompressible, since applying the condition for flow incompressibility $\nabla\cdot\boldsymbol{v}=0$ we obtain:

$$\varrho\left(\frac{\partial \boldsymbol{v}}{\partial t}+(\boldsymbol{v}\cdot\boldsymbol{\nabla})\,\boldsymbol{v}\right)=-\boldsymbol{\nabla}P+\eta\nabla^2\boldsymbol{v}+\varrho\,\boldsymbol{g} \tag{3.17}$$

which makes the problem simpler to solve and applies to most cases in geophysics, since usually a viscous fluid is also incompressible. This is not necessarily true in stellar physics, where the fluid can be both viscous and compressible, therefore stellar hydrodynamic codes are normally either fully compressible, i.e. they solve the Navier-Stokes equations in the form of (3.16), or they rely on intermediate approximations such as the anelastic approximation,

which derives new equations assuming small variations in the thermodynamic quantities compared to the mean state (see e.g. Clune et al., 1999).
The Navier-Stokes equations do not have any known analytical solution (the existence of a solution is one of today's most important unsolved problems in Physics), therefore they must be solved numerically on a discretized grid. This is the standard approach for modelling the turbulent flow in stellar multi-D simulations, as I shall describe in the following sections.
Finally, the total energy of the fluid must be conserved at all times, therefore the energy variation in time must be zero. This is described by an energy conservation equation, which in Euler's formalism assumes the form (see Landau & Lifshitz, 1987):

$$\frac{\partial}{\partial t}\left(\varrho E\right) + \boldsymbol{\nabla} \cdot \left[\boldsymbol{v}\left(\varrho E + P\right)\right] = \varrho\, \boldsymbol{v} \cdot \boldsymbol{g} \tag{3.18}$$

where E is the total specific energy, sum of the kinetic and internal energy, and the term on the right-hand side of the equation comes from the gravitational potential. In case there is additional generation or dispersion of energy, extra terms can be included on the right-hand side of the equation, as it happens in stars with nuclear energy generation and radiation or neutrino losses (see in the following sections).

3.3 Computational approach to fluid dynamics

As we just saw, the general approach for solving a problem of fluid dynamics consists of discretizing the fluid variables on a finite grid and computationally solving the Navier-Stokes equations to follow the fluid motions over time. The main difference between the specific implementations lies in the way the problem of having a range of fluid scales is handled. Indeed, turbulent motions in a fluid occur on a variety of spatial scales, from the largest ones ("integral

scales") that contribute to most of the kinetic energy of the fluid, to the smallest ones ("dissipative scales") where viscous effects dissipate the kinetic energy into heat and break down the turbulent flow. These scales can be significantly distant from each other, especially for astrophysical fluids. Thus, the problem of including all these different scales within the same simulation arises.

The simplest approach to computational fluid dynamics would be to build a mesh grid which is fine enough to resolve the dissipative scale, but also with a domain large enough to cover the integral scale. This method, known as the direct numerical simulation (DNS), can be considered the most accurate since it reproduces all the principal fluid scales, but this makes it also extremely expensive in terms of computing power. For typical stellar interiors, the dissipative scale is about ~ 1 cm, while the integral scale can be as big as $\sim 10^9$ cm. This difference of about nine orders of magnitude in spatial scale makes it practically impossible to simulate stellar interiors with DNS.

To overcome this problem, an alternative method has been developed, in which the large integral scales are still included in the domain, but the smallest scales are excluded by having a less refined grid. This framework is called the large eddy simulation (LES), and it finally makes the computations for stellar fluid dynamics affordable. Obviously, the effects of viscosity on the fluid still need to be taken into account. The LES method is based on the finding by Kolmogorov (1941) that the energy dissipation rate is independent of the scale and of the type of dissipative process, in a scenario known as "turbulent cascade", where kinetic energy is transferred down from larger to smaller scales. Therefore, excluding the smallest scales from the simulations by employing a coarser grid does not affect the behaviour of the fluid at larger scales, as long as the dissipation below the grid (the "sub-grid" scale) is still reproduced in some way.

This can be implemented in different ways, depending on the code. One possibility is to include a term in the governing equations that mimics the dissipation at the sub-grid scale; in this case, we talk of an "explicit LES". For

example, a term of artificial viscosity can be added to the equations of motion (see Garnier et al., 2009). Alternatively, it is possible to avoid adding any extra term of dissipation to the equations, but rather rely on the "numerical dissipation" of the computation, i.e. the difference between the expected exact solutions of the Navier-Stokes equations and the actual approximated solutions on the numerical grid, a difference that comes from the solving scheme and the truncation error. This method is called "implicit LES" or "ILES", and its specifics and applicability strictly depend on the numerical algorithm used to solve the equations. For example, spectral methods solve differential equations by using series expansions for the solutions; by construction, they have no numerical dissipation, therefore they must include an explicit term for viscosity. The accuracy of ILES methods is guaranteed by the fact that the numerical errors in the computation are larger than the corrections introduced to mimic sub-grid dissipation (see Ghosal, 1996). However, when using the ILES method one must be very careful and make sure that the principle of energy conservation is always respected. Therefore, the code must be designed in such a way that the internal energy of the fluid is progressively increased to mimic the effects of viscosity at the dissipative scale.

The ILES approach represents a powerful way of reducing the computational cost for modelling fluid dynamics, and it made possible throughout the years to develop and run complex hydrodynamic simulations that follow the fluid motions in stellar environments. In the following sections, we shall see in more detail how these hydrodynamic simulations are prepared and run.

Finally, the fluid dynamics equations are solved on a discretized grid. In addition to the solving schemes, which can be many and diverse, the question of reconstruction processes for interpolating values on the walls and centre of cells also arises. Without getting into too much detail, it is worth mentioning here the existence of finite-volume methods for representing partial differential equations on a discretized grid (see LeVeque, 2002), the Godunov method (Godunov & Bohachevsky, 1959) for solving partial differential equa-

tions with first-order accuracy, and its higher-order equivalent the piecewise parabolic method (PPM, Colella & Woodward, 1984), a reconstruction scheme with third-order accuracy. PPM is at the base of many cutting-edge hydrodynamical codes, including the one used to produce the simulations presented in this thesis.

3.4 Multi-D hydrodynamic simulations

Today, there are a wide range of hydrodynamical codes specifically designed for simulating stellar convection. Some of them, within the context of deep-interior convective burning, are e.g. `FLASH` (Fryxell et al., 2000), `MUSIC` (Viallet et al., 2016), `PPMSTAR` (Woodward et al., 2014), `SLH` (Miczek, 2013) and `PROMPI` (Meakin & Arnett, 2007), which is the one I employed for the present study. These codes can investigate similar scenarios, and their predictions are in excellent agreement between each other, as recently proven in the code-comparison paper of Andrassy et al. (2022). A different approach are codes based of spectral schemes, i.e. solving the equations of motions through a spectral decomposition of the solutions, such as `ASH` (Clune et al., 1999), `Dedalus` (Burns et al., 2020), `MagIC` (Christensen et al., 2001), and `Rayleigh` (Featherstone & Hindman, 2016). Regardless of the solving scheme, within each code there is a range of options that can be selected to ensure the most realistic environment for modelling a specific stellar scenario. These choices can involve the numerical grid and domain, the geometry, boundary conditions, physical processes, etc.

In this section, I will give a general summary of the most important options and procedures that are normally undertaken when setting up a hydrodynamic code for reproducing a particular stellar environment.

3.4.1 Initial conditions

As I mentioned earlier, hydrodynamic simulations of stars cannot reproduce large fractions of the stellar lifetimes, as it is normally done with 1D evolutionary models. For this reason, multi-D stellar models have to start their computation from initial conditions assumed independently. This is generally done by using data coming from a 1D stellar simulation that has followed the evolution of an entire star for most of its life. The hydrodynamic model focuses only on a section of the star where convection occurs, e.g. the main-sequence core, the envelope, or the late-phase burning cores and shells. Then, the multi-D simulation follows the evolution of the section in great detail, but for a limited time-scale, usually long compared to the convective motions but shorter than the evolutionary time-scale.

Nevertheless, the question of translating these conditions from the 1D to the multi-D models is not trivial, and can present some issues. Usually, key quantities like density, pressure, temperature, entropy, mass and chemical composition, expressed as function of the radius on the 1D grid, are remapped on a 2- or 3-dimensional grid. Since all points at the same radius would also have the exact same value for all these variables, it is necessary to introduce some small perturbations in order to break the symmetry and seed the convective instabilities. These perturbations can be defined in different ways, usually as sinusoidal functions, but their shape does not normally have any impact on the evolution of the simulations, since they merely serve as seeds and are soon washed away by the turbulent motions, which have a chaotic nature. After triggering the perturbations, there is usually a transient phase when turbulence propagates and fills the region predicted to be convective by the 1D model; afterwards, the simulation enters a quasi-steady state.

Second, initial conditions are known to be in hydrostatic equilibrium in the 1D model, according to the assumptions I described in Sec. 3.1, but the situation might be different in the hydrodynamic model, for example because a

different equation of state is used for the gas. Thus, it is always good practice to recompute the hydrostatic equilibrium in the new hydrodynamic model before starting the simulation, and this can be done by re-calculating one of the thermodynamic variables from the others using the new equation of state employed in the code. Ignoring this step could result in artefacts during the initial transient of the simulation, such as strong expansion or contraction of the layers, that might alter the consequent evolution.
Finally, it is important to keep in mind that the evolution of the hydrodynamic simulations is dependent on the initial stratification assumed from the 1D model. Therefore, possible inaccuracies in the 1D model necessarily propagate also in the multi-D simulations. One example already mentioned in Sec. 2.2.2 is the fact that hydrodynamic simulations of convective regions with CBM prescriptions always appear to be out of equilibrium, predicting quite large entrainment rates; this can be traced back to the incorrect implementation of CBM in 1D models, which may be underestimated and cause this strong reaction in the multi-D simulations, that do not need to assume such prescriptions to reproduce the CBM.

3.4.2 Computational domain, grid and geometry

When it comes to choosing a domain configuration for hydrodynamic simulations, there are generally two possible approaches. In what is commonly know as the "box-in-a-star" setup, the domain (the "box") is fully enclosed in the star, so only a small part of the star is simulated (see Arnett & Meakin, 2016 for examples and more details). This option is simple and allows to attain higher local resolution, but it is also very limited spatially. On the other hand, the "star-in-a-box" approach involves a domain that is built to completely enclose a larger part of the star, for example the core or an entire shell (see e.g. Herwig et al., 2014), but the local resolution inevitably decreases. The choice of a particular configuration clearly depends on the problem to solve and on

the available resources.

In theory, both configurations can support a grid with either a Cartesian or a spherical coordinate system, but again the choice varies from case to case. Both options present benefits and disadvantages. A grid in Cartesian coordinates is simple and does not contain any singularity, but it also does not reflect the spherical symmetry of the problem. This might generate some artificial effects of grid-alignment that can influence the results, as found e.g. in Andrassy et al. (2020) where a strong $\ell = 3$ mode is present in the simulations, aligned with the diagonals of the cubic domain. Additionally, a Cartesian grid cannot follow multiple spatial scales at the same time, so in some cases an adaptive mesh is used, e.g. in Fryxell et al. (2000); note that the same can be done with a spherical grid. Generally, employing a Cartesian grid is most useful when modelling the stellar core (see e.g. the recent Herwig et al., 2023), to avoid the singularity in the centre of the sphere, and for simulations of shell sections with an angular size small enough that the plane-parallel approximation can be used (e.g. Cristini et al., 2017).

On the other hand, it is possible to employ a grid in spherical coordinates (radius r, polar angle θ, azimuthal angle φ), which is geometrically more accurate for stellar problems. The major issue of this choice is the presence of coordinate singularities at the origin and along the polar axis of the sphere. These singularities represent points in space where the physical size of the cells rapidly decreases. This has a strong effect on how the simulation time-step Δt is calculated in the models, which is done according to the Courant-Friedrichs-Lewy condition (Courant et al., 1928) applied to each cell of the domain:

$$\Delta t \leq C_{\max} \sum_i \frac{\Delta x_i}{v_i} \tag{3.19}$$

where i are the spatial variables, Δx_i is the width of the cell, v_i is the fluid velocity across the cell, and $C_{\max}$ is the maximum Courant number, chosen to be typically ≤ 1 ($C_{\max}$ is fixed to 0.8 in `PROMPI`). This condition, introduced to ensure convergence and avoid loss of information during the computation,

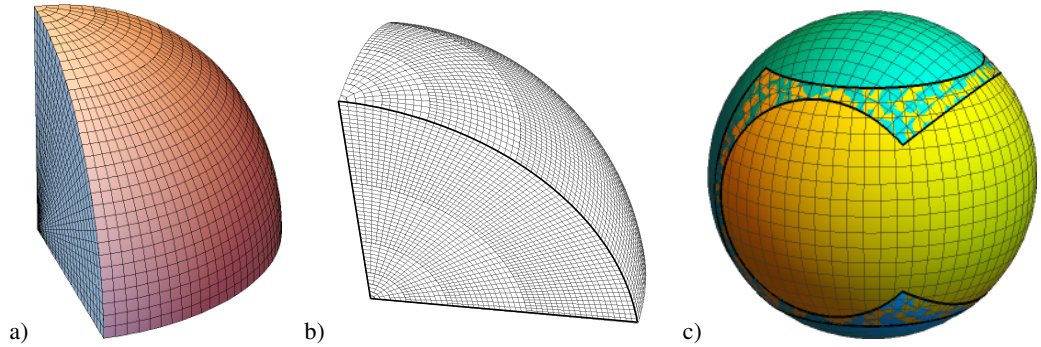

Figure 3.1: Three possible solutions to the spherical-grid singularity problem: a) coarsening the mesh in the φ-coordinate; b) "dendritic" grid, coarsening in both the θ- and φ-coordinates; c) "Yin-Yang" overset grid of Kageyama & Sato (2004). Figure taken from Müller (2020).

needs to be satisfied for every cell in the domain, so the simulation time-step is actually constrained by the cell with the smallest $\Delta x/v$ ratio. It is therefore evident that Δt becomes very short in the presence of singularities, which have very small Δx, slowing down the entire simulation.

In order to avoid this problem, researchers have suggested variations on the classic spherical grid that attempt to avoid or minimize the singularities. Some examples are illustrated in Fig. 3.1, taken from the review of Müller (2020), to which I refer for further details. One possible workaround is to artificially coarsen the mesh close to the singularities, in such a way as to produce cells with a similar size across the entire domain. This can be done either only for coordinate φ (Fig. 3.1, a) as in Müller (2015), or for both coordinates θ and φ (Fig. 3.1, b), producing the so-called "dendritic grid" used e.g. in Skinner et al. (2019). A third possibility is to assemble a new mesh from two or more patches, so that the entire spherical surface is covered but the singularities are completely avoided. An emblematic example is the "Yin-Yang" grid of Kageyama & Sato (2004) (Fig. 3.1, c), employed for hydrodynamic simulations by Wongwathanarat et al. (2010). The region of space that comes from the

overlap of the two patches is resolved through interpolation.

3.4.3 Boundary conditions

The question of choosing the appropriate boundary conditions for the simulation domain is a delicate one, and depends on the specific configuration. A popular choice is the "hydrostatic boundary conditions", in which a number of fictitious "ghost cells" are built outside the physical domain. In these cells some variables such as composition and entropy are held constant, while others like pressure and density are recomputed according to the hydrostatic equation. This ensures that the material close to the boundary remains in hydrostatic equilibrium. Additionally, if the normal component of the velocity is set to zero, we also have "wall boundary conditions", because no flow is allowed to pass through the boundary. A different possibility is having "reflecting boundary conditions", when instead the sign of the normal component of the velocity at the boundary is reversed. In this case, the incoming waves are reflected by the boundary as if impacting an impenetrable barrier. Finally, choosing "periodic boundary conditions" the properties of the fluid at one boundary are required to be equal to the ones at the opposite boundary.
The choice of which conditions to implement for each boundary can affect the physical behaviour of the simulation and it carries the risk of generating artefacts, such as the amplification of waves. Sensible choices for box-in-a-star domains are wall or reflective boundary conditions at the top and bottom boundaries of the domain, to ensure no radial flow, and periodic boundary conditions at the lateral walls, to mimic the presence of a larger environment beyond the domain. This is applicable to both Cartesian and spherical geometry.
For star-in-a-box setups, the situation can be more complicated, depending on the geometry. In spherical coordinates, it is straightforward to apply wall or reflective boundary conditions at the outermost (and potentially also at the

innermost) radius. But if the coordinates are Cartesian, it is not trivial which boundary conditions to choose considering that the star has a spherical structure within a cubic domain. A simple approach is to apply wall or reflective boundary conditions directly to the faces of the cube, if they are far enough from the region of interest. Otherwise, it is more difficult but also more accurate to fix the boundary conditions on a fictitious sphere built inside the domain, which would be containing the region of interest (e.g. Andrassy et al., 2020; Herwig et al., 2023).

Finally, it is worth mentioning that an issue arises also when boundary conditions are implemented close to coordinate singularities, i.e. the polar axis and origin in spherical coordinates. Indeed, the combination of grid singularities and improper boundary conditions can easily generate artefacts. Conventionally, reflective boundary conditions are imposed to such boundaries, to make sure that velocities do not grow uncontrollably, but in some cases it also becomes necessary to impose null velocity in the neighbouring cells. The question is indeed rather complex, so I refer to the detailed review of Müller (2020) where the interested reader can find more information.

3.4.4 Gravity

The gravitational field of a system depends on the mass distribution of its constituents. We have seen that, through the Navier-Stokes equations (3.16), the fluid motions depend on a gravitational acceleration term, which thus needs to be taken into account during the hydrodynamical computations. However, keeping track of the changes in gravity requires to include an additional equation into the system, which is not computationally convenient. Said equation is the Poisson's equation, which states:

$$\nabla^2 \Phi = 4\pi G \varrho \tag{3.20}$$

where Φ is the gravitational potential and can be used to derive the gravitational field $\boldsymbol{g} = -\boldsymbol{\nabla}\Phi$. This equation is normally solved through multipole expansion of the Green function, with 10 - 20 multipoles (Müller & Steinmetz, 1995). However, the computation can be largely simplified using only a monopole, i.e. assuming that gravity within a sphere of radius r comes from a central point mass and ignoring any non-radial fluctuation; this leads to the usual Newton's law:

$$\Phi(r) = -\frac{GM}{r}; \quad \boldsymbol{g} = -\frac{GM}{r^2}\hat{\boldsymbol{r}} \tag{3.21}$$

This is easy to solve in a hydrodynamical code, and still relatively accurate since non-radial fluctuations of density are normally rather small.

A further simplification, largely used in hydrodynamic simulations for non-explosive phases, is to hold the gravitational source term constant in time. In this way, gravity is fixed at the beginning of the simulation, usually from the mass distribution assumed from the 1D model, and it is not necessary to solve a gravity equation during the simulation, saving precious computing resources. The major limitation of this method is that, having fixed the gravity, neither contraction nor expansion of the layers is allowed. This is a very reasonable assumption for most stellar simulations, which reproduce hydrostatic phases of the stellar evolution with a time-scale that is normally much shorter than the evolutionary time-scale.

Assuming time-independent gravity and hydrostatic equilibrium, the fluid stratification is expected to be preserved over time according to $\boldsymbol{\nabla}P = -\varrho\,\boldsymbol{g}$. In reality, the numerical computation might not automatically cancel these terms, giving rise to non-zero extra flows. This problem is normally tackled through the so-called "well-balancing schemes" (Berberich et al., 2021). The choice and implementation of these schemes inextricably depends on the specific numerical method employed in the code (see Müller, 2020 and Edelmann et al., 2021 for more details). Generally, these methods allow to significantly reduce the numerical errors, guaranteeing the stratification to be preserved

over long time-scales.

3.4.5 Nuclear burning

Stellar hydrodynamic codes require a source of energy to transfer heat to the fluid and enable convective motions. The question of fuelling convection can be approached in different ways. One of the simplest solutions is to have time-independent "heating profiles" (e.g. in Jones et al., 2017), which can reproduce the energy generation profile of the 1D model, or simply concentrate the energy release in certain parts of the domain. As it happens when we fix the gravity, fixed heating profiles do not allow the stratification to change over time, but as I said this is not a problem for simulating the hydrostatic phases. However, this approach also does not allow to follow the evolution of the chemical species and model nucleosynthesis.

The more realistic approach, although more expensive, in the presence of a nuclear burning environment is to include an explicit nuclear burning routine in the simulations. This allows to reproduce nuclear energy generation across the simulation and keep track of how the chemical composition evolves over time. Differently from 1D models, only a small selection of isotopes can be included into the hydrodynamic models, due to the additional computing cost for running this nuclear subroutine. Therefore, the selection must be done carefully to ensure the presence of all the isotopes involved in the reactions that dominate the energy release. This of course depends on the burning phase that the simulations intend to reproduce.

Since for this work I am interested in massive stars and late burning phases, I will summarize here the energy-releasing reactions that occur during the more advanced burning stages, based on the studies of Arnett & Thielemann (1985) and Thielemann & Arnett (1985). As mentioned in the Introduction, helium burning is a three-body reaction ("triple alpha") that first converts two α-particles into the unstable ^{8}Be, and then before ^{8}Be has time to decay

an additional α is captured, producing the final product ^{12}C thanks to the presence of a resonant state of ^{12}C (the "Hoyle state", Hoyle, 1954), which greatly increases the probability of the reaction. In this same environment, rich in α-particles, it can also happen that α are captured by ^{12}C generating ^{16}O, and consequently captured also by ^{16}O generating ^{20}Ne. This chain can be summarized as:

$$^{4}\mathrm{He}(2\alpha,\gamma)^{12}\mathrm{C}(\alpha,\gamma)^{16}\mathrm{O}(\alpha,\gamma)^{20}\mathrm{Ne} \tag{3.22}$$

The helium-burning environment is also ideal for the production of free neutrons, which are important for the slow neutron-capture process (or "s-process"), responsible for the production of many elements beyond the iron peak. The neutron-source reaction in massive stars is ^{22}Ne(α, n)^{25}Mg, that can take place during helium burning thanks to the significant abundance of free α-particles. Specifically, the presence of ^{22}Ne is dependent on the abundance of ^{14}N from which it originates according to the α-captures:

$$^{14}\mathrm{N}(\alpha,\gamma)^{18}\mathrm{F}(\beta^{+},\nu)^{18}\mathrm{O}(\alpha,\gamma)^{22}\mathrm{Ne} \tag{3.23}$$

In turn, ^{14}N comes from the preceding CNO burning phase, for which the slowest reaction (the bottleneck) is ^{14}N(p, γ)^{15}O, therefore ^{14}N is the most abundant residue.

The alternative neutron-source reaction ^{13}C(α, n)^{16}O takes place instead in low-mass AGB stars, and is based on the production of ^{13}C via the nuclear chain:

$$^{12}\mathrm{C}(\mathrm{p},\gamma)^{13}\mathrm{N}(\beta^{+},\nu)^{13}\mathrm{C} \tag{3.24}$$

which requires free protons in a He- and C-rich environment. A promising site for this process is the formation of a ^{13}C pocket during and immediately after the "third dredge-up" in AGB stars, where free protons can diffuse from the H-rich envelope to the He- and C-rich shell underneath. Numerical simulations seem to confirm the viability of this scenario (Straniero et al., 1997; Cristallo

et al., 2009; Battino et al., 2016), although a complete understanding of this process, in particular the ingestion of the correct amount of protons, is still missing (see Herwig et al., 2011, 2014).

However, since it is already challenging to follow the neutron-capture mechanism in 1D models, given the large amount of isotopes involved, hydrodynamic simulations are not currently able to take into account such extensive and complex processes with their limited nuclear networks.

During the carbon burning, two ^{12}C nuclei are fused to produce ^{24}Mg in a highly-excited unstable state, that soon decays into ^{20}Ne or ^{23}Na, according to:

$$^{12}\mathrm{C}\left(^{12}\mathrm{C},\ \begin{matrix}\alpha\\ \mathrm{p}\end{matrix}\right)\begin{matrix}^{20}\mathrm{Ne}\\ ^{23}\mathrm{Na}\end{matrix} \tag{3.25}$$

Following these reactions, the newly formed ^{23}Na interacts with the free protons, producing:

$$^{23}\mathrm{Na}\left(\mathrm{p},\ \begin{matrix}\alpha\\ \gamma\end{matrix}\right)\begin{matrix}^{20}\mathrm{Ne}\\ ^{24}\mathrm{Mg}\end{matrix} \tag{3.26}$$

so that by the end of the carbon burning little sodium remains, and the ashes are mostly composed of neon.

Even higher temperatures trigger the photodisintegration of neon, which is more fragile than oxygen despite being heavier:

$$^{20}\mathrm{Ne}(\gamma,\alpha)^{16}\mathrm{O} \tag{3.27}$$

This is not nuclear fusion, since photodisintegration is an endothermic reaction, but the production of free α-particles triggers a set of consequent reactions that make the entire process exothermic:

$$^{20}\mathrm{Ne}(\alpha,\gamma)^{24}\mathrm{Mg}(\alpha,\gamma)^{28}\mathrm{Si} \tag{3.28}$$

so that neon burning leaves behind a composition consisting mostly of ^{16}O, ^{24}Mg and ^{28}Si.

For oxygen burning, two ^{16}O nuclei combine to produce an unstable ^{32}S, that

can decay in different combinations, the most important ones being:

$$^{16}\mathrm{O}\left(^{16}\mathrm{O},\ \begin{matrix}\alpha\\ \mathrm{p}\end{matrix}\right)\begin{matrix}^{28}\mathrm{Si}\\ ^{31}\mathrm{P}\end{matrix} \tag{3.29}$$

Secondary is the reaction ^{16}O(^{16}O, n)^{31}S(β^+, ν)^{31}P producing ^{31}S that soon decays to phosphorus. Phosphorus is also involved in ^{31}P(p, α)^{28}Si(α, γ)^{32}S. By the end of oxygen burning, the composition is mostly made of ^{28}Si and ^{32}S. If we consider the burning reactions that I summarized here, it is straightforward to see that it is possible to build a nuclear network that covers the energy generation of every phase from helium to oxygen burning making use of eleven isotopes: n, p, ^{4}He, ^{12}C, ^{16}O, ^{20}Ne, ^{23}Na, ^{24}Mg, ^{28}Si, ^{31}P, ^{32}S. This is an important point to consider, since a burning routine including these isotopes would enable hydrodynamic simulations to explicitly reproduce nuclear burning and energy generation for most stellar burning phases.

Finally, for the last hydrostatic burning phase of massive stars, the silicon burning, things are complicated by the large number and variety of isotopes and reactions involved, therefore it is difficult to build a simple burning routine to include in hydrodynamic simulations. With a simplification, we can say that during silicon burning part of the silicon and other elements photodisintegrate, releasing free α-particles:

$$^{28}\mathrm{Si}(\gamma, \alpha)^{24}\mathrm{Mg}(\gamma, \alpha)^{20}\mathrm{Ne}(\gamma, \alpha)^{16}\mathrm{O}(\gamma, \alpha)^{12}\mathrm{C}(\gamma, 2\alpha)\alpha \tag{3.30}$$

with a consequent α-capture chain that produces heavier elements up to the iron peak:

$$^{28}\mathrm{Si}(\alpha, \gamma)^{32}\mathrm{S}(\alpha, \gamma)^{36}\mathrm{Ar}(\alpha, \gamma)^{40}\mathrm{Ca}(\alpha, \gamma)^{44}\mathrm{Ti}(\alpha, \gamma)^{48}\mathrm{Cr}(\alpha, \gamma)^{52}\mathrm{Fe}(\alpha, \gamma)^{56}\mathrm{Ni} \tag{3.31}$$

This happens in addition to the production of other important nuclei such as ^{27}Al, ^{30}Si, ^{34}S, ^{35}Cl, ^{38}Ar, ^{49}K, ^{42}Ca, ^{48}Ti, ^{52}Cr and much more. The silicon burning is challenging to model also because of the consequent advent of the nuclear statistical equilibrium, as mentioned in Sec 1.1, and the presence

of quasi-equilibrium groups before that, making the computation even more difficult (see Thielemann & Arnett, 1985, for further details). One emblematic example is the 25-isotope network used in hydrodynamic simulations by Meakin & Arnett (2007) and Mocák et al. (2018).

3.5 The PROMPI code

PROmetheus MPI (PROMPI, Meakin & Arnett, 2007) is a multi-dimensional hydrodynamic code specifically designed to model turbulent motions in stellar interiors. It is based on the PROMETHEUS code by Fryxell et al. (1989), but it has been improved by Meakin & Arnett (2007) for parallel computing through domain decomposition with the Message Passing Interface (MPI) libraries, hence the name. The code represents an Eulerian implementation of the numerical scheme called "piecewise parabolic method", introduced by Colella & Woodward (1984), which employs a Riemann solver for a gas with a general equation of state (Colella & Glaz, 1985).

PROMPI is implemented to solve a set of equations that determine the motion of the fluid over time. The key variables that are traced across the grid are density ϱ, pressure P, temperature T, velocity $\boldsymbol{v}$ (which is made of 2 or 3 components), total specific energy $E = E_{\mathrm{K}} + E_{\mathrm{I}}$ composed of kinetic and internal energy, and chemical composition represented by the mass fraction X_i for a number of species $i = 1, ..., I$. This set of $5 + I$ variables is solved through a system of $5 + I$ equations:

$$
\begin{cases}
\dfrac{D\varrho}{Dt} = -\varrho\,\boldsymbol{\nabla}\cdot\boldsymbol{v} & \text{mass conservation} \\
\dfrac{D\boldsymbol{v}}{Dt} = -\dfrac{1}{\varrho}\boldsymbol{\nabla}P + \boldsymbol{g} & \text{momentum conservation} \\
E = \dfrac{1}{2}v^2 + E_{\mathrm{I}}\left(T, \varrho, X_i\right) & \text{energy definition} \\
\dfrac{DE}{Dt} = -\dfrac{1}{\varrho}\boldsymbol{\nabla}\cdot\left(P\boldsymbol{v}\right) + \boldsymbol{v}\cdot\boldsymbol{g} + \varepsilon_{\mathrm{n}} - \varepsilon_{\nu} & \text{energy conservation} \\
P = P\left(T, \varrho, X_i\right) & \text{equation of state} \\
\dfrac{DX_i}{Dt} = \dfrac{m_i}{\varrho}\left(\displaystyle\sum_j R_{j,i} - \sum_k R_{i,k}\right) & \text{nuclear burning, } i \in [1, I]
\end{cases}
\tag{3.32}
$$

where I used the total derivative notation $\dfrac{D}{Dt} := \dfrac{\partial}{\partial t} + \boldsymbol{v}\cdot\boldsymbol{\nabla}$, which describes the temporal change of a quantity under the velocity field $\boldsymbol{v}$. As before, ε_{n} is the nuclear energy release rate, ε_{ν} the neutrino loss rate, m_i the species mass, and $R_{a,b}$ the rate of the reaction that transforms species $a \to b$.

We have already seen these equations. Many of them are simply the multi-dimensional generalization of the stellar equations we found in (3.1), with the space and time derivatives replaced by the total derivative. For example, in the nuclear burning equation the advection term is included in the total derivative, so it does not appear on the right-hand side. The equation of momentum conservation is the Euler's equation we have seen in (3.8), i.e. the Navier-Stokes equation (3.16) with no viscosity. We can neglect viscosity here since `PROMPI` follows the ILES framework, as described in Sec. 3.3. Another requirement of the ILES framework is that energy conservation must be imposed, as viscosity progressively converts kinetic into internal energy (see Sec. 3.3). This is done in `PROMPI` in the following way. From (3.32), the total energy consists of the sum of the specific kinetic and specific internal energy. At each time-step, the kinetic energy is recomputed from the velocity magnitude, while the internal energy is obtained subtracting the kinetic from the total energy at the previous

time-step; then, the internal energy is updated with the contributions from nuclear sources and neutrino losses. These steps ensure that the total energy is always exactly the sum of the kinetic and internal energy, so any variation in kinetic energy is promptly included into E_{I}.
Additionally, PROMPI can include an extra term $-\frac{1}{\varrho}\boldsymbol{\nabla}\cdot\boldsymbol{F}_r$ inside the energy conservation equation to represent radiative dissipation, with the radiative flux $\boldsymbol{F}_r = -\kappa\boldsymbol{\nabla}T$ and the opacity κ, but this is not needed for the late burning phases I am modelling here, in which the cooling is dominated by neutrino diffusion (ε_ν) instead. PROMPI can also include a time-dependent gravitational field, as I described in Sec. 3.4.4; in this case $\boldsymbol{g}$ is also a variable, and the additional equation for its computation is:

$$\boldsymbol{g} = -\frac{GM(r)}{r^2}\,\hat{r} \quad ; \quad M(r) = \int_0^r \bar{\varrho}(x)\; 4\pi x^2\; \mathrm{d}x \tag{3.33}$$

where we assume spherical symmetry for the mass distribution $M(r)$, therefore we integrate the average density $\bar{\varrho}(r)$ which depends solely on the radius, ignoring any non-radial fluctuations.
The PROMPI code has been successfully used over the years to investigate a variety of convective stellar environments. I will recall here the notable works conducted with PROMPI on modelling the hydrogen-core burning (Meakin & Arnett, 2007), carbon-shell burning (Cristini et al., 2017, 2019), oxygen-shell burning (Meakin & Arnett, 2007; Arnett et al., 2009; Viallet et al., 2013), shell merging (Mocák et al., 2018) and convective envelope of a red giant star (Viallet et al., 2013).

3.5.1 Problem setup options

Among the many configuration options implemented in the PROMPI code, I shall describe here briefly the ones selected for the hydrodynamic simulations I present in this work. All models have a box-in-a-star design, therefore they present periodic boundary conditions at the lateral faces of the box, and reflec-

tive ones for the top and bottom bases. Both Cartesian and spherical systems of coordinates have been used, and since our domains are distant from the centre and polar axis of the star, the grid does not have any problem with singularities. Furthermore, when Cartesian coordinates were employed the gravitational field has been fixed as a constant profile, but with spherical coordinates the gravity has been recomputed at every time-step from the density distribution, therefore allowing for contraction or expansion of the layers.
Concerning the nuclear burning routines, for the neon-shell plane-parallel simulations of Chapter 4 a simple network of 5 isotopes has been used (see Sec. 4.1.1 for the details), but for the neon-shell spherical simulations and the shell-merging simulations of Chapter 5 and 6 the 11-isotope network presented in Sec. 3.4.5 has been used. As I described there, this network allows to reproduce the energy generation in all the late phases before silicon burning, which is particularly useful when having multiple burnings within the same simulation, as in the case of Chapter 6. The nuclear reaction rates have been assumed from the most recent library of the `JINA REACLIB` database[2] (Cyburt et al., 2010). Regarding the equation of state used to describe the gas in the simulations, the "Helmholtz" equation of state has been employed (Timmes & Arnett, 1999; Timmes & Swesty, 2000). It assumes an ideal gas of ions, a Planck distribution of the photon energies, and an electron-positron gas with arbitrary degrees of relativity and degeneracy. The equation takes in temperature, density and chemical composition as input, and returns pressure, internal energy, entropy and several other quantities. Cooling by neutrino losses is a by-product of a number of reactions (pair creation, plasma reactions, bremsstrahlung, recombination); it is taken into account employing the analytical formula of Beaudet et al. (1967).

[2] `https://reaclib.jinaweb.org`

3.5.2 Mean-field analysis

The output of a multi-D simulation are normally large datafiles, saved at regular time intervals, that store a certain number of variables for every cell of the grid. These files can be very large and occupy a significant amount of storage memory, up to tens of terabytes. This creates not only a problem of data storage, but also of data analysis, since it can be expensive and time-consuming to import and analyse these large datasets. Generally, an important part of the data analysis of multi-D simulations is done through space and time averaging, which requires first to import the data from the multi-D datafiles and then perform the averaging.

A useful feature of the `PROMPI` code is the possibility of performing a data averaging already on the fly, while the simulation is running. Angularly averaged variables as function of the radius are saved in dedicated datafiles while the code is still running, and they can be between 100 - 1000 times smaller compared to the full-size datafiles. This method not only has the effect of making the storage and analysis of the files much easier, but it also allows to save information that otherwise would be lost. Indeed, all datafiles are saved after a certain time interval, but the mean-field time averaging in `PROMPI` includes all the averages after each time-step; therefore, the 1D-averaged datafiles include information from all the intermediate time-steps that is not saved when the datafiles are produced.

For performing a mean-field statistical analysis, `PROMPI` makes use of the so-called "Reynolds-Averaged Navier-Stokes" (RANS) framework. This has been implemented in `PROMPI` by Mocák et al. (2014) and first employed for simulation analysis in Mocák et al. (2018). The RANS framework is based on the combination of two types of averaging, a time averaging and a horizontal or angular averaging, depending on the coordinate system. For a quantity q that varies with position $\boldsymbol{r}$ and time t, we can define the Reynolds average at radius

r as:

$$\overline{q}(r) = \frac{1}{T\Delta S}\int_0^T \int_{\Delta S} q(\boldsymbol{r},t)\ \mathrm{d}t\ \mathrm{d}S \tag{3.34}$$

having performed both a time averaging over the time window T, and a horizontal/angular average over ΔS, which is either the surface of the horizontal plane or the solid angle of the shell. The surface elements for Cartesian coordinates are $\mathrm{d}S = \mathrm{d}x\,\mathrm{d}y$, while the solid angle elements for spherical coordinates are $\mathrm{d}S = \sin\theta\,\mathrm{d}\theta\,\mathrm{d}\varphi$.

Another type of averaging, the Favre average, is defined as

$$\widetilde{q} = \frac{\overline{\varrho q}}{\overline{\varrho}} \tag{3.35}$$

which represents a density-weighted Reynolds average. Therefore, using these definitions it is possible to perform the mean-field analysis by decomposing the variables into their Reynolds or Favre mean and fluctuations, according to:

$$q = \overline{q} + q' \quad ; \quad q = \widetilde{q} + q'' \tag{3.36}$$

where $\overline{q}, \widetilde{q}$ are the means and q', q'' the fluctuations of a quantity q (see Mocák et al., 2014, 2018 for additional details). The general properties of the mean also apply here: $\overline{a+b} = \overline{a} + \overline{b}$, $\overline{ab} \neq \overline{a}\,\overline{b}$ and similarly for the Favre average. Therefore, taking the Reynolds and Favre averages of (3.36) respectively gives:

$$\overline{q} = \overline{\overline{q} + q'} = \overline{q} + \overline{q'} \quad ; \quad \widetilde{q} = \widetilde{\widetilde{q} + q''} = \widetilde{q} + \widetilde{q''} \tag{3.37}$$

therefore $\overline{q'} = 0$ and $\widetilde{q''} = 0$ by construction, as expected for fluctuations.

To show the effectiveness of this formalism, I will give here a meaningful example. In the RANS equations, the turbulent flux f_q of a quantity q in an environment with density ϱ and velocity v is given by $f_q = \overline{\varrho}\,\widetilde{q''v''}$. To calculate this flux directly from the means of the quantities ϱ, q, v, we can expand this definition using the properties described above:

$$\begin{aligned} f_q = \overline{\varrho}\,\widetilde{q''v''} &= \overline{\varrho}\,\widetilde{(q-\widetilde{q})(v-\widetilde{v})}\ = \overline{\varrho}\,(\,\widetilde{qv} - \widetilde{q\widetilde{v}} - \widetilde{\widetilde{q}v} + \widetilde{\widetilde{q}\widetilde{v}}\,) = \\ &= \overline{\varrho}\,(\,\widetilde{qv} - \widetilde{q}\widetilde{v} - \widetilde{q}\widetilde{v} + \widetilde{q}\widetilde{v}\,) = \overline{\varrho}\,(\,\widetilde{qv} - \widetilde{q}\widetilde{v}\,) = \overline{\varrho qv} - \overline{\varrho q}\ \overline{\varrho v}/\overline{\varrho} \end{aligned} \tag{3.38}$$

In this way, we are able to express the turbulent flux in terms of Reynolds averages, which are the ones that PROMPI computes and saves on the fly during its mean-field analysis. I will make use of this result in the following chapters, when I will compute the turbulent fluxes in the simulations.

Thanks to the RANS framework and its implementation in PROMPI, I was able to run part of the analysis directly on the 1D-averaged radial profiles of the simulations, without having to perform any laborious post-processing averaging on the large 3D datafiles. In this thesis, the plots that include radial profiles have been obtained with this RANS framework analysis, making use of the dedicated open-source code RANSX[3].

[3] https://github.com/mmicromegas/ransX

4 Entrainment in 3D simulations of a neon-burning shell

4.1 Motivations and overview

As I described in Chapter 3, hydrodynamic simulations of stellar convection can be computationally very expensive since turbulence occurs over very short time-scales compared to the stellar evolutionary time-scales, especially for the early burning phases, so it is hard to simulate a significant fraction of a burning stage in 3D. This is because the time-steps of the simulations are limited by the CFL condition (see Sec. 3.4.2), therefore by the sound speed in the fluid. The Mach number, which is the convective flow speed over sound speed in the fluid, strongly depends on the evolutionary phase, being as small as 10^{-4} for the main-sequence core burning and reaching values up to 10^{-1} for the final burning phases (e.g. Yoshida et al., 2021). Therefore, the modelling approach must be different depending on the phase and environment studied, especially since low-Mach-number flows are expensive and difficult to model for most solving schemes (see e.g. Miczek, 2013; Leidi et al., 2022). While it is still possible to reproduce the late oxygen and silicon convective phases for short time-scales without altering the initial conditions (Couch & Ott, 2015; Müller et al., 2017; Yoshida et al., 2019), for the earlier phases the common approach is to artificially increase the convective velocities by boosting the energy release, which is also called "luminosity boosting". This procedure alters the fluid velocity in the simulations, that is expected to follow the scaling $v \propto L^{1/3}$ according to Biermann (1932) and Kolmogorov (1941), and it introduces important differences from the 1D stellar model assumed for initial conditions. Since the luminosity boosting is the only way to make most hydrodynamic simulations of stellar convection possible and affordable to run, it is always worth investigating whether this modification only affects the velocity magni-

tude and therefore the simulation time-scale, or if additional effects arise in the fluid physics.

The neon-burning phase is a good compromise in this sense: it is not as extreme as the oxygen or silicon burning, which are highly dynamical and might show some differences from the previous hydrostatic phases; but it is still vigorous enough to have a short lifetime and a rapid evolution, making it possible to reproduce it with hydrodynamic models, assuming that enough computing resources are allocated. Simulating a burning shell rather than a burning core presents some advantages, because shells are often more dynamical environments, have shorter lifetimes, and present two convective boundaries that can be studied, an upper and a lower one, for the price of one simulation. In particular, neon-burning regions are relatively small, with a typical spatial extent of $\sim 10^8$ - 10^9 cm, and a lifetime of weeks to months. Of course, the possibility of modelling a neon-burning shell in multi-D depends on the 1D stellar model used for initial conditions: does a convective neon shell form at all? Is it stable enough that its turbulent motions can be studied? Does it live for long enough to witness convective boundary mixing?

For this study, I have analysed a set of simulations of a neon-burning shell in a 15 $M_\odot$ star; the results of this analysis have been published in Rizzuti et al. (2022). Specifically, the bulk of the simulations has been run by collaborators employing a 3D hydrodynamic model, while I was entirely responsible for the analysis and publication of the results. The simulations have been started from the same initial conditions but test different resolutions and boosting factors, to study the dependence of the results on these assumptions. From the results of these simulations, I studied the development and evolution of convection, with particular attention to convective boundary mixing and entrainment of stable material into the convective zone.

4.1.1 Setup of the simulations

All hydrodynamic simulations have been started from the same initial conditions, which were assumed from a stellar evolution model of a 15 $M_\odot$ star at solar metallicity ($Z = 0.014$), run with the `GENEC` code (Eggenberger et al. 2008) from the zero-age main sequence to the start of silicon burning with the options described in Ekström et al. (2012). Among these, it is worth mentioning that the Schwarzschild criterion was used to predict the convective boundary location, and penetrative overshoot was included only for core-hydrogen and core-helium burning phases with $\alpha_{\rm ov} = 0.1$, as I described in Sec 2.2.1. For carbon-burning and afterwards, an α-chain network was used (Hirschi et al., 2004).

The time-evolution diagram of the stellar model is presented in Fig. 4.1. The neon shell used as initial conditions to start the 3D simulations is indicated by the red arrow, and also shown in more detail in Fig. 4.2. We can see from the isomass contours of this figure that the neon shell does not undergo any significant contraction or expansion during its evolution. Additionally, the physical time of the 3D simulations is always less than one hour, much shorter than the evolutionary time-scale of this shell. The radial profiles of some key variables (temperature, density, nuclear energy and neutrino loss rates) are plotted in Fig. 4.3; in particular, it is possible to see the temperature inversion at the bottom of the convective zone ($r \sim 3.55 \times 10^8$ cm) caused by the fact that the neutrino energy loss is larger than the nuclear energy generation in the core after core-oxygen burning.

From the 1D `GENEC` model, the key variables density, pressure, temperature, entropy, mass, and chemical composition have been remapped on a tridimensional Cartesian grid, after having recomputed the hydrostatic equilibrium according to the Timmes equation of state used in `PROMPI`. Specifically, the equation of state is used to calculate the entropy, that is missing from the `GENEC` model, and to recalculate the temperature from the other ther-

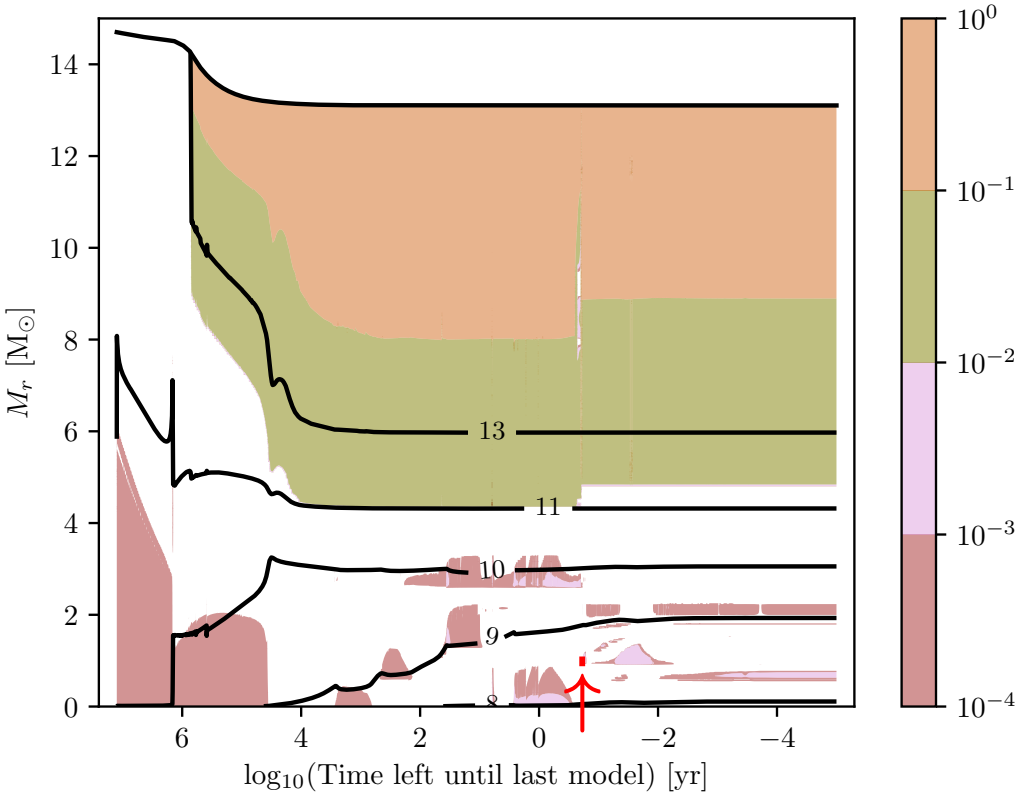

Figure 4.1: Structure evolution diagram of the input model, a 15 M$_\odot$ 1D `GENEC` model: horizontal axis is the time left until the predicted collapse of the star in log scale; vertical axis is the mass coordinate; black lines are radial contours with numbers indicating $\log_{10}(r)$ in cm; shaded areas are convective regions with Mach number in colour scale. The red arrow points to the neon shell simulated in 3D. Figure taken from Rizzuti et al. (2022).

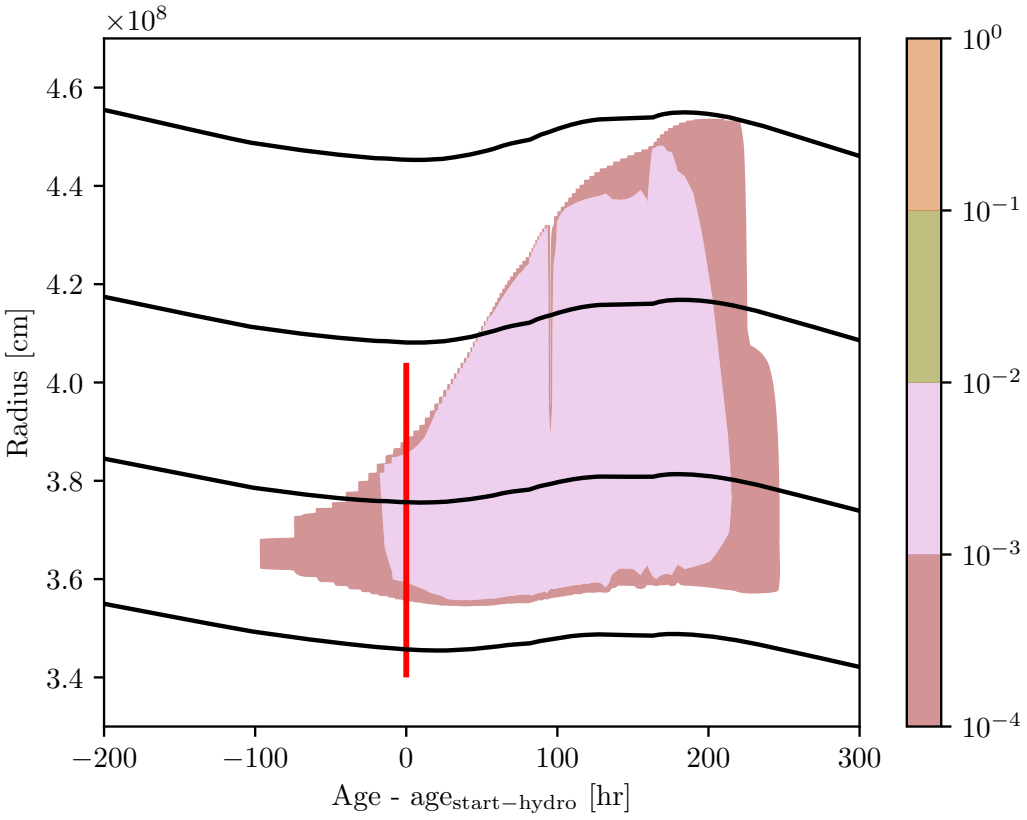

Figure 4.2: Zoom-in of the neon shell from the 1D `GENEC` model: horizontal axis is the time from the start of the 3D simulations; vertical axis is the radius in units of 10^8 cm; black lines are isomass contours for $M_r = 0.9, 1.0, 1.1, 1.2$ $M_\odot$; shaded areas are convective regions with Mach number in colour scale. The vertical red bar is the radial extent of the 3D simulations. Figure taken from Rizzuti et al. (2022).

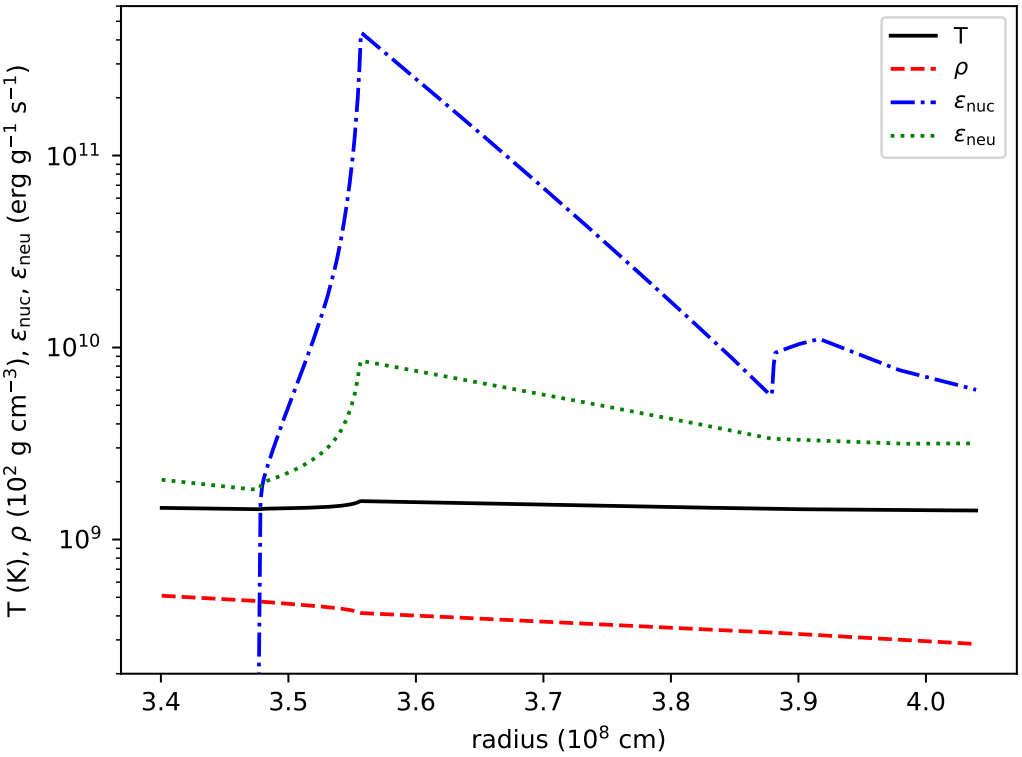

Figure 4.3: Initial profiles from the 1D `GENEC` input model: temperature (T, solid black line), density (ϱ, red dashed line), nuclear energy generation rate ($\varepsilon_{\rm nuc}$, blue dot-dashed line), and neutrino energy loss rate ($\varepsilon_{\rm neu}$, green dotted line). Figure taken from Rizzuti et al. (2022).

modynamic variables, in addition to calculating some partial derivatives used below. Then, the density profile is integrated radially onto the new 3D grid, starting from the bottom of the domain, by using the equation:

$$\frac{\mathrm{d}\varrho}{\mathrm{d}r} = \frac{\partial\varrho}{\partial s}\frac{\mathrm{d}s}{\mathrm{d}r} + \frac{\partial\varrho}{\partial P}\frac{\mathrm{d}P}{\mathrm{d}r} + \frac{\partial\varrho}{\partial A}\frac{\mathrm{d}A}{\mathrm{d}r} + \frac{\partial\varrho}{\partial Z}\frac{\mathrm{d}Z}{\mathrm{d}r} \tag{4.1}$$

where the partial derivatives have been obtained from the equation of state, and the hydrostatic condition is applied: $\mathrm{d}P/\mathrm{d}r = -\varrho\, g$. Gravity is a time-independent function of the radius, expressed as an analytical fit from the 1D model:

$$g(r[\mathrm{cm}]) = -\sum_{n=0}^{7} a_n\, r^n \,\mathrm{cm\ s^{-2}}, \tag{4.2}$$

with the following coefficients used:

$a_0 = 1.389\,869\,06 \times 10^{14}$	$a_1 = -\,2.611\,254\,76 \times 10^{6}$
$a_2 = 2.101\,117\,88 \times 10^{-2}$	$a_3 = -\,9.386\,056\,09 \times 10^{-11}$
$a_4 = 2.514\,064\,18 \times 10^{-19}$	$a_5 = -\,4.037\,712\,06 \times 10^{-28}$
$a_6 = 3.600\,322\,41 \times 10^{-37}$	$a_7 = -\,1.374\,975\,79 \times 10^{-46}$

Overall, the variables recomputed with this method result very close to the original 1D model ones, having a relative difference that is below 1 per cent. These variables have been mapped on a cubic Cartesian grid with a side of 0.64×10^8 cm, with the radius spanning the range 3.40 - 4.04×10^8 cm. Some small seed perturbations are added to trigger convective instability: in each cell between $3.6 < r < 3.8 \times 10^8$ cm, i.e. the predicted convective zone, the values of density and temperature are modified in the following way:

$$\varrho \to \varrho\,(1 + rand) \quad ; \quad T \to T/\,(1 + rand) \tag{4.3}$$

where *rand* is a random number between -2.5 and $+2.5 \times 10^{-7}$, different for each cell. This method was chosen because it is the same one that has been applied in Cristini et al. (2017, 2019); it ensures that the perturbations are

much smaller than the original values (relative difference smaller than 10^{-13}), and the product $\varrho \cdot T$ remains constant.

For the domain boundaries, reflective boundary conditions in the vertical direction and periodic boundary conditions in the horizontal directions have been assumed. Additionally, near the lower boundary a velocity-damping region has been included between $3.40 < r < 3.46 \times 10^8$ cm, in order to mimic the downward propagation of low-speed gravity waves according to the method described in Cristini et al. (2017). Specifically, the velocity magnitude is multiplied by a damping factor, which depends on the radial position r, according to:

$$v \to v \cdot \frac{1}{1 + \mathrm{d}t \cdot \omega \cdot f_\mathrm{d}} \quad ; \quad f_\mathrm{d} = \frac{1}{2}\left(\cos\left(\pi \frac{r - r_\mathrm{i}}{r_\mathrm{o} - r_\mathrm{i}}\right) + 1\right) \tag{4.4}$$

where $\mathrm{d}t$ is the time-step of the simulation, $\omega = 0.01$ is the damping frequency, and $r_\mathrm{i} = 3.4 \times 10^8$ cm, $r_\mathrm{o} = 3.46 \times 10^8$ cm. This damping is present during the entire simulation and always at the same radii.

Finally, convection has been driven in the 3D simulations using an explicit nuclear network of five isotope: ^{4}He, ^{16}O, ^{20}Ne, ^{24}Mg, ^{28}Si. The abundance of ^{4}He is assumed to be always at nuclear equilibrium, a reasonable assumption for late burning stages. As I described in Sec. 3.4.5, these isotopes are involved in the neon-burning nuclear reactions $^{20}\mathrm{Ne}(\gamma,\alpha)^{16}\mathrm{O}$ and $^{20}\mathrm{Ne}(\alpha,\gamma)^{24}\mathrm{Mg}$, and in the secondary reaction $^{24}\mathrm{Mg}(\alpha,\gamma)^{28}\mathrm{Si}$, allowing not only to fuel convection with nuclear energy, but also to study the nucleosynthesis of these species. At the beginning of each simulation, the nuclear burning at the bottom of the convective shell triggers the turbulent motions, gradually filling the region of space predicted to be convective in the 1D input model. After this initial transient, convection has fully developed and the simulation enters what can be called the "quasi-steady state" regime.

From the initial conditions obtained as just described, I have run a set of 3D simulations with different resolution and luminosity boosting, combining the three grids of 128^3, 256^3, 512^3 cells with the three boosting factors 1, 10, 100

Table 4.1: Properties of the 3D hydrodynamic simulations presented in this chapter: model name; resolution N_{xyz}; boosting factor of the driving luminosity ε; starting $\tau_{\rm start}$ and ending $\tau_{\rm end}$ time of the quasi-steady state; convective turnover time $\tau_{\rm c}$; number of convective turnovers simulated in the quasi-steady state $n_{\rm c}$; root-mean-square convective velocity $v_{\rm rms}$; sonic Mach number Ma; cost required to run the simulation in CPU core-hours.

name	N_{xyz}	ε	$\tau_{\rm start}$ (s)	$\tau_{\rm end}$ (s)	$\tau_{\rm c}$ (s)	$n_{\rm c}$	$v_{\rm rms}$ (10^6 cm/s)	Ma (10^{-3})	cost (10^6 hr)
Ex1_128	128^3	1	2500	3006	230	2	0.28	0.21	0.08
Ex10_128	128^3	10	250	1502	50	25	1.58	4.53	0.04
Ex100_128	128^3	100	100	250	25	6	3.42	9.60	0.01
Ex1_256	256^3	1	2500	5000	127	20	0.56	1.51	1.00
Ex10_256	256^3	10	250	1832	47	34	1.70	4.44	0.36
Ex100_256	256^3	100	98	251	23	7	3.62	10.1	0.11
Ex1_512	512^3	1	2500	3202	98	7	0.70	1.93	11.4
Ex10_512	512^3	10	250	1004	49	15	1.49	3.96	4.66
Ex100_512	512^3	100	96	251	22	7	3.72	9.95	1.15
Ex1000_512	512^3	1000	17	24	9	1	8.00	23.2	0.28
Ex10_1024	1024^3	10	500	811	49	6	1.49	3.94	48.2

times the nominal case. When a boosting in luminosity is present, all the nuclear reaction rates have been multiplied by the boosting factor, including the neutrino cooling rate. The complete list of simulations is presented in Table 4.1, identified by code names that summarize the boosting factor `Ex` followed by the resolution. Two additional simulations have also been run: a high-boosting `Ex1000_512` simulation with resolution 512^3 and boosting factor 1000, and a high-resolution simulation `Ex10_1024` with resolution 1024^3 and boosting factor 10. Due to the high computing cost, the latter has been restarted from the `Ex10_512` simulation after 500 s.

4.2 The turbulent regime

In Table 4.1, I present the list of simulations run for this study, complete of their most important properties. In addition to listing the model features, which include the resolution, boosting factor, starting and ending time of the quasi-steady state, I also made use of the `RANSX` library and computed the convective turnover time τ_c, which is the time taken by the flow to cover twice the radial extent of the convective zone, the number of convective turnovers in the quasi-steady state, the convective root-mean-square velocity $v_{\rm rms}$, the sonic Mach number defined as $v_{\rm rms}$ over sound speed, and the cost of each simulation in CPU core-hours.

From the table, it is possible to draw some interesting conclusions regarding the effects of the resolution and luminosity boosting on the simulations. Generally, simulations with different resolution but same boosting factor tend to have similar properties, with the exception of the simulations with a resolution of 128^3, which seem to have lower $v_{\rm rms}$ than their higher-resolution counterparts, hinting that at this low resolution the fluid motions are not converged upon grid refinement yet. However, one must keep into account that simulations run for longer time-scales have higher $v_{\rm rms}$ because they built larger kinetic energies over time.

On the other hand, the boosting factor has a strong effect on sets of simulations with the same resolution, increasing the convective velocities and Mach number, and therefore decreasing the convective turnover time. The predicted scaling $v_{\rm rms} \propto \varepsilon^{1/3}$ (Biermann, 1932; Kolmogorov, 1941) and therefore $\tau_c \propto v_{\rm rms}^{-1} \propto \varepsilon^{-1/3}$ seem to hold well in these simulations.

In order to study the flow regime, it is possible to calculate a characteristic number associated with the fluid called the "Reynolds number" or Re (Reynolds, 1883). This number represents the ratio between the inertial and the viscous forces in the fluid, so its value can help determine if the flow is laminar or turbulent, with the threshold between the two regimes usually es-

timated around Re $\sim 2 \times 10^3$ (Durst & Ünsal, 2006; Pavelyev et al., 2003). In real stars the Reynolds number, that depends on the viscosity of the fluid, is normally on the order of Re $\sim 10^9$ or more (see Arnett & Meakin, 2016). However, stellar hydrodynamic simulations do not resolve the viscous scale, but rather rely on the numerical viscosity (see Sec. 3.3); therefore, it is more correct in this context to talk of an "effective Reynolds number" that can be defined in the following way.

We start from the definition of the Reynolds number $\mathrm{Re} = v\,\ell/\nu$, where v is the flow velocity, ℓ the flow characteristic length, and ν the viscosity. We can assume that the numerical viscosity, which dimensionally is a velocity times a length, has an expression of the type $\nu = \Delta v\,\Delta x$, where Δx is the typical grid cell size and Δv the fluid velocity across this cell. Finally, we can define two different energy dissipation rates, one for the largest scales $\varepsilon_\ell = v^3/\ell$ and one for the grid scale $\varepsilon_{\Delta x} = \Delta v^3/\Delta x$, and we know from Kolmogorov (1941) that the dissipation rates must be equal at all scales. Combining everything together, we can finally estimate the effective Reynolds number as $\mathrm{Re}_{\mathrm{eff}} = (\ell/\Delta x)^{4/3}$. If we assume that ℓ is the size of the convective zone, then the ratio $\ell/\Delta x$ simply becomes the number of cells used for resolving the convective zone. In this way, $\mathrm{Re}_{\mathrm{eff}}$ is resolution-dependent, which is logically consistent with the ILES assumption that the numerical grid mimics the effects of viscosity.

In my simulations, $\mathrm{Re}_{\mathrm{eff}}$ and the number of cells that resolve the convective shell depend on each simulation and on the specific time frame. Indicative values for simulations with resolution 128^3 are 250 - 350, for 256^3 are 700 - 900, for 512^3 are 1800 - 2300, and for 1024^3 is 4800. According to these numbers and to the threshold value for a turbulent regime Re ~ 2000, choosing a resolution of 128^3 or 256^3 for the simulations could result in a regime which is not fully turbulent, while 512^3 and 1024^3 can be considered acceptable. Indeed, for the analysis of the results I focused here on the set of simulations with resolution 512^3, which are highly detailed and reproduce enough convective turnovers to be statistically significant.

4.3 Dynamics of the fluid motions

To make a first, meaningful comparison between the 1D and the 3D models, I present in Fig. 4.4 the radial profiles of different velocity components. The black line is the convective velocity predicted by the 1D model according to the mixing-length-theory (see Sec. 2.1.1); the coloured lines are horizontally averaged velocity components from the 3D simulation `Ex1_512`, averaged over one convective turnover. The 1D mixing-length-theory velocity is approximately half of the 3D root-mean-square velocity obtained in the hydrodynamic simulation: this means that the strength of the turbulent motions is underestimated in 1D. The convective velocity at the beginning of the 3D model (in red) is slightly smaller compared to the one at the end of the simulation (in blue, solid), where the upper boundary is also visibly shifted outwards as expected from entrainment. The radial component of the convective velocity (blue dotted line) has a maximum at the centre of the cell, while the horizontal component (blue dashed line) is larger closer to the boundaries, reflecting the fact that the fluid elements under convection move radially in the bulk of the convective zone, and turn to move horizontally at the boundaries.

It is always useful to have a visual representation of the simulation evolution; hence, I display in Fig. 4.5 some vertical cross-sections of simulation `Ex1_512` taken at different time-steps throughout the simulation, with the fluid speed in colour scale. What we can see here is that as the simulation evolves the nuclear burning drives the turbulent motions, which start filling the convective region predicted by the 1D input model. The duration of this initial transient in the simulations depends on the fluid speed and therefore on the boosting factor, but after convection is fully developed in the shell the simulation is in the quasi-steady state and can be analysed.

I also present in Figure 4.6 the cross-sections of the four different simulations `Ex10_128`, `Ex10_256`, `Ex10_512`, `Ex10_1024`, which have the same boosting factor but different resolution. This figure shows very well the impact of the

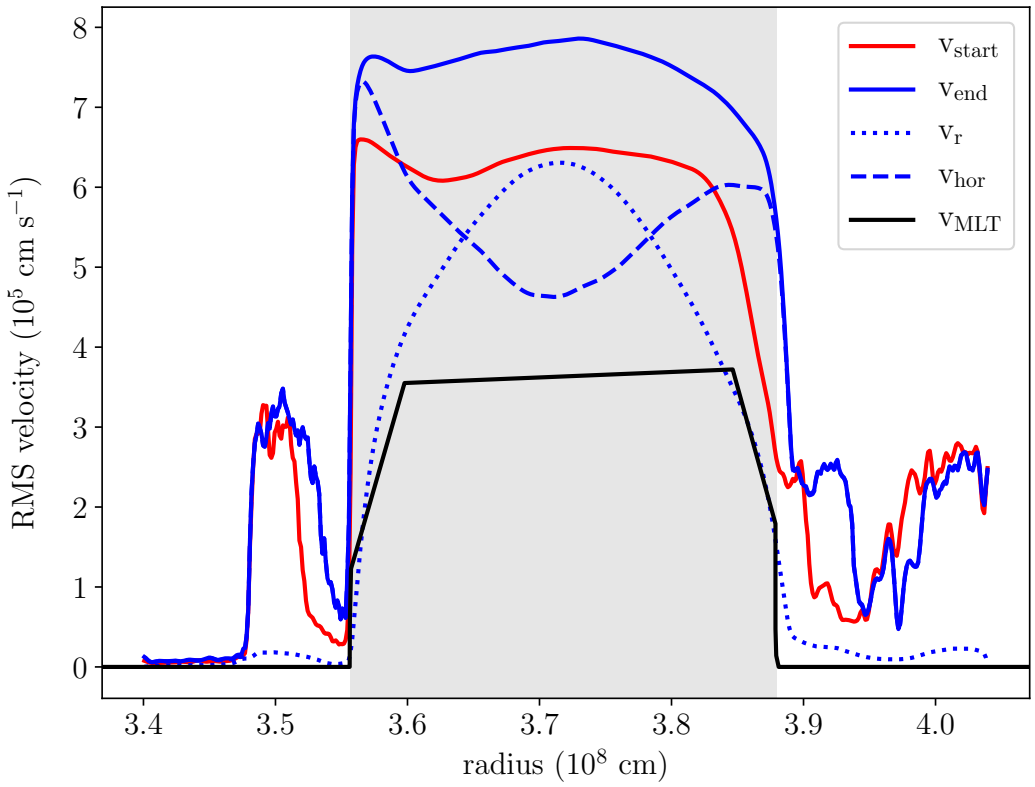

Figure 4.4: Radial profiles of different velocity components: in black, the mixing-length-theory velocity of the 1D model; in red, the root-mean-square velocity at the beginning of `Ex1_512`; in blue solid, the root-mean-square velocity at the end of `Ex1_512`; in blue dotted and dashed, the radial and horizontal components of v_{end} respectively. The shaded area is the convective zone according to the 1D stellar model.

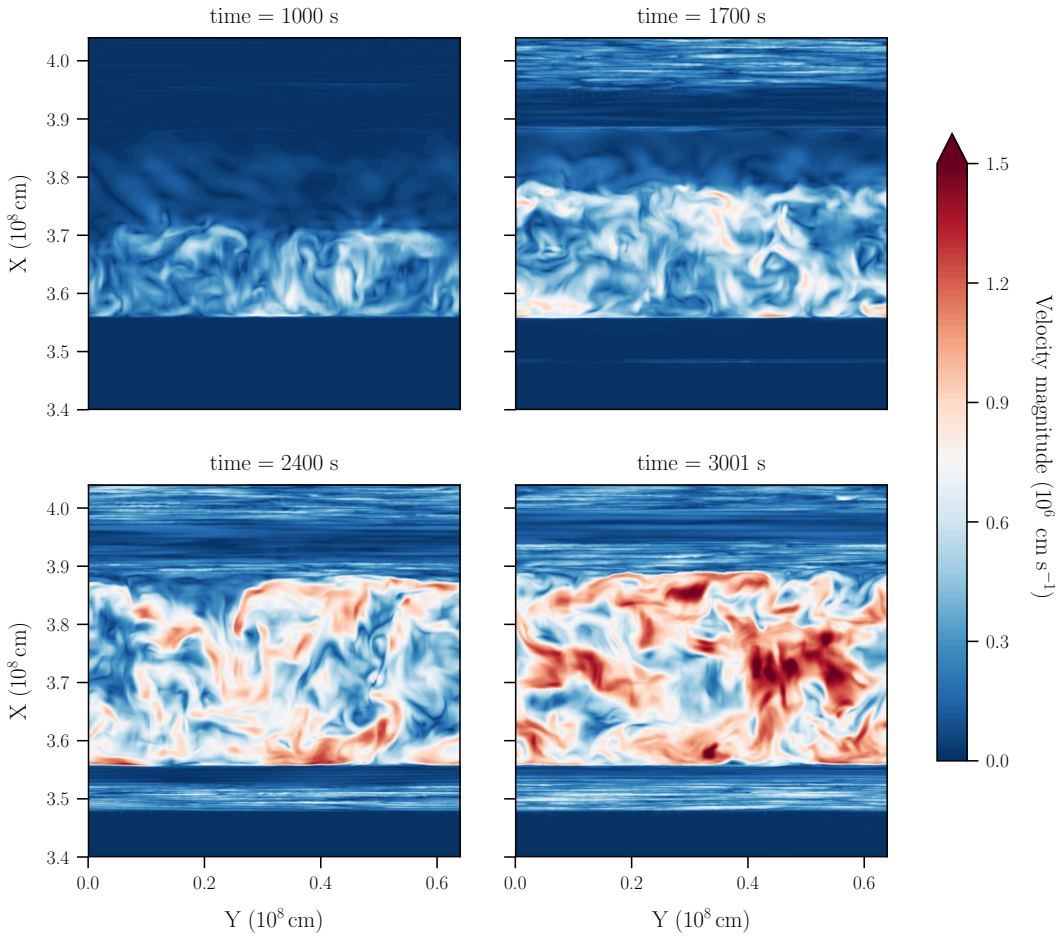

Figure 4.5: Vertical cross-sections taken from `Ex1_512` at 1000, 1700, 2400 and 3001 seconds, with the fluid speed in colour scale. The progression shows the formation of the convective cell and its growth as expected from turbulent entrainment, with an increase in the velocity magnitude of the fluid elements.

resolution on the fluid motions, producing eddies and plumes progressively on smaller scales as the resolution increases. According to the ILES framework (see Sec. 3.3), the dissipative scale corresponds here to the grid scale, having numerical dissipation that mimics the effect of viscosity; therefore, simulations with higher resolution have smaller dissipation scales and display more detailed convective features, but since the dissipation rate is independent of the scale, the physics of convection is expected to be the same regardless of the resolution.

Finally, I compare in Figure 4.7 the cross-sections of the four models `Ex1_512`, `Ex10_512`, `Ex100_512`, `Ex1000_512` when they all have a similar convective shell size, to present the effects of the energy boosting in a different way. The time frames of the simulations have been chosen at the moment when their upper convective boundaries have all reached $r \sim 3.9 \times 10^8$ cm. This figure clearly shows how a larger boosting factor is linked to higher kinetic energies of the fluid, as expected.

As a different way of studying the time evolution of the simulations, I present in Fig. 4.8 the specific total kinetic energy, integrated across the simulation domain, evolving over time for the four simulations with same resolution and different boosting `Ex1_512`, `Ex10_512`, `Ex100_512`, `Ex1000_512`. In all simulations, the first part of the plot is dominated by a sudden increase in kinetic energy, which corresponds to the initial transient when turbulent convection is building up inside the region predicted to be convective. The duration of this transient depends on the convective velocities, therefore on the boosting factor: this is why it is considerably longer for the nominal-luminosity model. Afterwards, the simulations are in the quasi-steady state, during which the kinetic energy slowly increases over time. This phase is dominated by the visible pulses in kinetic energy with a period equal to the convective turnover time (see Table 4.1 for values). These oscillations come from the time delay between the formation of large-scale plumes at the bottom of the convective zone and their rise and dissipation towards the top. It is worth mentioning

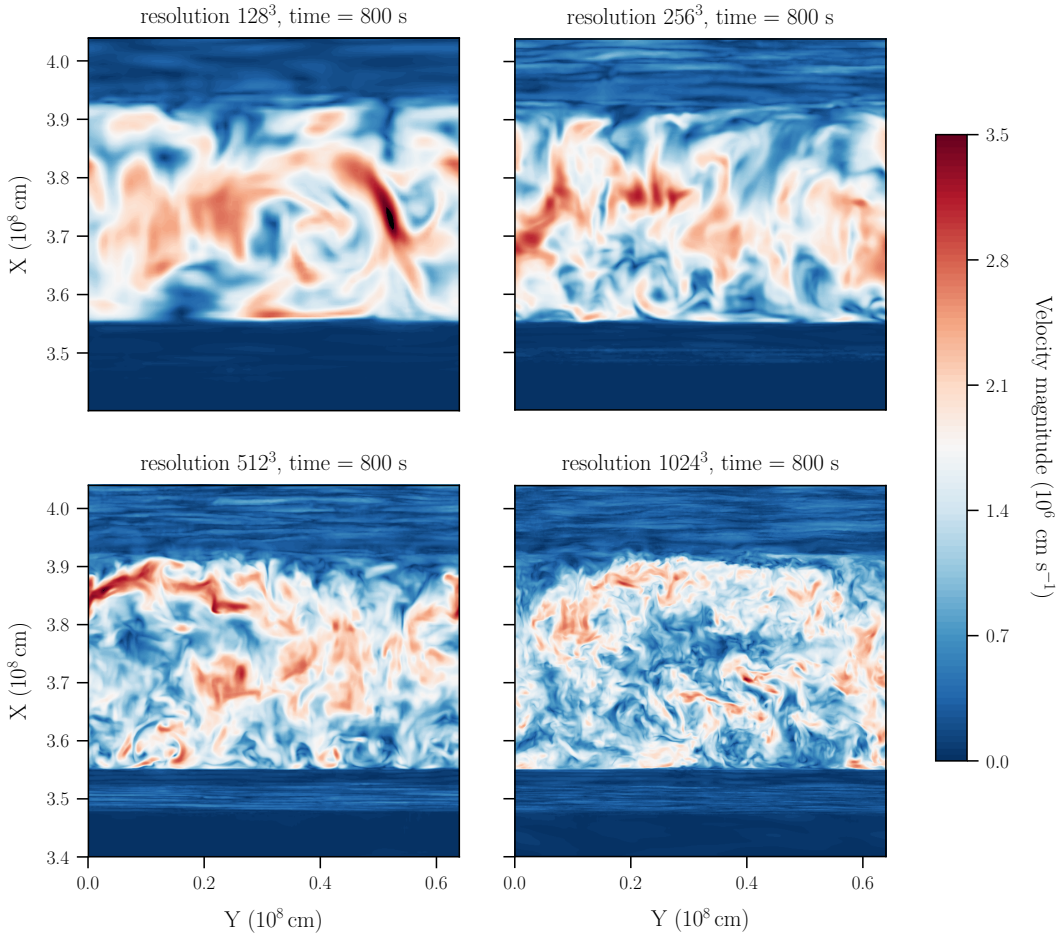

Figure 4.6: Same as Fig. 4.5, but for the models with different resolution `Ex10_128`, `Ex10_256`, `Ex10_512`, `Ex10_1025`, taken at 800 seconds from the beginning of each simulation. Since a higher resolution is linked to a smaller dissipation scale, the simulations produce eddies on a smaller scale when the resolution is increased.

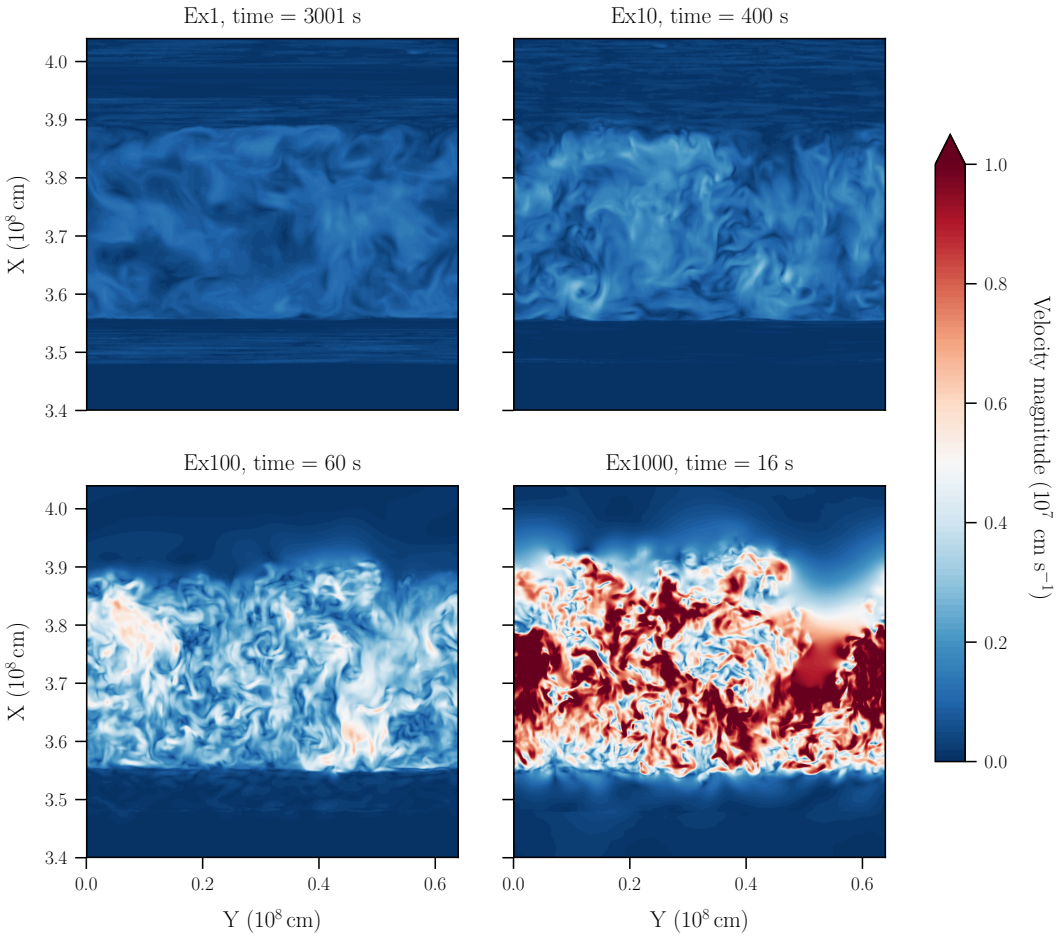

Figure 4.7: Same as Fig. 4.5, but for the models with different boosting factors `Ex1_512`, `Ex10_512`, `Ex100_512`, `Ex1000_512`, taken at 3001, 400, 60, 16 seconds respectively, chosen so that the convective boundary locations are similar in all simulations. One major effect of the boosting is an increase in the velocity magnitude of the fluid elements.

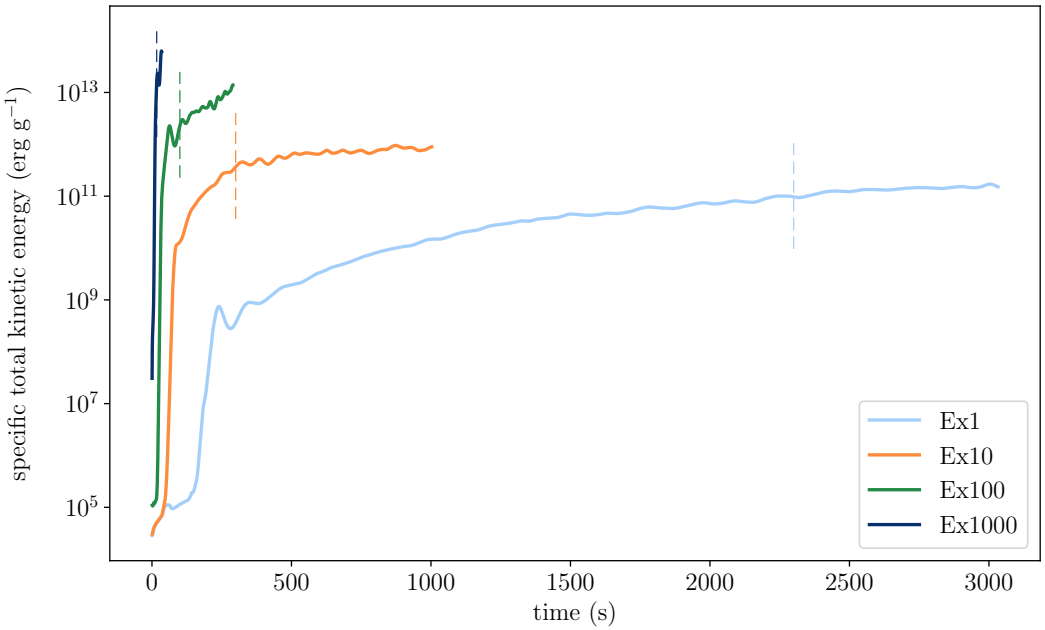

Figure 4.8: Time evolution of the specific kinetic energy for `Ex1_512`, `Ex10_512`, `Ex100_512`, `Ex1000_512`. After an initial transient, the simulations enter the quasi-steady state (starting time indicated by the vertical dashed lines). Models with larger boosting factors have shorter time-scales, and reach higher kinetic energies.

here that the magnitude of the kinetic energy scales with the luminosity according to a simple relation: having established that $v_{\rm rms} \propto \varepsilon^{1/3}$ (Biermann, 1932), it follows that the kinetic energy is proportional to $\varepsilon^{2/3}$. The convective velocity from Table 4.1 follows the expected scaling, and apart from statistical fluctuations the kinetic energy from Fig. 4.8 does the same.

Similarly, I show in Fig. 4.9 the time evolution of the kinetic energy for four simulations with different resolution but same boosting factor: `Ex10_128`, `Ex10_256`, `Ex10_512`, `Ex10_1024`. In this case, the evolution is the same for all simulations because of the similar values of $v_{\rm rms}$ and $\tau_{\rm c}$ in models with the same boosting factor, regardless of the resolution (see Table 4.1).

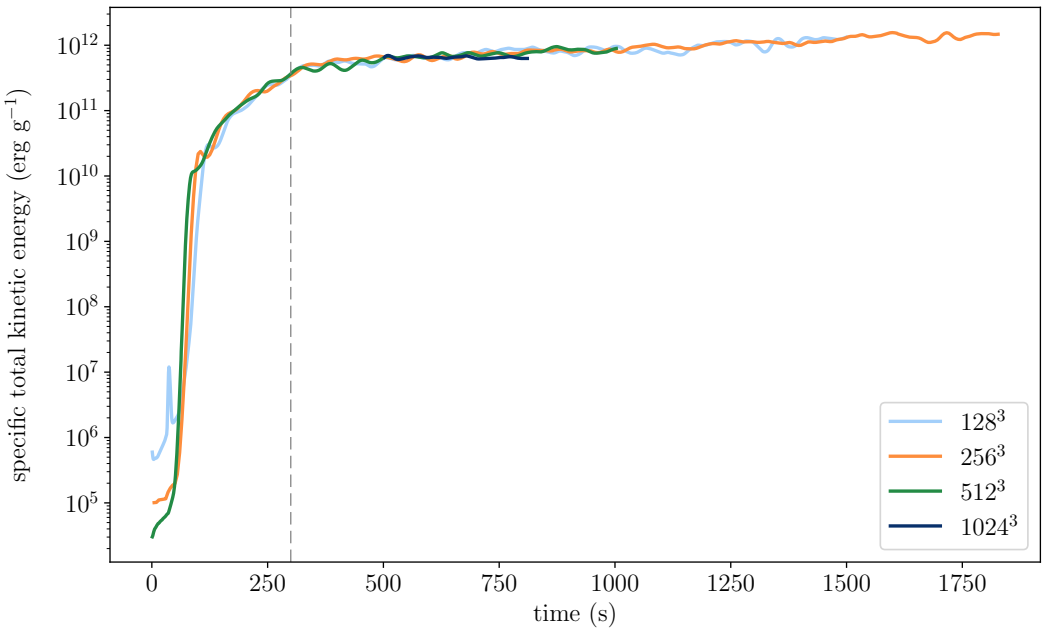

Figure 4.9: Same as Fig. 4.8, but for models with same boosting factor and different resolution `Ex10_128`, `Ex10_256`, `Ex10_512`, `Ex10_1024`. The simulations share a very similar evolution. The vertical dashed line shows the beginning of the quasi-steady state.

4.3.1 Spectral analysis of the kinetic energy

A different way of studying the kinetic energy distribution and evolution in the 3D simulations is to perform a spectral analysis. Since the present set of simulations has been produced assuming a Cartesian geometry and the plane-parallel approximation, I performed here a horizontal 2D Fourier analysis of the velocities in the simulations, following a similar approach to e.g. Cristini et al. (2019) and Andrassy et al. (2022). Having fixed the radius x inside the convective zone, a discrete Fourier transform of a quantity q as a function of the horizontal coordinates y, z is defined as:

$$\hat{q}(k_y, k_z) = \frac{1}{N_y N_z} \sum_{n_y=0}^{N_y-1} \sum_{n_z=0}^{N_z-1} q(y,z)\, \mathrm{e}^{-i\,2\pi\left(\frac{k_y n_y}{N_y}+\frac{k_z n_z}{N_z}\right)} \tag{4.5}$$

where N_y, N_z are the numerical resolution, n_y, n_z the cell numbers, and k_y, k_z the wavenumbers, which span the range:

$$\begin{aligned} k_y &= \begin{cases} i, & \text{if} \quad 0 \le i < N_y/2 \\ i - N_y, & \text{if} \quad N_y/2 \le i < N_y \end{cases} \\ k_z &= \begin{cases} j, & \text{if} \quad 0 \le j < N_z/2 \\ j - N_z, & \text{if} \quad N_z/2 \le j < N_z \end{cases} \end{aligned} \tag{4.6}$$

To visualize this process, one can imagine the transform $\hat{q}$ as a function of the reciprocal space $\vec{k} = (k_y, k_z)$ with $k_y \in [-N_y/2, N_y/2]$ and $k_z \in [-N_z/2, N_z/2]$. Therefore, the norm $k = \sqrt{k_y^2 + k_z^2}$ draws a circle in the (k_y, k_z) space, so we need to be careful and limit our spectra to the range $k \in [0, \min\{N_y/2, N_z/2\}]$ to avoid the circle going beyond the domain and losing a fraction of the signal, resulting in a drop of the power spectrum.

In the spectra I present here, I plot the squared Fourier transform of the velocity, which can be interpreted as a specific kinetic energy, as a function of both the wavenumber k and the real space r. I also normalise the spectra by the power law expected for the inertial scaling $k^{-5/3}$ (Kolmogorov, 1941): in this way, the scales where the spectra have a horizontal trend correspond to the

inertial range. In Fig. 4.10, I compare the spectra of the radial velocity in models with different resolution (top panel) and different boosting factors (bottom panel). These spectra are averaged over the entire quasi-steady state for each simulation, and have been taken in the bulk of the convective region. We can see from the upper plot that increasing the resolution the inertial plateaus are extended towards larger k, because dissipation occurs at smaller scales r, as expected from the ILES method. On the other hand, increasing only the luminosity as in the lower plot results in an increase of the kinetic energy without changing the length of the plateaus, since the convective velocities are higher but the dissipation scale remains the same.

To study the time evolution of the spectra, I plot in Fig. 4.11 the different velocity components taken at different times from the beginning to the end of the `Ex10_512` simulation, averaged over windows of 50 s, which is approximately the convective turnover time. The spectra were taken at $r = 3.6 \times 10^8$ cm, and the figure shows the square of the radial velocity (top panel) and of the horizontal velocity (bottom panel). At the very beginning of the simulation, during the initial transient, the spectra present a peak at large k, i.e. at small scales, because convection is dominated by small eddies at this early stage. As time passes, the velocity magnitude increases and the peaks move towards smaller k, as the turbulent flow forms large-scale structures that contain most of the energy. During the quasi-steady state, the spectra converge and remain relatively constant over time.

Additionally, I compare in Fig. 4.12 the velocity spectra taken at different radial locations inside the convective zone, from 3.58 to 3.88×10^8 cm, during the quasi-steady state of `Ex10_512`, averaged over 500 - 550 s. The spectra present very little difference, confirming that turbulence remains generally isotropic throughout the convective zone. The major difference is in the radial velocity close to the convective boundaries, at the uppermost and lowermost radii, whose spectra show a lower radial velocity around $k = 10$ compared to the spectra in the bulk of the convective region. This can be easily explained con-

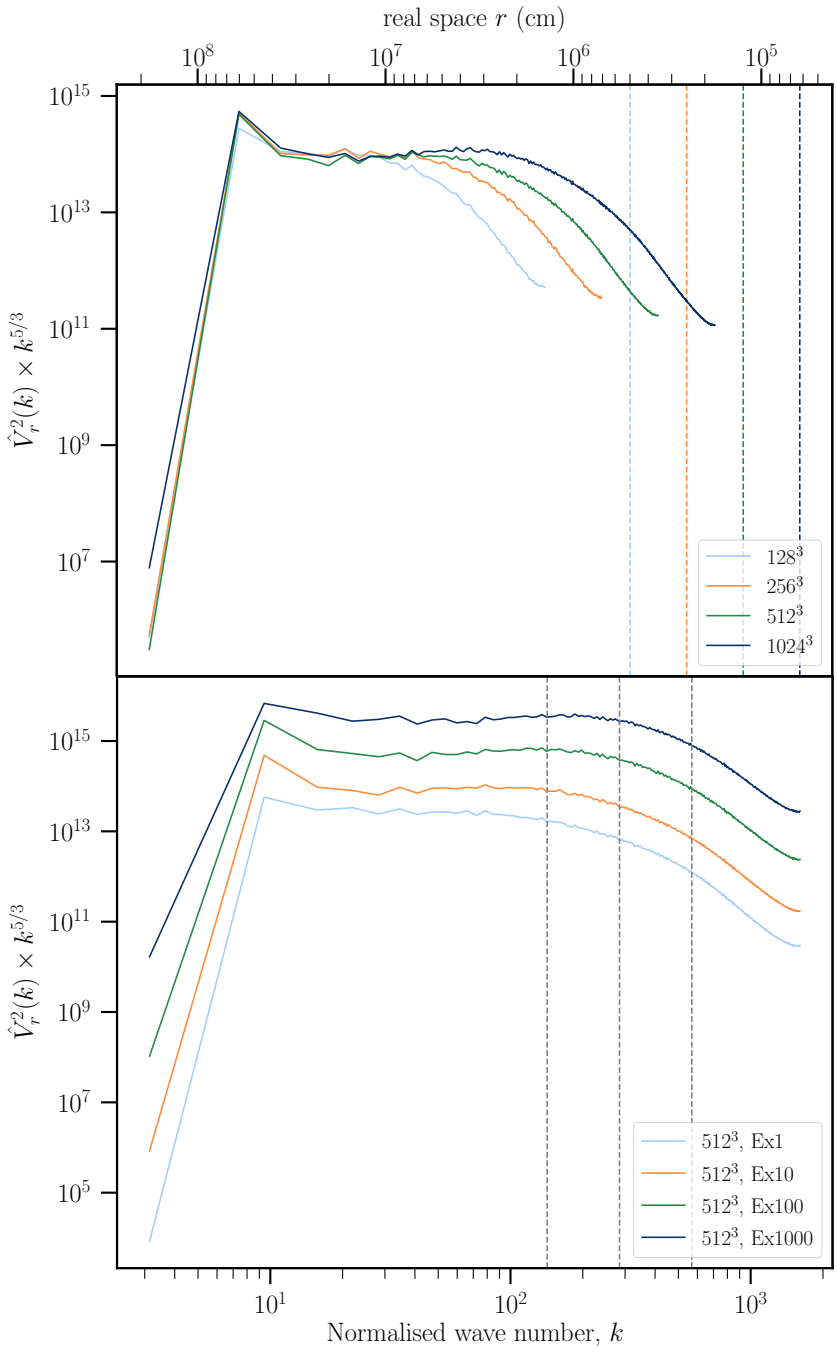

Figure 4.10: Fourier transforms of the radial velocity, squared and multiplied by $k^{5/3}$, for models with different resolution `Ex10_128`, `Ex10_256`, `Ex10_512`, `Ex10_1024` (top panel), and with different boosting factors `Ex1_512`, `Ex10_512`, `Ex100_512`, `Ex1000_512` (bottom panel). The vertical dashed lines show in the upper plot the dissipation range for each resolution, and in the lower plot 32, 16, 8 times the dissipation range for resolution 512^3.

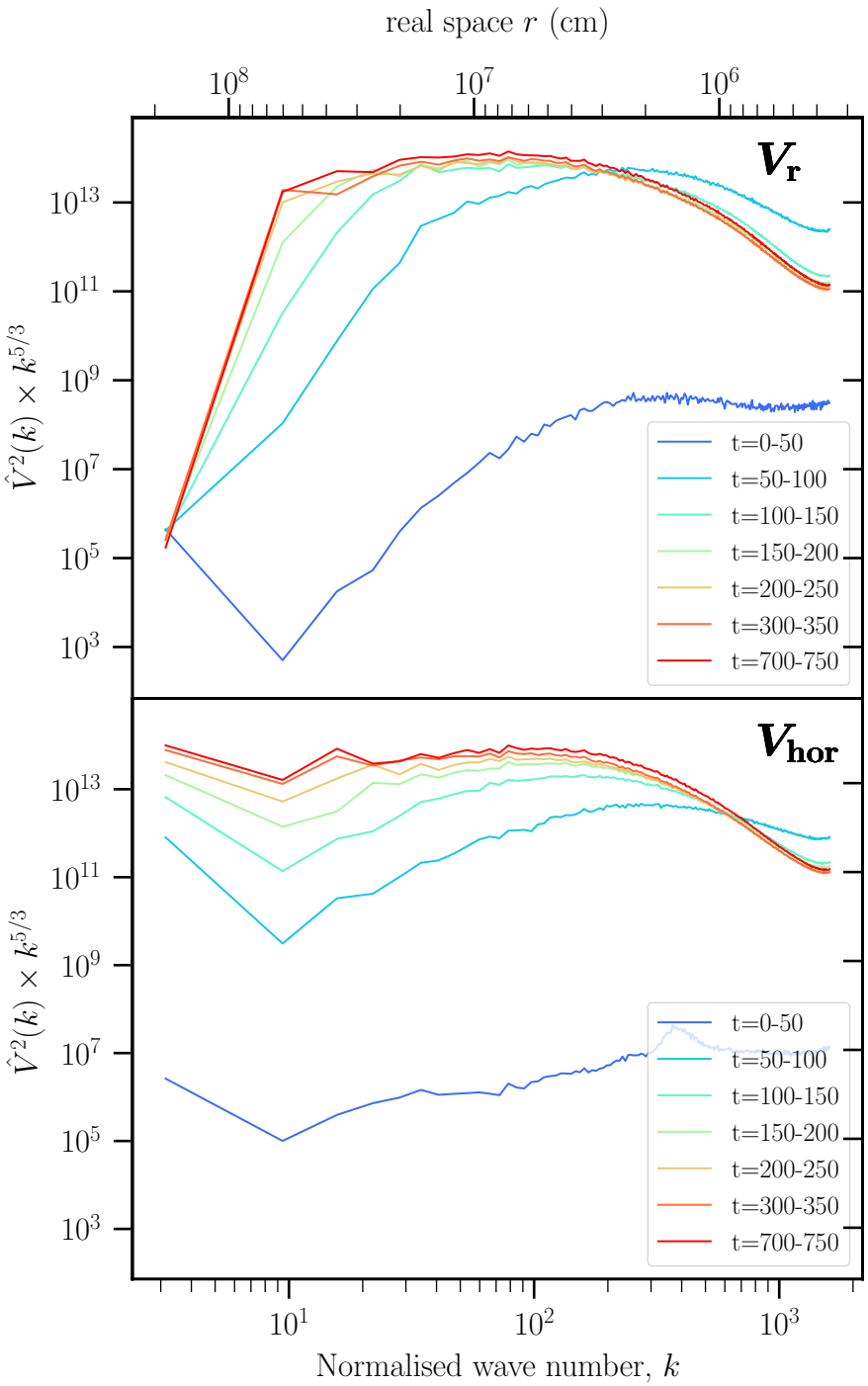

Figure 4.11: Same as Fig. 4.10, but for the Fourier transforms of the radial velocity (top panel) and horizontal velocity (bottom panel), taken at different times through the `Ex10_512` simulation, with the averaging windows listed in the legend. The convergence of the spectra towards the quasi-steady state can be clearly seen.

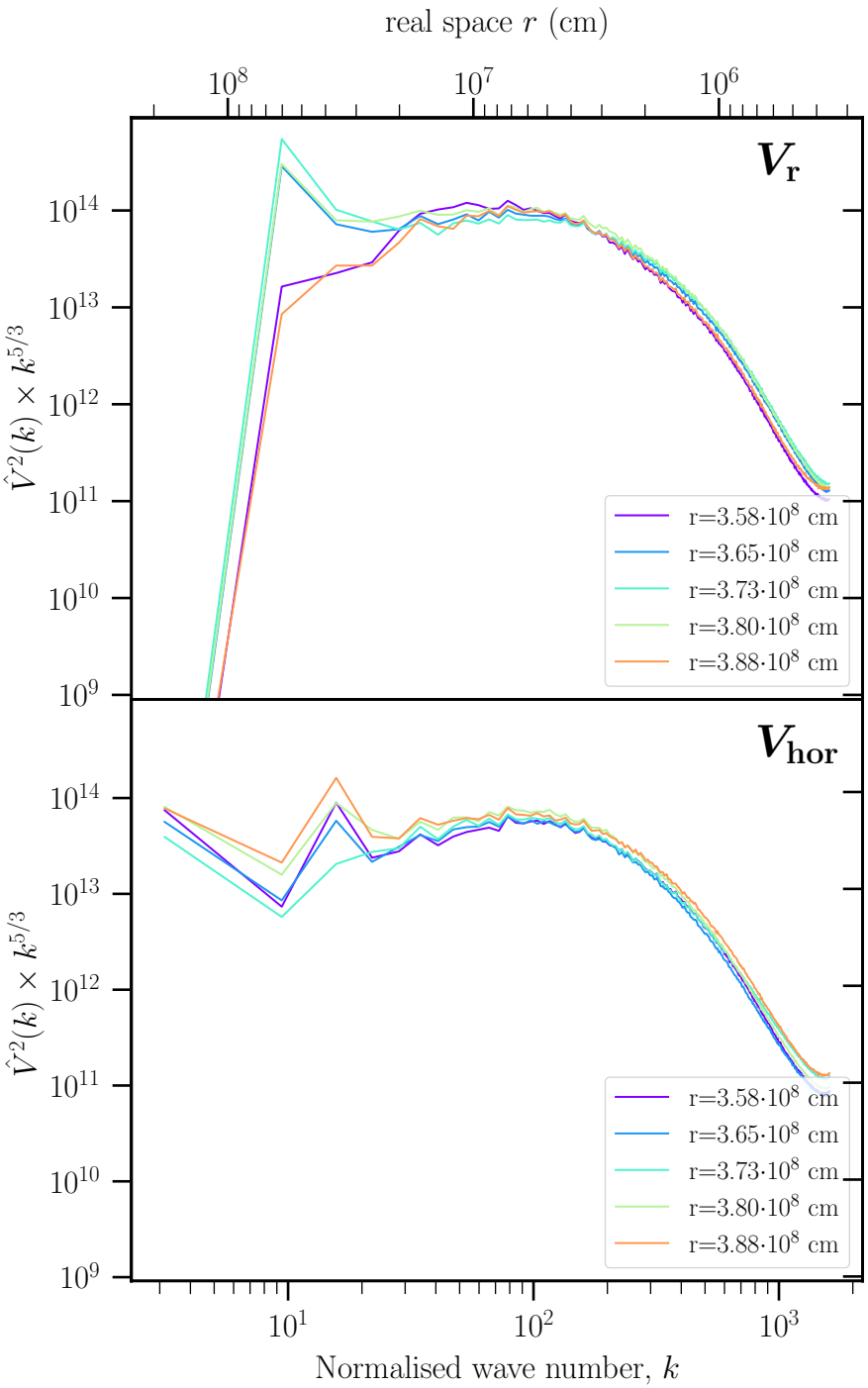

Figure 4.12: Same as Fig. 4.10, but for the Fourier transforms of the radial velocity (top panel) and horizontal velocity (bottom panel), taken at different radial locations inside the convective zone, listed in the legend, from `Ex10_512` averaged over 500 - 550 seconds.

sidering that the convective boundaries limit the motion of the fluid elements in the radial direction, while they are still free and encouraged to move in the horizontal direction; indeed, the spectra of the horizontal velocity do not show such a strong difference.

4.4 Chemical composition and nucleosynthesis

In addition to studying the dynamics of the simulations, it is also worth investigating the changes in the chemical composition, making use of the explicit burning routine included in `PROMPI`. The key species involved in neon burning are ^{16}O, ^{20}Ne, ^{24}Mg and ^{28}Si. It is useful to plot the abundances of these species in cross-sections of the simulations, as I do in Fig. 4.13 where I show the mass fractions in colour scale after 1500 s from the beginning of the `Ex1_512` simulation. The situation here fully reflects what is expected from a neon-burning environment: compared to the mean abundance in the shell (in white for each isotope), neon is consumed inside the convective region, so its mass fraction goes towards the blue, while oxygen, magnesium and silicon are produced, so they are more red-coloured. These cross-sections also show very clearly how the different species are mixed inside the convective zone, being transported by the turbulent motions of the fluid.

Although cross-sections are impactful ways of visualizing the simulations, they are impractical for a rigorous analysis of the results. To study the chemical composition, it is better to use horizontally averaged profiles of the mass fractions, assuming that the chemicals are horizontally well mixed and non-radial fluctuations are small, as is often the case. As an example, I present in Fig. 4.14 the radial profiles of ^{16}O, ^{20}Ne, ^{24}Mg and ^{28}Si at the beginning (dashed) and at the end (solid) of the `Ex10_512` simulation; thus, the dashed lines indicate the composition of the 1D input model. We can see that above the convec-

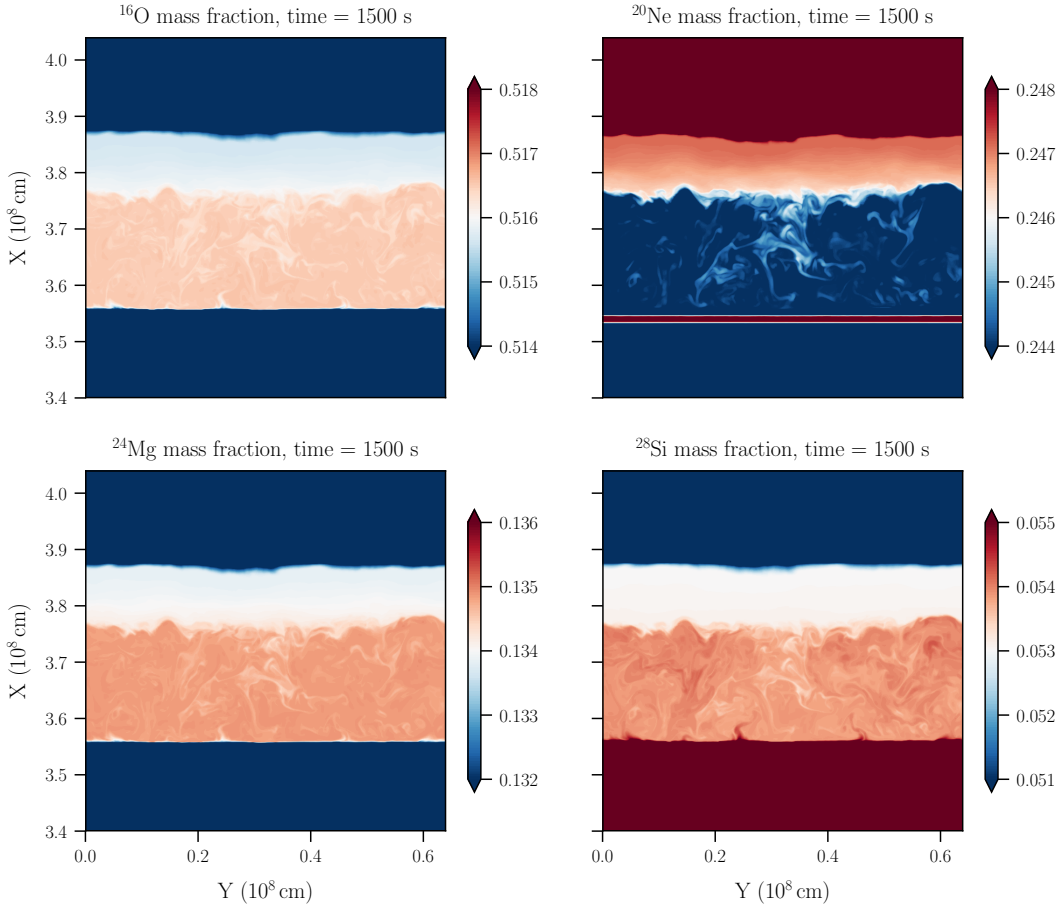

Figure 4.13: Vertical cross-sections from `Ex1_512` at 1500 seconds, with the mass fraction for the nuclides ^{16}O, ^{20}Ne, ^{24}Mg, ^{28}Si in colour scale. Inside the convective zone, the overabundance of ^{16}O, ^{24}Mg, ^{28}Si and the underabundance of ^{20}Ne reflect the nuclear reactions of the neon burning.

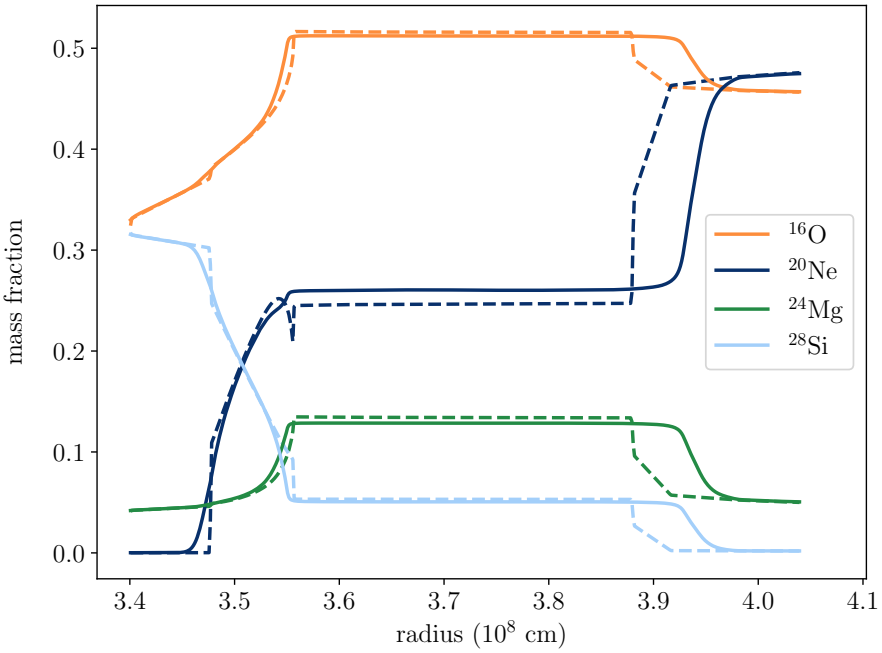

Figure 4.14: Radial profiles of the horizontally averaged mass fractions of ^{16}O, ^{20}Ne, ^{24}Mg, ^{28}Si at the beginning (dashed) and at the end (solid) of the `Ex10_512` simulation.

tive region, at $r > 3.88 \times 10^8$ cm, the composition is consisting mostly of oxygen and neon as a result of the previous helium burning in this region (see Fig. 4.1), that produced mostly ^{12}C and ^{16}O, and the following carbon burning that converted ^{12}C into ^{20}Ne, according to the nuclear reactions that I described in Sec. 3.4.5. Inside the convective zone, where $3.56 < r < 3.88 \times 10^8$ cm, the composition profiles are plateauing because of convective mixing, and the neon-burning reactions are taking place as described before, consuming neon to produce oxygen and magnesium, which are more abundant in the convective zone compared to the external layers. Below the convective zone $r < 3.56 \times 10^8$ cm, radiative burning has taken place and has converted oxygen, neon and magnesium into heavier nuclides such as silicon and sulphur.
Towards the end of the simulation, Fig. 4.14 shows that the upper boundary has moved outwards, due to the entrainment of material from the upper stable region; a similar effect, but weaker, is also present at the bottom of the convective zone, causing the slight downward shifting of the lower convective boundary. Inside the convective zone, the abundance of ^{20}Ne has increased despite the nuclear burning reactions, because of the entrainment of neon-rich material from above, while ^{16}O, ^{24}Mg and ^{28}Si have slightly decreased due to the mixing with material that is poor in these elements. This is an important result, and it shows that for this environment the hydrodynamic simulations predict that the impact of entrainment is much stronger than the effects of the nuclear burning.

4.5 Convective boundary mixing

To study the effects of entrainment on the evolutions of the neon-shell simulations, we first need to have a solid method that allows us to track the location of the convective boundaries. This is not a trivial problem: in 1D models, conditions like the Schwartschild criterion can be applied, making use of vari-

ables that depend only on the radius and are often step-like; but in multi-D simulations, variables usually have a smooth transition between layers, and the boundaries assume the form of extended surfaces that can be deformed and fluctuate. Normally, it is possible to define the convective boundary using either the thermodynamic variables or the chemical composition of the layers. I make use here of the latter, in consistency with previous works such as Cristini et al. (2017, 2019).

In Fig. 4.15, the mean atomic mass $\bar{A}$ is shown from the 1D initial model. As in the case of the mass fraction profiles, the central plateau corresponds to a well-mixed region, which is the convective zone, while the upper plateau is a stable region above the convective one. In the model of Cristini et al. (2017), a lower plateau was also present, so they defined the convective boundary locations as the mid-points between the convective and the radiative plateaus; however, a lower plateau is missing in our case. Therefore, I decided here to define the radial location of the upper convective boundary as where $\bar{A}$ is intermediate between the value in the convective and in the upper stable regions; as for the lower convective boundary, I use the same jump in $\bar{A}$ between the convective and upper stable regions, and I define the boundary as where $\bar{A}$ is equal to the value in the convective zone plus half the jump. Summarizing:

$$\begin{aligned} r_{\text{upper boundary}} &= r\left(\bar{A} = \frac{\bar{A}_{\text{convective}} + \bar{A}_{\text{upper radiative}}}{2}\right) \\ r_{\text{lower boundary}} &= r\left(\bar{A} = \bar{A}_{\text{convective}} + \frac{\bar{A}_{\text{convective}} - \bar{A}_{\text{upper radiative}}}{2}\right) \end{aligned} \tag{4.7}$$

The convective boundaries obtained with these definitions are shown in Fig. 4.15 as vertical dashed lines.

To give a preliminary idea of how the convective boundaries are expected to evolve over time, I display in Fig. 4.16 the time evolution of the horizontally averaged mean atomic mass for `Ex10_512`. Just like in Fig. 4.15, the value of $\bar{A}$, here in colour scale, gives a clear indication of the different layers that compose the simulation: the convective zone, which is the part in yellow, can

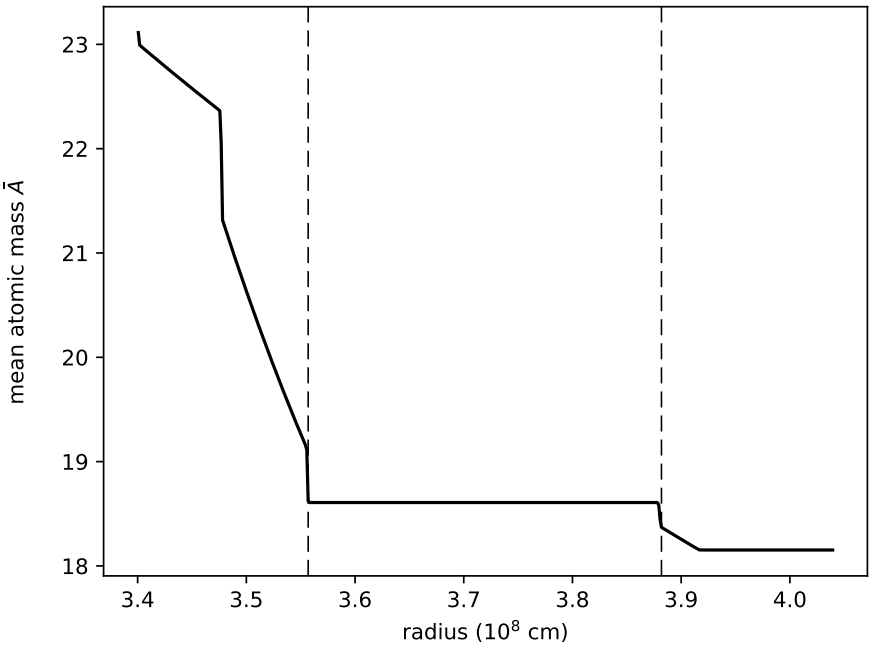

Figure 4.15: Radial profile of the mean atomic mass at the beginning of the simulations, taken from the 1D input model as initial conditions. The vertical dashed lines are the convective boundary locations computed as described in this section.

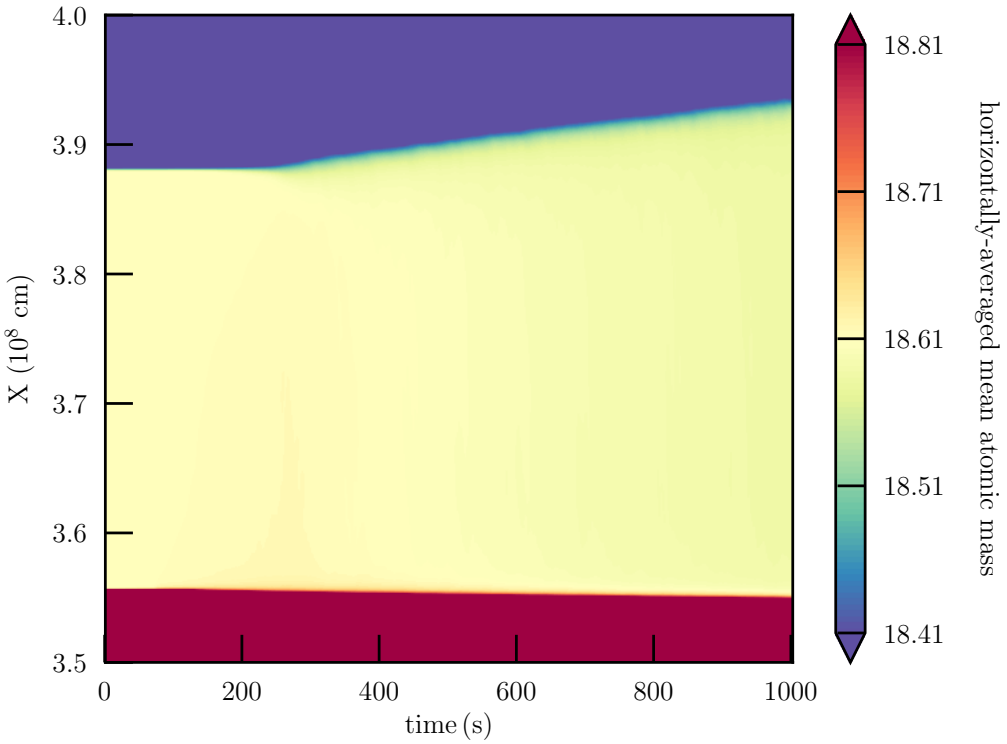

Figure 4.16: Time evolution of the horizontally averaged mean atomic mass (in colour scale) for the `Ex10_512` simulation. After an initial transient of about 250 s, the convective zone (in yellow) grows due to entrainment.

be clearly distinguished from the upper and lower stable regions, which have lower and higher values of $\bar{A}$ respectively. Furthermore, the plot shows that after an initial transient of ~ 250 s the convective zone starts growing both upwards and downwards under the effect of entrainment of material from the upper and lower stable regions. This shows that entrainment is present and strong in the hydrodynamic simulations, and it can be studied making use of the changes in chemical composition.

Using the findings and definitions introduced above, we can finally study the evolution of the convective boundaries in a rigorous way. The plots in Fig. 4.17 show the time evolution of the upper and lower boundary locations enclosing the convective zone, for the four high-resolution models with different boosting factors. It is evident the strong impact of the energy boosting on the growth of the convective zone: a larger boosting factor promotes the convective boundary mixing, so the entrainment rate is progressively larger. The models with a large boosting also show very clearly the downward migration of the lower boundary: entrainment actually takes place at both boundaries, but it is much weaker at the lower one, so it is more difficult to observe in simulations with small boosting.

The figure also shows another interesting aspect of the simulations. Studying entrainment in models that include energy boosting can present some difficulties: on the one hand, simulations with no boosting evolve extremely slowly, and are computationally very expensive; on the other hand, when the boosting is excessive the boundary migration is not smooth and can rapidly reach the domains of the simulation, affecting the accuracy of the results. These effects are clearly illustrated by Fig. 4.17. For these reasons, a more effective way of studying entrainment is to collect information from simulations with different levels of boosting, and include it into a more generally applicable law. We shall see how this is performed for the present set of simulations in the following section.

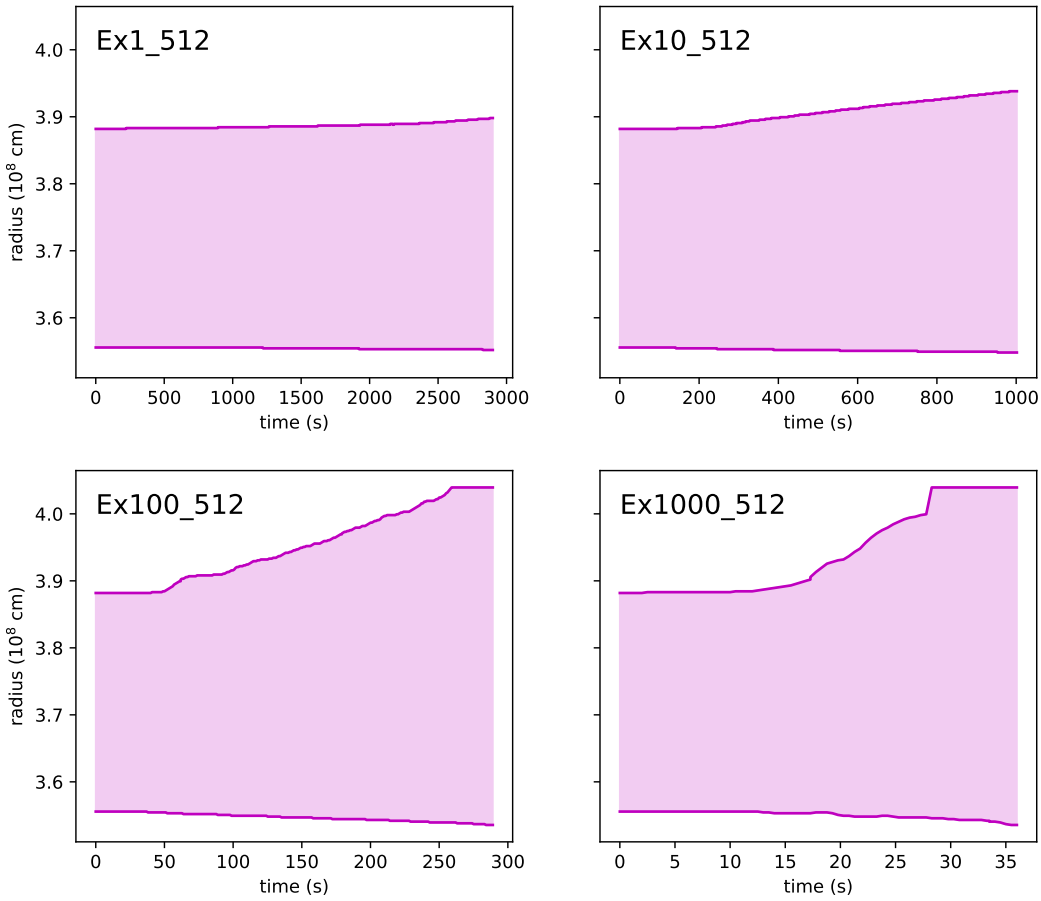

Figure 4.17: Time evolution of the upper and lower convective boundaries, enclosing the growing convective zone (in magenta), for the four models `Ex1_512`, `Ex10_512`, `Ex100_512`, `Ex1000_512`. The impact of the boosting factor on the evolution of the convective regions can be clearly seen.

4.5.1 Computing the entrainment law

I have described in Sec. 2.2.2 how entrainment can be parametrized with a simple and general law (2.25), making use of the definitions in (2.26). I briefly recall here that the quantities needed for performing the parametrization are the entrainment velocity $v_{\rm e}$, the convective velocity $v_{\rm rms}$, and the bulk Richardson number $\mathrm{Ri_B}$, which is computed from the Brunt-Väisälä frequency N defined in (2.15). In this section, I analyse the set of simulations with high resolution 512^3 and different boosting factors, that allow to resolve the boundaries in detail and have been run for multiple convective turnovers. The simulation `Ex1000_512` has been excluded from the entrainment analysis, due to its excessive boosting that distorts the shape of the boundaries and makes it difficult to follow the convective boundary evolution.

The values of the entrainment rates and bulk Richardson numbers estimated from the simulations are listed in Table 4.2. The entrainment velocities have been obtained from the time derivatives of the boundary locations from Fig. 4.17; $\mathrm{Ri_B}$ was calculated from the definitions in (2.15) and (2.26). All data have been averaged over the entire quasi-steady state for each simulation. In particular, since there is no strict definition for ℓ in (2.26), here I set it equal to a fraction of the local pressure scale hight, as done in Cristini et al. (2019), who set $\ell = H_{\rm P}/2$. However, for the present simulations this range would be almost as large as the entire convective region, because the radial domain is ~ 30 times smaller than in Cristini et al. (2019); therefore, I set here $\ell = H_{\rm P}/12$ so that it can include just the convective boundaries. Despite this being a hand-tuned choice, it is not expected to impact the value of $\mathrm{Ri_B}$, because the integrated quantity, N^2, presents a narrow peak around the boundary, and it is close to zero elsewhere: as long as ℓ includes the peak entirely, integrating additional regions brings negligible contribution to $\mathrm{Ri_B}$.

It is worth here discussing the sensitivity of the entrainment rate measurements to other choices. First, the resolution of the simulation can potentially

Table 4.2: List of measurements for the entrainment analysis from the 3D hydrodynamic simulations: model name; upper-boundary entrainment velocity v_e^{up}; lower-boundary entrainment velocity v_e^{low}; upper-boundary bulk Richardson number Ri_B^{up}; lower-boundary bulk Richardson number Ri_B^{low}.

name	v_e^{up} (cm s^{-1})	v_e^{low} (cm s^{-1})	Ri_B^{up}	Ri_B^{low}
Ex1_512	1.36×10^3	1.17×10^2	493	2214
Ex10_512	6.97×10^3	6.16×10^2	104	492
Ex100_512	7.56×10^4	5.63×10^3	19	103

affect the boundary migration, primarily because the boundary location may not be well resolved; I have confirmed that for resolution 256^3 and above the boundary migration is smooth (see Fig. 4.17) and produces similar entrainment rates for the same luminosity, regardless of the resolution. Second, the entrainment rate might depend on the time window chosen for measuring the boundary migration. From Fig. 4.17, we can see that entrainment behaves linearly during the quasi-steady state, after the initial transient and before reaching the upper domain. As long as the time averaging falls within this window, the entrainment rate is constant. I decided to use for each simulation the entire quasi-steady state as averaging window, in order to limit the statistical fluctuations that affect the small time-scales.

From Table 4.2, we can see that simulations with a larger boosting factor produce larger entrainment velocities and smaller Ri_B, due to the larger penetrability of the boundaries. Making use of these measurements, I can finally parametrize entrainment by estimating the free parameters A, n that define the entrainment law (2.25). I perform here a liner regression in log scale on the data from both the upper and lower convective boundaries, treating them as independent measurements of entrainment in different conditions. In order to put these results into context, I show in Fig. 4.18 the data and the line of best fit in log scale for the present neon-shell simulations (blue, solid), alongside

previous PROMPI simulations of a carbon shell (green, dashed, Cristini et al., 2019) and an oxygen shell (orange, dot-dashed, Meakin & Arnett, 2007), intending this figure as an update of Fig. 2.1. In the plot, I also include the error bars for the neon-shell measurements corresponding to the standard deviations of the bulk Richardson number and the entrainment rate at each time-step in the simulations.

The estimates for the entrainment law parameters from this new study are $\log A = -0.53 \pm 0.47$ and $n = 0.96 \pm 0.19$; these values fall in between the ones obtained for the carbon shell and the oxygen shell. Comparing the parameter estimates from different burning stages can help determine whether or not the entrainment law varies during the stellar evolution; in this case, Fig. 4.18 shows that entrainment seems to occur in a similar way across the different burning stages of massive stars.

The best fit for n in the neon-shell simulations is compatible with the value of 1 expected from geophysical studies (Fernando, 1991). The estimate for A is more uncertain, since the fitting has been done in log scale and the measurements have a large dispersion: the new results indicate a value between $A \sim 0.1$ and 1, which is in line with the other hydrodynamic simulations of entrainment (Gilet et al., 2013; Müller et al., 2016; Horst et al., 2021). Differently, 1D stellar model studies of entrainment (Staritsin, 2013; Scott et al., 2021) find much smaller values close to $A \sim 10^{-4}$, as I explained in Sec. 2.2.2, having fixed $n = 1$ and calibrating A through asteroseismic measurements (Staritsin, 2013) or the observed main sequence width (Scott et al., 2021). However, these results have been obtained for convective cores of main-sequence stars, but 1D stellar models have never investigated entrainment in late-phase convective zones, and they rarely include any CBM prescription for these late phases. This evidence strongly motivates further investigation of CBM and entrainment in 1D models of massive stars.

As one of the most important results of the present study, this new set of realistic hydrodynamic simulations of stellar convection establishes the presence

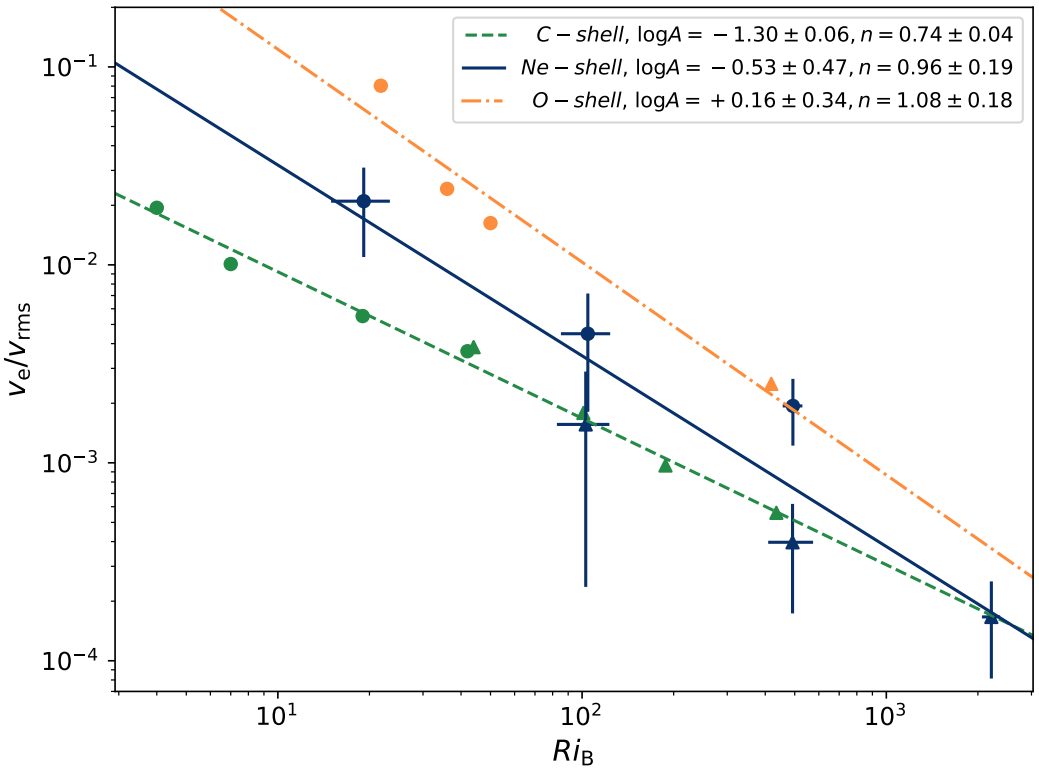

Figure 4.18: Entrainment rate versus bulk Richardson number in log scale, measurements from `PROMPI` simulations and respective linear regressions: Ne-shell from this study (in blue, solid), C-shell from Cristini et al. (2019) (in green, dashed), and O-shell from Meakin & Arnett (2007) (in orange, dot-dashed). Triangles are the lower convective boundaries, circles the upper boundaries. Error bars (only for Ne-shell) are standard deviations. Parameter estimates for the entrainment law $v_\mathrm{e}/v_\mathrm{rms} = A\ \mathrm{Ri}_\mathrm{B}^{-n}$ are listed in the legend for each study. Figure taken from Rizzuti et al. (2022).

of significant entrainment when using the exact conditions from a state-of-the-art 1D stellar model; therefore, we can conclude that strong turbulent entrainment is not a result of the large boosting factors normally used in hydrodynamic simulations, neither it comes from unusual initial conditions, but is a natural result that is expected to occur in real stars.

5 321D second-generation simulations of neon burning

5.1 Motivations and overview

As I explained in the previous chapters, making progress in understanding the evolution of stars is only possible employing both 1D and multi-D stellar models; despite their own limitations, each model complements the other with the ability of investigating aspects that are precluded to the other. 1D evolutionary models give a general but complete description of the entire stellar evolution, while multi-D models investigate localized problems with a high degree of detail and realism. The relation between the two is sometimes called "321D approach", referring to the fact that prescriptions about the stellar physics are obtained from 3D hydrodynamic simulations and integrated into 1D evolutionary models, in order to improve the predictions thanks to the refined physical assumptions.

This is not simply a linear approach, because 3D models are also based on initial conditions assumed from 1D models. We can imagine this as a cycle that connects 1D to 3D, in which each model is based on assumptions from the other, but it also produces results that can improve the other model. In Chapter 4, the 3D hydrodynamic simulations have been started from initial conditions assumed from a 1D model with no CBM prescription in the late phases, and the results were used to parametrize entrainment. The next logical step in the 321D approach is to produce new-generation 1D models that keep into account the strong CBM predicted by hydrodynamic simulations. And this can be pushed even further: results from 321D-guided 1D models can be fed into hydrodynamic simulations to test whether or not an equilibrium has been reached and predictions from 1D and 3D models are consistent. The major problem, as I described before, is that different studies can strongly

disagree on the amount of CBM to include in 1D stellar models, since hydrodynamic simulations always predict much larger entrainment rates than the ones assumed in 1D models.

In this chapter, I present the results from a new set of 3D hydrodynamic models simulating a neon-burning shell from a 20 $M_\odot$ star, started from a 321D-guided model that assumes stronger CBM prescriptions than usual. The results presented here have been published in Rizzuti et al. (2023). In particular, the 1D model assumed for initial conditions has been produced by collaborators, while I prepared, ran and analysed the hydrodynamic simulations. This work allowed me to compare the entrainment rates measured from the new 3D simulations to the ones assumed in 1D, which are normally much slower. Additionally, the simulations have been run for the entire nuclear burning time-scale until fuel is exhausted and convection dies out. Simulating an entire burning phase using hydrodynamic models is a complete novelty in the literature, and these results help answer some open questions in stellar physics, in particular whether convection stops when fuel is exhausted or if the mixing of entrained material extends the convective growth indefinitely. These are important points to clarify, because they determine the size of the convective zones, which can affect multiple aspects of the stellar life as I described in Sec. 2.2.

5.1.1 Setup of the simulations

Initial conditions have been assumed from a 1D stellar evolution model produced with the `MESA` code (Paxton et al., 2011, 2013, 2018, 2019), simulating the evolution of a 20 $M_\odot$ star at solar metallicity ($Z = 0.014$) using the relative abundances of Asplund et al. (2009). Mass-loss rates were taken from the so-called "Dutch" options, that include rates from Vink, de Koter & Lamers (2000, 2001) for O-type stars, from Nugis & Lamers (2000) if the star enters the Wolf-Rayet stage, i.e. when the surface hydrogen mass fraction drops below 0.4, and the empirical mass-loss rate from de Jager, Nieuwenhuijzen & van der

Hucht (1988) if the stellar effective temperature is $T_{\rm eff} < 10^4$ K. Convection in `MESA` is treated according to the mixing-length theory (see Sec. 2.1.1), having set $\alpha_{\rm MLT} = 1.67$ according to Arnett et al. (2018); in particular, the convective boundaries are determined through the Schwarzschild criterion (see Sec. 2.1). Convective boundary mixing was included according to the exponential decaying diffusive prescription I described in Sec. 2.2.1, assuming $f_{\rm ov} = 0.05$ for the upper boundaries of all convective cores and shells, and $f_{\rm ov} = 0.01$ for the lower boundaries of all convective shells.

Setting $f_{\rm ov} = 0.05$ for the upper convective boundaries implies a stronger CBM than normally assumed in stellar models, for example $\alpha_{\rm ov} = 0.1$ in Ekström et al. (2012) and $\alpha_{\rm ov} = 0.335$ in Brott et al. (2011), considering that $f_{\rm ov} \sim 1/10\ \alpha_{\rm ov}$ (see Scott et al., 2021). This large value is motivated by the work of Scott et al. (2021), who showed that $f_{\rm ov} \geq 0.05$ in stars ≥ 20 $M_\odot$ best reproduces the observed main-sequence width in the Hertzsprung-Russell diagram (Castro et al., 2014), as indicated by Scott et al. (2021) in their fig. 9. For the lower convective boundaries, setting $f_{\rm ov}$ to 1/5 of the value for the upper boundary is based on 3D hydrodynamic simulations (Cristini et al., 2019; Rizzuti et al., 2022), who found that CBM is weaker at the lower boundary due to its larger stiffness. Furthermore, Scott et al. (2021) show that the amount of CBM increases with the initial stellar mass, so choosing $f_{\rm ov} = 0.05$ for a 20 $M_\odot$ star is consistent with the smaller values inferred from asteroseismic measurements for less massive stars (see Bowman, 2020). In conclusion, including a strong CBM prescription in the 1D input model at all convective boundaries is supported by both observations and hydrodynamic simulations, and is a key aspect for the novelty of the results I present here.

Figure 5.1 shows the structure evolution diagram of the 1D input model, from the pre-main-sequence phase until core collapse. The convective zones are blue in colour, while the CBM zones are shown in green; we can see here the impact of CBM on the size of the convective zones. The 3D hydrodynamic simulations of this chapter have been started from the neon-burning shell indicated by the

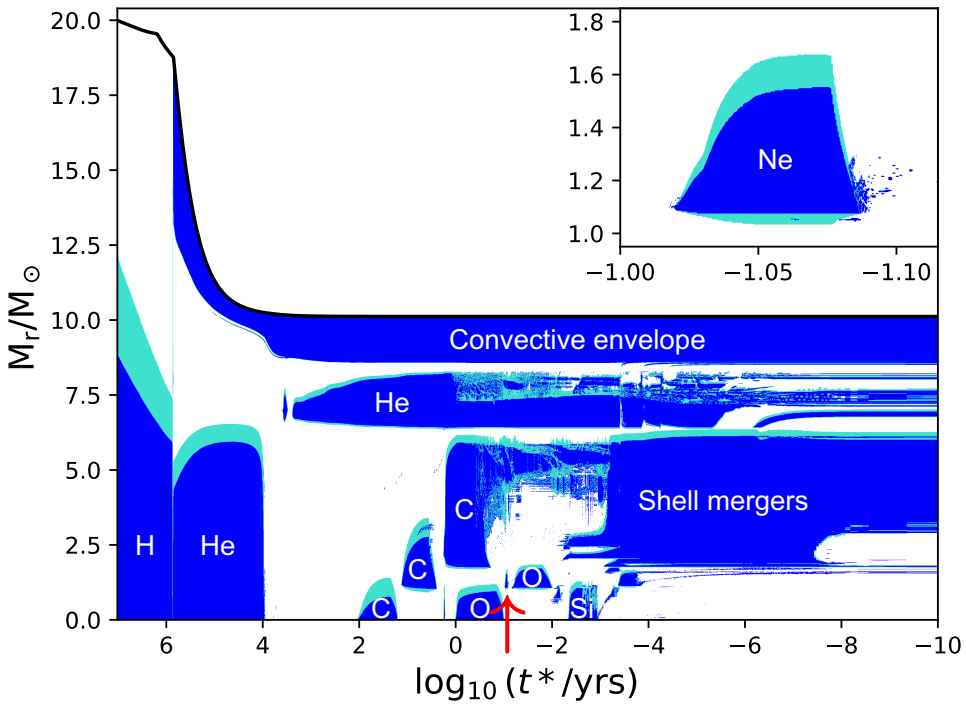

Figure 5.1: Structure evolution diagram of the 20 $M_\odot$ 1D `MESA` model as a function of the time left until the predicted collapse of the star (in years, log scale). In blue the convective zones, in green the CBM zones. The red arrow indicates the neon-burning shell the 3D simulations were started from, with a zoom-in in the top right corner. Figure taken from Rizzuti et al. (2023).

red arrow, a zoom-in of which is shown in the top right corner of Fig. 5.1 in mass coordinates, and also in Fig. 5.2 in radius coordinates. Additionally, Fig. 5.2 also shows the squared convective velocity in colour scale, the radial domain of the hydrodynamic simulations as a red line, and the isomass contours as black lines.

In the same way as it has been done in Chapter 4, the radial variables density, pressure, temperature, entropy, mass, and chemical composition have been remapped from the 1D to the 3D grid, adding small perturbations to density

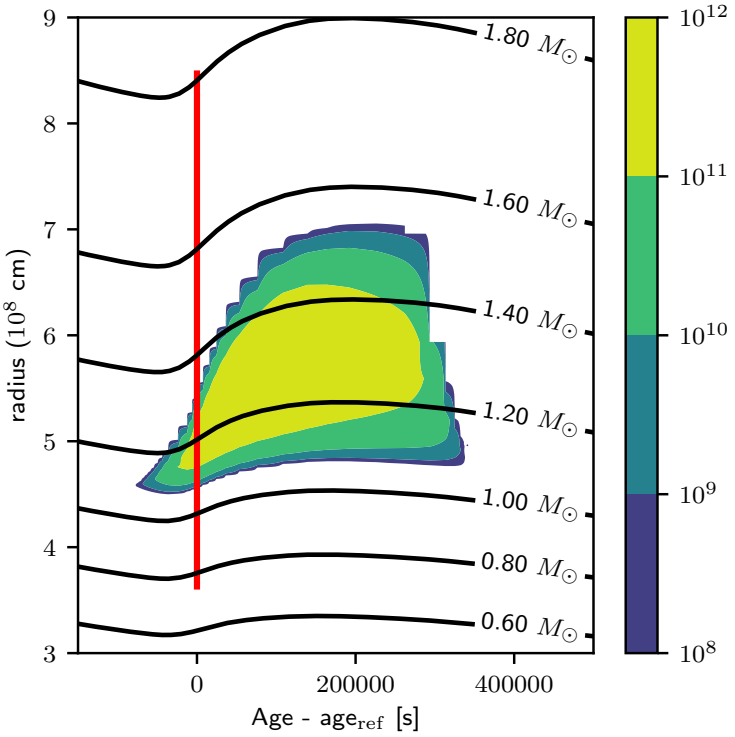

Figure 5.2: Zoom-in on the neon shell used as initial conditions, as a function of the time in seconds from the start of the 3D simulations. In colour scale, the squared convective velocity. Isomass contours are shown as black lines. The vertical red bar indicates the starting time and radial extent of the hydrodynamic simulations. Figure taken from Rizzuti et al. (2023).

and temperature between $4.5 < r < 5 \times 10^8$ as seeds for convective instabilities. The hydrostatic equilibrium has been recomputed in `PROMPI` as I described in the previous chapter. I used here a grid in spherical coordinates with a radial extent $3.6 < r < 8.5 \times 10^8$ cm and an angular size of 26° in both θ and φ. The boundary conditions are reflective at the top and bottom domains, and periodic at the lateral sides. As before, a velocity-damping region is present between $3.6 < r < 3.9 \times 10^8$ cm.

By making use of a spherical coordinate system, I can introduce a time-dependent gravitational term; thus, gravity is recomputed at each time-step according to equation (3.33), allowing for a contraction or expansion of the layers. Since the radial extent of the grid is approximately twice the size in the other dimensions, I used here a resolution with twice the number of cells in radius. The grid is linear in θ and φ but not in r, to account for the fact that in spherical coordinates the cell size increases with the radius. Starting from the innermost radius $R_{\rm min}$ towards the outermost $R_{\rm max}$, the next grid point $r(i+1)$ is obtained by multiplying the previous $r(i)$ by a constant factor that includes the radial resolution N_r:

$$r(i+1) = r(i)\, \exp\left\{\left(\frac{R_{\rm max}}{R_{\rm min}}\right)^{1/N_r} - 1\right\} \tag{5.1}$$

so that the last grid point, as expected, is

$$r(N_r) = R_{\rm min}\left(\exp\left\{\left(\frac{R_{\rm max}}{R_{\rm min}}\right)^{1/N_r} - 1\right\}\right)^{N_r} \simeq R_{\rm min}\left(\left(\frac{R_{\rm max}}{R_{\rm min}}\right)^{1/N_r}\right)^{N_r} = R_{\rm max} \tag{5.2}$$

The set of simulations run for the longest time range have a resolution of 256×128^2 grid points in r, θ, and φ, respectively; for a more detailed analysis of entrainment and other aspects I ran a set of simulations with higher resolution 512×256^2; finally, results have been validated with the very high-resolution simulations of 1024×512^2 and 2048×1024^2 grid points.

Convection in these simulations has been fuelled by an explicit nuclear burning routine. Differently from Chapter 4, where only the five key isotopes for

neon burning were included, I have now extended the nuclear network to include 12 isotopes: n, p, ^{4}He, ^{12}C, ^{16}O, ^{20}Ne, ^{23}Na, ^{24}Mg, ^{28}Si, ^{31}P, ^{32}S, and ^{56}Ni. This is the list of 11 isotopes I presented in Sec. 3.4.5, that can cover every burning phase from helium to oxygen, plus ^{56}Ni that is not involved in any of these reactions but has been added here to enforce the conservation of the total mass fraction. While the extension from 5 to 12 isotopes does not have any important effect on the neon-burning energy release, which was already accurate with just the five isotopes, this upgrade allows me to study the nucleosynthesis and transport of other species, as well as start testing the implementation of an extended nucleosynthesis in multi-D stellar models.
Making use of this nuclear burning routine, I included in my study simulations with and without boosted luminosity. A nominal-luminosity simulation is always present for every resolution, to validate the results and exclude the possibility that conclusions are influenced by the boosting. When a luminosity boosting is included, the nuclear rates for the neon-burning reactions $^{20}\mathrm{Ne}(\gamma,\alpha)^{16}\mathrm{O}$ and $^{20}\mathrm{Ne}(\alpha,\gamma)^{24}\mathrm{Mg}$ have been multiplied by a boosting factor. Since these reactions dominate the energy release, it does not make any difference that the other reactions have not been boosted. The boosting factors I used for these simulations are 1 (nominal luminosity), 5, 10, and 50.

5.2 Analysis of the fluid dynamics

In Table 5.1, I summarize the properties of the hydrodynamic simulations I present in this chapter, calculated with the `RANSX` library in the same way I did in Chapter 4. The code name of each simulation describes its radial resolution (`r`) and its boosting factor (`e`). We can see that simulations with different resolution but same boosting factor have very similar properties, and even the simulations with the lowest resolution seem already converged upon grid refinement. In particular, simulations `r256e1`, `r256e5`, `r256e10` and `r256e50` have

Table 5.1: Properties of the 3D hydrodynamic simulations presented in this chapter: model name; resolution $N_{r\theta\varphi}$; boosting factor of the driving luminosity ε; starting $t_{\rm start}$ and ending $t_{\rm end}$ time of the simulation; convective turnover time $\tau_{\rm c}$; number of convective turnovers simulated in the quasi-steady state $n_{\rm c}$; root-mean-square convective velocity $v_{\rm rms}$; sonic Mach number Ma; cost required to run the simulation in CPU core-hours.

name	$N_{r\theta\varphi}$	ε	$t_{\rm start}$ (10^3 s)	$t_{\rm end}$ (10^3 s)	$\tau_{\rm c}$ (s)	$n_{\rm c}$	$v_{\rm rms}$ (10^6 cm/s)	Ma (10^{-2})	cost (10^6 hr)
r256e1	256×128^2	1	0	60	155	96	3.29	0.83	2.08
r256e5	256×128^2	5	0	29	59	25	6.55	1.76	0.89
r256e10	256×128^2	10	0	19	50	16	8.06	2.15	0.60
r256e50	256×128^2	50	0	30	30	5	13.1	3.48	0.96
r512e1	512×256^2	1	16	19	136	22	3.83	0.99	1.66
r512e5	512×256^2	5	0	2	59	25	6.65	1.80	0.80
r512e10	512×256^2	10	0	1	49	16	8.28	2.23	0.50
r512e50	512×256^2	50	0	0.49	30	5	13.4	3.61	0.20
r1024e1	1024×512^2	1	10	10.4	127	3	3.26	0.84	2.88
r2048e1	2048×1024^2	1	10.01	10.03	113	0	3.85	0.99	2.02

been run until the complete exhaustion of neon in the shell, taking around 5 to 16 hours depending on the boosting, while the other simulations are higher-resolution versions of that set, with `r512e1` that has been restarted from `r256e1` at 16 000 s, together with `r1024e1` and `r2048e1` that have been restarted at 10 000 s and run only for a short time range due to their high computing cost (notice that running 20 s of `r2048e1` has the same cost as running 60 000 s of `r256e1`).

As a starting point, I present in Fig. 5.3 a vertical cross-section of the neon mass fraction in colour scale from the highest-resolution `r2048e1` simulation. This plot serves the double purpose of showing the fine detail that this hydrodynamic simulation can reveal, and also presenting the mixing of neon-rich and neon-poor material inside the convective zone, together with the entrainment of some neon-rich material (in red) from the upper stable region, underlining the importance and occurrence of CBM in this stellar environment. In this

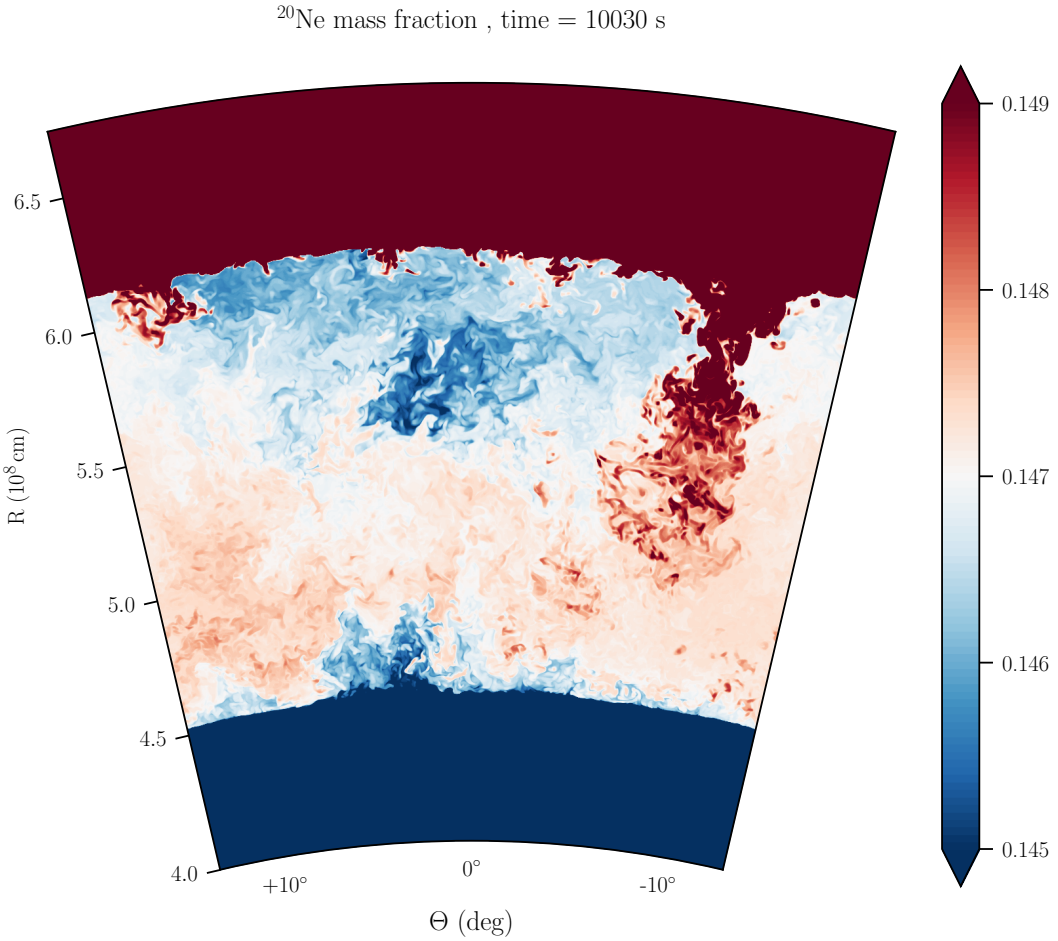

Figure 5.3: Cross-section from the `r2048e1` simulation with the neon mass fraction in colour scale. In addition to presenting the high resolution of the simulation, the frame also shows the entrainment of some neon-rich material from the upper stable region into the convective zone. Figure taken from Rizzuti et al. (2023).

context, the entrainment of fresh fuel is crucial because it can extend the nuclear burning time-scale and therefore the lifetime of the convective shell.
In Fig. 5.4, I show the effects of the mixing on the convective boundaries. In the top panel, I present the difference in mean atomic mass and entropy between the 1D initial conditions and a 3D `r512e1` test simulation run for five convective turnovers. I also superimposed on the profiles the grid points of the 3D simulation, to show the resolution used to resolve the convection boundaries. The mean atomic mass and entropy for $r < 5.4 \times 10^8$ cm do not match perfectly ($\sim 10^{-4}$ relative difference) because of the remapping and the small mixing that occurs during the initial transient. The figure shows that the convective boundary shifts outwards due to CBM, and both the chemical composition and the entropy are consequently mixed. The bottom panel of Fig. 5.4 shows the actual and adiabatic temperature gradients, defined in (2.8), for the same models. Both the 1D and 3D stellar models deviate from the adiabatic temperature gradient outside the convective region, so in the 3D simulation the CBM has altered the temperature gradient in the overshooting region $5.5 < r < 5.7 \times 10^8$ cm, that has become adiabatic unlike the 1D model. These two plots show very clearly that the 1D `MESA` code reproduces accurately the composition mixing, because the boundary shape in $\bar{A}$ is similar to the 3D one, but the entropy profile is visibly different, therefore it is necessary to include also the mixing of entropy in 1D models.
In Fig. 5.5, I present the time evolution of the specific turbulent kinetic energy integrated across the domain; the specific turbulent kinetic energy at radius r has been defined using the Reynolds averages of the velocity components (see Sec. 3.5.2):

$$E_{\mathrm{TK}}(r) = \frac{1}{2}\left(\overline{v_r^2} - \overline{v_r}^2 + \overline{v_\theta^2} - \overline{v_\theta}^2 + \overline{v_\varphi^2} - \overline{v_\varphi}^2\right) \tag{5.3}$$

and $E_{\mathrm{TK}}(r)$ has been integrated in volume across the entire shell domain, from $R_{\min} = 3.6 \times 10^8$ cm to $R_{\max} = 8.5 \times 10^8$ cm, to obtain the total energy:

$$E_{\mathrm{TK}}^{\mathrm{tot}} = \frac{3}{4\pi\left(R_{\max}^3 - R_{\min}^3\right)} \int_{R_{\min}}^{R_{\max}} E_{\mathrm{TK}}(r)\, 4\pi r^2 \,\mathrm{d}r \tag{5.4}$$

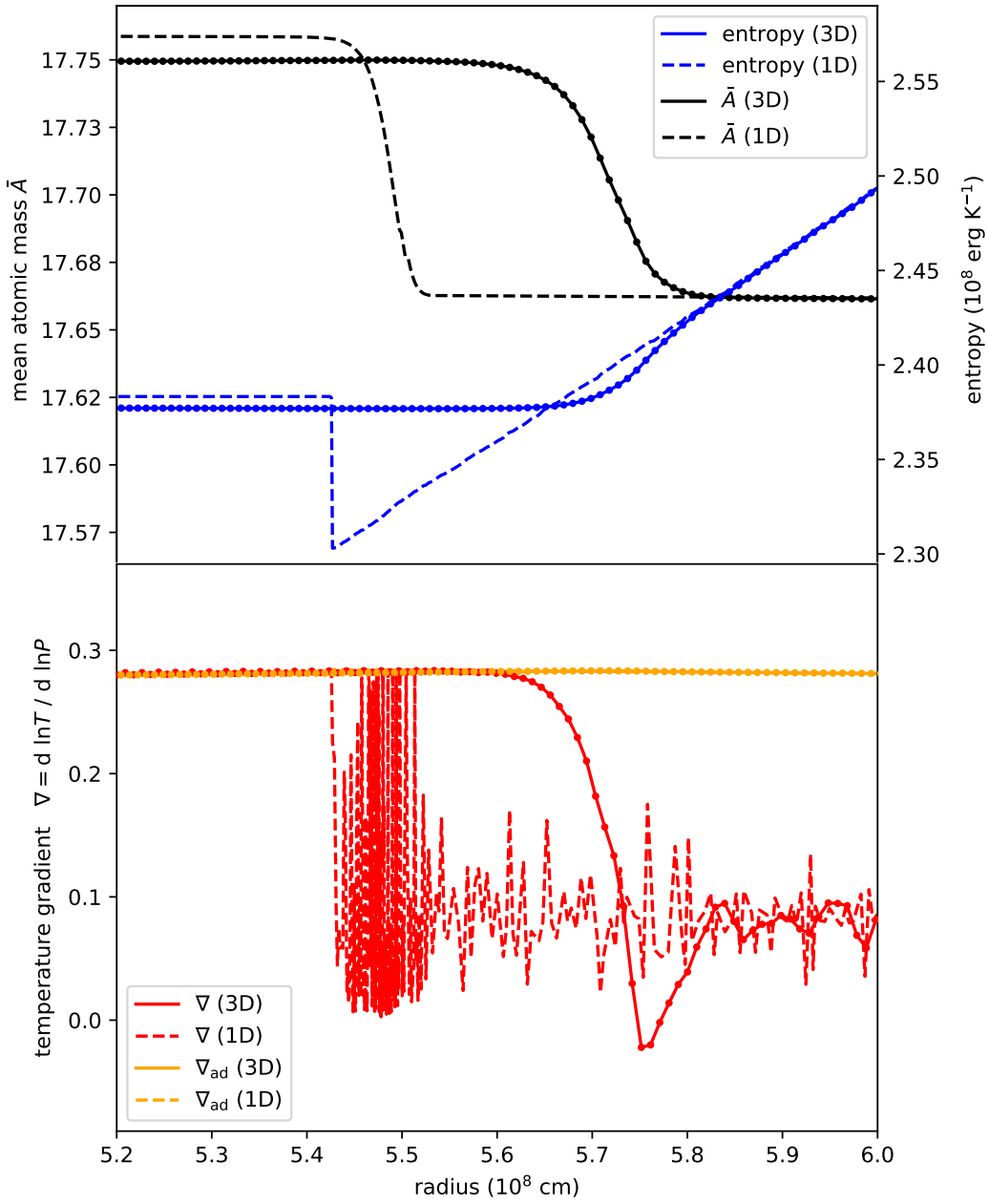

Figure 5.4: Radial profiles of the mean atomic mass $\bar{A}$ in black and entropy in blue (top panel), and of the actual temperature gradient ∇ in red and the adiabatic temperature gradient $\nabla_{\rm ad}$ in yellow (bottom panel), for the 1D input model (dashed lines) and at the end of a 3D `r512e1` test simulation (solid lines are angularly averaged quantities) run for 5 convective turnovers. The dots on the 3D curves indicate the mesh grid. Figures taken from Rizzuti et al. (2023).

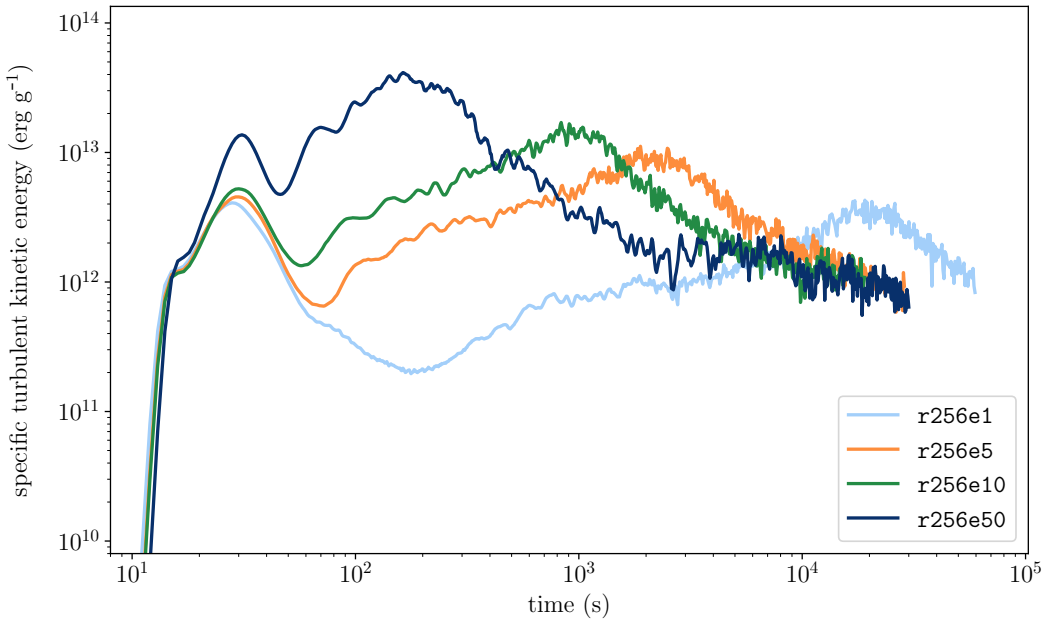

Figure 5.5: Time evolution of the specific turbulent kinetic energy for the four simulations with different luminosity boosting, `r256e1`, `r256e5`, `r256e10`, and `r256e50`. Figure taken from Rizzuti et al. (2023).

In the figure, I show the evolution of the simulations with the longest time range, the set `r256e1`, `r256e5`, `r256e10`, `r256e50`. The difference in luminosity boosting between the simulations explains the different trends. The kinetic energy builds up during the initial transient; afterwards, all simulations evolve with similar trends, gradually increasing the kinetic energy during the first phase (the nuclear-burning phase), followed by a slow decrease after all neon is consumed in the convective zone and nuclear burning cannot sustain the kinetic energy any longer. Primarily, the luminosity boosting affects the magnitude of the kinetic energy and the time-scale of the simulations, since the nuclear rates control the amount of energy produced and how rapidly the fuel is consumed, therefore the nuclear burning time-scale. In the plot, the peaks in kinetic energy occur approximately at 20 000, 2200, 960 and 180 seconds for `r256e1`, `r256e5`, `r256e10` and `r256e50`, respectively, and the neon mass

fraction left in the convective shell is about 6 per cent in all cases.

From Fig. 5.5, it is also possible to see that, after fuel exhaustion, the turbulent kinetic energy of all simulations seems to converge towards a value of $\sim 10^{12}$ erg g^{-1}, regardless of the boosting factor. This can be explained considering that after neon is exhausted the burning reactions $^{20}\mathrm{Ne}(\gamma,\alpha)^{16}\mathrm{O}$ and $^{20}\mathrm{Ne}(\alpha,\gamma)^{24}\mathrm{Mg}$ stop occurring, but the secondary $^{24}\mathrm{Mg}(\alpha,\gamma)^{28}\mathrm{Si}$ can still proceed due to the abundant magnesium residue, and this reaction was not boosted so it has the same rate in all simulations. However, this "magnesium burning" is not energetic enough to sustain convection as before with neon burning, so turbulence slowly decays and the shell growth halts.

Another way of studying the time evolution of the turbulent kinetic energy is presented in Fig. 5.6, where I plot $E_{\mathrm{TK}}(r)$ versus time with values in colour scale. As we saw before, apart from the difference in energy magnitude and time-scale, all simulations share a very similar evolution, with a first period dominated by nuclear burning and entrainment, demonstrating a linear growth of the shell, followed by fuel exhaustion and the slow dissipation of convection, as evident from the drop in kinetic energy, halting the shell growth. Additionally, another weak burning front is visible around $r \sim 8 \times 10^8$ cm, which is produced by the impact of gravity waves on a carbon shell above the neon one, but its energy is three orders of magnitude lower than in the neon-burning shell, so it has no impact on convection or entrainment.

These results have important implications for stellar evolution. Previous studies (e.g. Cristini et al., 2019; Horst et al., 2021; Rizzuti et al., 2022) supposed that the strong CBM predicted from hydrodynamic simulations would eventually lead to the convective engulfment of the entire star, but the new simulations I present here show that the shell naturally halts its growth once fuel is exhausted. Indeed, it is possible to estimate the nuclear burning time-scale by using nuclear network calculations in a one-zone model starting from the same initial conditions as the 3D simulations, to exclude the contribution from convective mixing. In this way, the nuclear burning time-scale $X_{\mathrm{Ne}}/\dot{X}_{\mathrm{Ne}}$

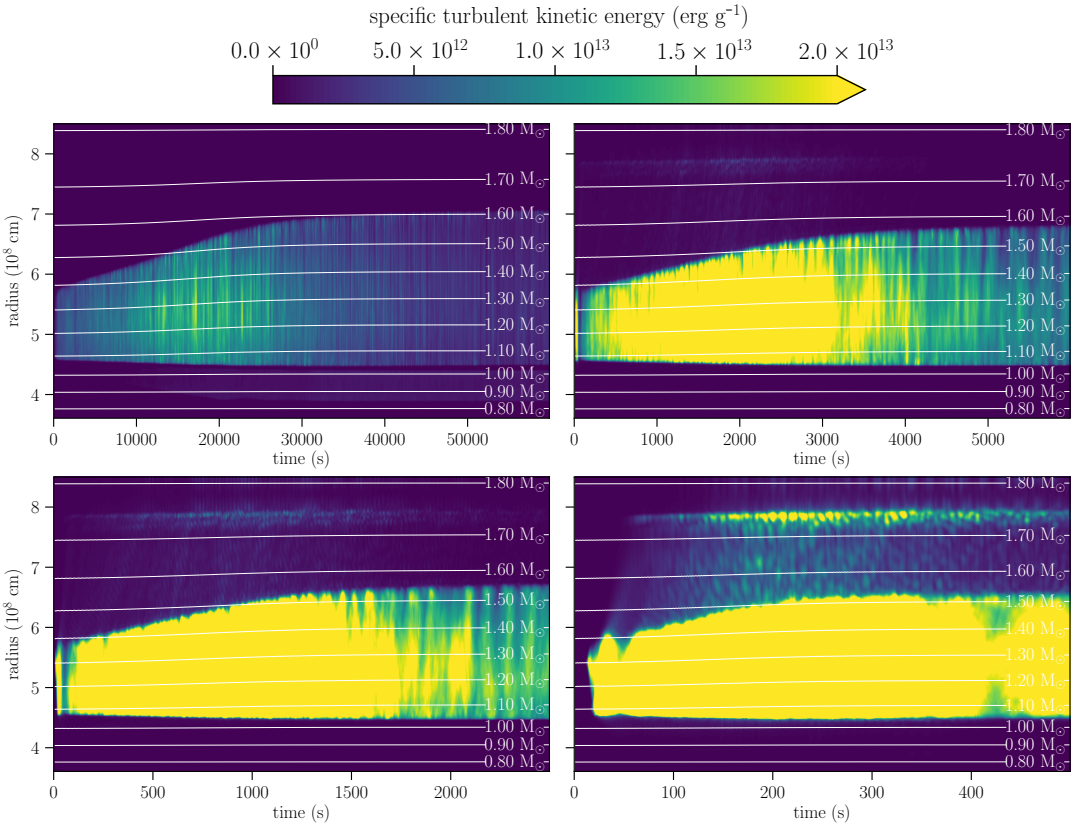

Figure 5.6: Time evolution of the specific turbulent kinetic energy for the four simulations with different luminosity boosting, `r256e1`, `r256e5`, `r256e10`, and `r256e50`. Figure taken from Rizzuti et al. (2023).

in the neon shell is estimated around 4000 seconds, which is much shorter than the time-scale for mass entrainment $M_{\rm entr}/\dot{M}_{\rm entr}$ around 30 000 seconds in the nominal-luminosity simulation. We can conclude that the entrainment of fresh fuel cannot sustain convection on its own. This finding puts a limit on the extent that convective zones can reach in stars, which has an important impact particularly on the evolution of massive stars and on their final structure.

5.2.1 Nuclear burning time-scale: a fast evolution

If we compare the nominal-luminosity simulation in the first panel of Fig. 5.6 to the corresponding shell evolution of the 1D model in Fig. 5.2, it appears evident that the convective shell in the 3D model evolves approximately ~ 5 times faster than its 1D equivalent. Understanding this difference is not trivial. In Fig. 5.6, I overlaid some isomass contours in white so that the expansion of the layers can be seen, as I did also in Fig. 5.2. In the 3D simulations, the contours show a small expansion of the layers around the convective zone, but no expansion is allowed close to the upper and lower domain boundaries, because mass flow is not allowed to pass through. Instead, in the 1D model around the neon shell a strong expansion of the layers is present, because they are not limited by domain boundaries but are free to contract or expand. This difference in convective zone size between 1D and 3D models can also explain the difference in burning time-scale. This is because the neon-burning energy release is strongly dependent on the temperature, according to a power of $\sim T^{50}$ (Woosley et al., 2002) due to the temperature dependence of the nuclear reaction rates and the α-particle mass fraction, and the temperature of a gas is dependent on its volume, according to its equation of state. Therefore, the expansion has an impact on the nuclear time-scale through a difference in volume and temperature between the 1D and the 3D shells.

I show here with a simple calculation that the volume difference between the final states of the convective zone in 1D versus 3D can explain the difference

in time-scales. Assuming for simplicity that the two states are separated by an adiabatic expansion (it is reasonable to assume no heat exchange with the surroundings), it is true that:

$$\frac{T_{3D}}{T_{1D}} = \left(\frac{V_{1D}}{V_{3D}}\right)^{\gamma-1} = \left(\frac{R_{1D}^3 - r_{1D}^3}{R_{3D}^3 - r_{3D}^3}\right)^{\gamma-1} \tag{5.5}$$

having expressed the temperature ratio of the simulations in terms of the inner r and outer R radii of the shells, and of the heat capacity ratio γ. Comparing the 1D and 3D models at the end of the nominal-luminosity neon burning, when the neon abundance is $X_{\mathrm{Ne}} \sim 0.015$, the radii in units of 10^8 cm are $R_{1D} = 7.34,\ r_{1D} = 4.63,\ R_{3D} = 6.93,\ r_{3D} = 4.44$. From the equation of state of the 3D model we get $\gamma = 1.55$, therefore the ratio in (5.5) results $T_{3D}/T_{1D} = 1.11$. The actual temperatures found in the simulations at the bottom of the convective shell, where the burning is taking place, are $T_{3D} = 1.88$ GK and $T_{1D} = 1.78$ GK, corresponding to a ratio of 1.06. From these values we can conclude that the limited expansion in the 3D simulations due to the closed boundary conditions can account for the higher temperatures compared to the 1D input model.

Now we can estimate the effect of the larger temperature reached in 3D on the nuclear time-scale. The nuclear energy generation rate can be expressed as a power of the temperature $\dot{\varepsilon} \sim T^{\alpha}$, thus the difference in nuclear burning time-scale, defined as $\tau \sim 1/\dot{\varepsilon}$, becomes:

$$\frac{\tau_{3D}}{\tau_{1D}} \sim \left(\frac{T_{1D}}{T_{3D}}\right)^{\alpha} \tag{5.6}$$

Woosley et al. (2002) suggested a value of $\alpha = 50$ for neon burning; using the temperature ratio $T_{1D}/T_{3D} = 1.78/1.88$, the result is a 3D time-scale that is 15 times shorter than the 1D one. This is much faster than what we see in the simulations, for which the non-boosted case is only ~ 5 times faster; this is because the energy generation rate is also dependent on the neon abundance, which decreases with time, therefore the value of α is expected to decrease in time as neon is depleted.

Both the 1D and 3D simulations are complex scenarios, but this simple calculation, estimating the effect of the expansion on the nuclear burning, shows how the difference in time-scale between the 3D and 1D models can be explained.

5.2.2 Spectral analysis and turbulence theory

As I did in the previous chapter, also for this set of simulations it is possible to compute and analyse the power spectrum of the kinetic energy. Since these new simulations employ a spherical system of coordinates, it would be reasonable to perform a spherical harmonic decomposition; however, the model domain reproduces only a small fraction of a sphere, covering 0.2 steradians or 2 per cent of the spherical surface, therefore it would be difficult to perform the decomposition. Horst et al. (2021) conducted a spherical harmonic decomposition on hydrodynamic simulations similar to the ones presented here, by repeating the pattern periodically until the entire spherical surface is covered, but this approach introduces artefacts from the surface remapping, and it is still unable to represent the low-order modes due to the lack of large-scale structures. I prefer here to compute the spectra of these simulations in the same way as I did in Sec. 4.3.1, using a 2D Fourier analysis. Fixing the radius in the middle of the convective region (in this case I chose $r = 5 \times 10^8$ cm), the definition of the Fourier transform in spherical coordinates for a quantity q is:

$$\hat{q}(k_\theta, k_\varphi) = \frac{1}{N_\theta N_\varphi} \sum_{n_\theta=0}^{N_\theta-1} \sum_{n_\varphi=0}^{N_\varphi-1} q(\theta, \varphi)\, \mathrm{e}^{-i\,2\pi\left(\frac{k_\theta n_\theta}{N_\theta}+\frac{k_\varphi n_\varphi}{N_\varphi}\right)} \tag{5.7}$$

with N_θ, N_φ the numerical resolution, n_θ, n_φ the cell numbers, and k_θ, k_φ the wavenumbers, which span the range:

$$\begin{aligned} k_\theta &= \begin{cases} i, & \text{if} \quad 0 \le i < N_\theta/2 \\ i - N_\theta, & \text{if} \quad N_\theta/2 \le i < N_\theta \end{cases} \\ k_\varphi &= \begin{cases} j, & \text{if} \quad 0 \le j < N_\varphi/2 \\ j - N_\varphi, & \text{if} \quad N_\varphi/2 \le j < N_\varphi \end{cases} \end{aligned} \tag{5.8}$$

Employing these definitions, I compute the term $\frac{1}{2}|\hat{v}_{\rm rms}|^2$ that can be interpreted as the power spectrum of the specific kinetic energy, as a function of the wave number $k = \sqrt{k_\theta^2 + k_\varphi^2}$. As before, the range is limited to $k \in [0, \min\{N_\theta/2, N_\varphi/2\}]$ to avoid losing any signal.

In Fig. 5.7 (top panel) I show the spectra for simulations at nominal luminosity but with different resolution; these spectra have been averaged over one convective turnover, except for `r2048e1` that has been averaged for the last 10 s due to its very short time-scale. The bulk of the spectra follow the expected Kolmogorov scaling, a confirmation that the simulations have a large inertial range. As expected, the spectra deviate from Kolmogorov's $k^{-5/3}$ scaling both at the largest scales, around the vertical line at $k \sim 2$, due to the anisotropy of the flow, and at the smallest scales due to the numerical dissipation at the grid scale. As the resolution increases the inertial range extends towards larger wave numbers, because dissipation takes place on smaller real-space scales; the spectra start deviating strongly from $k^{-5/3}$ around a scale that corresponds to 15 cells for all simulations, as represented in the plot with vertical dotted lines around $k \sim 8$ - 70.

On the other hand, I also present in Fig. 5.7 (bottom panel) the spectra for simulations with same resolution but different boosting factors, averaged over one convective turnover. As expected, the specific kinetic energy increases with the boosting factor, but the extent of the inertial range does not change since the resolution is the same. This confirms the fact that the boosting factor does not affect the properties of the turbulent flow apart from the magnitude of the kinetic energy.

5.3 Entrainment analysis and parametrization

In this section, I show results concerning the analysis and parametrization of entrainment in the new set of simulations. I refer to the analysis of the simu-

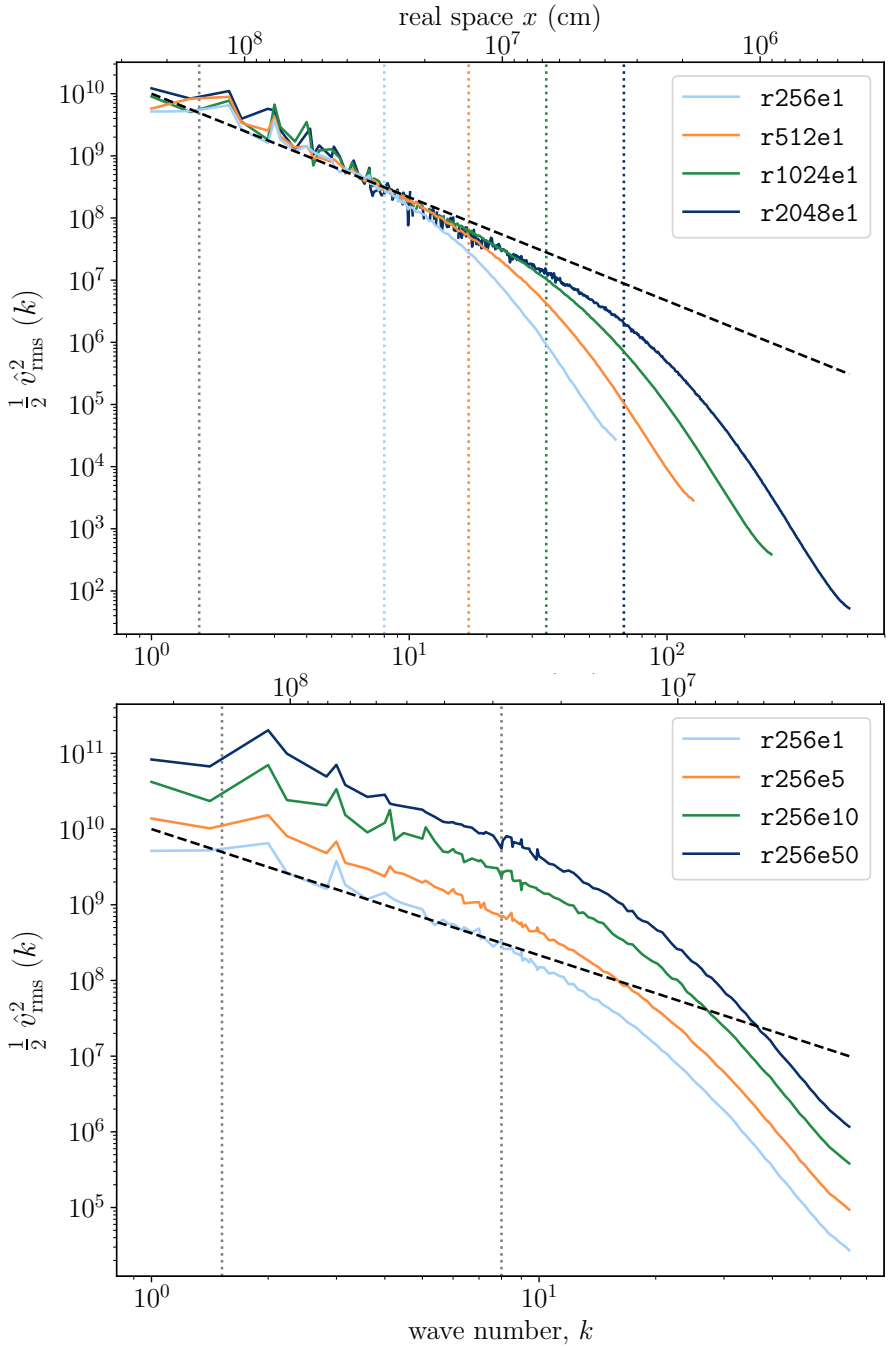

Figure 5.7: Spectra of the specific kinetic energy as function of the wave number k and the real space x, for simulations with different resolution (top panel) and with different boosting factors (bottom panel). The dashed black line is the Kolmogorov scaling $k^{-5/3}$; the vertical dotted line at $k \sim 2$ is the size of the convective region; the vertical dotted lines at $k \sim 8$ - 70 correspond to 15 cells for each resolution. Figures taken from Rizzuti et al. (2023).

Table 5.2: List of measurements from the simulations in this chapter used for the entrainment analysis: model name; root-mean-square convective velocity $v_{\rm rms}$; upper entrainment rate $v_{\rm e}^{\rm up}/v_{\rm rms}$; lower entrainment rate $v_{\rm e}^{\rm low}/v_{\rm rms}$; upper bulk Richardson number $\mathrm{Ri}_{\rm B}^{\rm up}$; lower bulk Richardson number $\mathrm{Ri}_{\rm B}^{\rm low}$.

`name`	$v_{\rm rms}$ (cm s^{-1})	$v_{\rm e}^{\rm up}/v_{\rm rms}$	$v_{\rm e}^{\rm low}/v_{\rm rms}$	$\mathrm{Ri}_{\rm B}^{\rm up}$	$\mathrm{Ri}_{\rm B}^{\rm low}$
`r512e1`	3.83×10^{6}	1.01×10^{-3}	5.38×10^{-5}	51.3	224
`r512e5`	6.65×10^{6}	5.03×10^{-3}	3.69×10^{-4}	13.8	64.7
`r512e10`	8.28×10^{6}	8.25×10^{-3}	6.54×10^{-4}	8.91	42.5
`r512e50`	1.34×10^{7}	2.72×10^{-2}	1.84×10^{-3}	2.63	15.3

lations in the previous chapter, in particular to Sec. 4.5.1, for the computation methods. Here, the convective boundary locations have been obtained using the angularly averaged neon mass fraction profiles, defining the boundary as the mid-point between the plateaus in the convective and in the radiative regions. As before, $v_{\rm e}$ is the entrainment velocity obtained as the time derivative of the boundary location, $v_{\rm rms}$ is the velocity inside the convective zone defined as $\left(\overline{v_r^2} + \overline{v_\theta^2} + \overline{v_\varphi^2}\right)^{1/2}$, and the length scale ℓ is set equal to 1/12 of the local pressure scale height. For the entrainment analysis, I selected the group of simulations `r512e1`, `r512e5`, `r512e10`, and `r512e50`, that have been run for enough convective turnovers to be statistically significant, and also have a high resolution to make sure that the boundaries are correctly resolved. All quantities have been averaged for the entire time the simulations spent in the entrainment regime. Figure 5.6 has shown that the growth of the convective zone follows the same slope at any point during the entrainment regime. The results are presented in Table 5.2.

In agreement with the results from the previous chapter, an increase in the boosting factor results in larger convective and entrainment velocities and smaller $\mathrm{Ri}_{\rm B}$ due to the larger penetrability. These results are used to estimate again the free parameter A, n that define the entrainment law (2.25).

For greater accuracy, instead of fitting the data with a linear regression in log scale, I used here an "orthogonal distance regression" that minimizes the squared perpendicular distance of the points from the fitting function. The `scipy.odr` library that I employed allows to take into account the errors in both x- and y-axes, and gives the possibility of fitting an arbitrary function, in this case a power law.

The measurements of entrainment rates, bulk Richardson numbers and the fitting laws are shown in Fig. 5.8, where I compare the results from this new work (in blue) to the simulations of the neon shell from Chapter 4 (in red), and to the 1D entrainment study of a convective hydrogen core in a 15 $M_\odot$ star from Scott et al. (2021) (in black). The error bars are standard deviations of the values at each time-step of the simulations, and since the new fitting has been done in real space, the plot in log scale can show some of the bars going towards zero.

The plot in Fig. 5.8 shows different values of $\mathrm{Ri_B}$ estimated both in late convective phases (data points, $\mathrm{Ri_B} \sim 1$ - 10^3) and in the main-sequence core (vertical line, $\mathrm{Ri_B} \sim 10^5$); the main reason of the disagreement between 1D and 3D models is the inability of running non-boosted hydrodynamic simulations of the convective cores, and the consequent need to extrapolate entrainment rates at very large $\mathrm{Ri_B}$. But Fig. 5.8 also shows an interesting result of the new simulations: the new entrainment law estimated from the present work appears to be intermediate between the previous multi-D simulations and the 1D prescription, being potentially able to explain and reproduce entrainment both at small and large $\mathrm{Ri_B}$.

This result is confirmed by the plot of Fig. 5.9, where I compare entrainment from all `PROMPI` simulations in the literature: the new simulations clearly have lower entrainment rates then all the previous multi-D measurements. These new rates are not as small as it would be predicted from the 1D entrainment law (the black line in Fig. 5.8), but the larger steepness and lower dispersion of the new rates produce an entrainment law that predicts much smaller rates

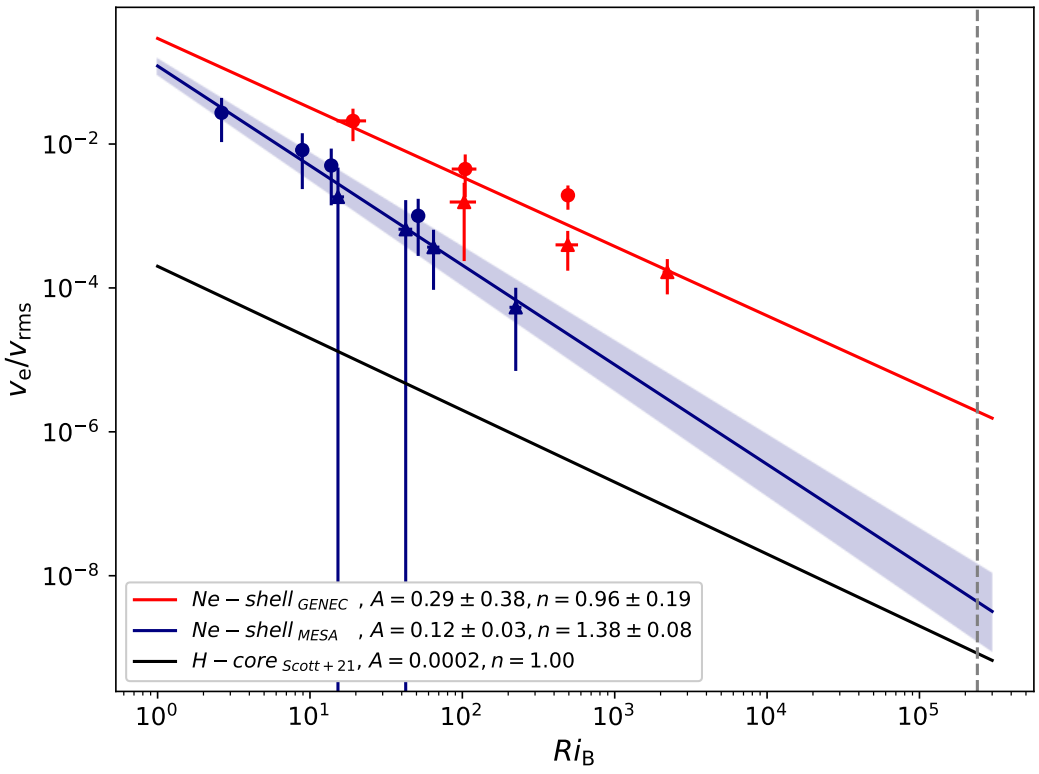

Figure 5.8: Entrainment rate versus bulk Richardson number, data from stellar simulations and respective linear regressions: "`MESA`" Ne-shell from this study (blue), "`GENEC`" Ne-shell from Chapter 4 (red), and H-core from 1D Scott et al. (2021) (black). Triangles are measurements for lower convective boundaries, circles for upper boundaries. The dashed vertical line indicates $\mathrm{Ri_B}$ in the convective H-core. Error bars are standard deviations. In the legend, parameter estimates for the entrainment law $v_\mathrm{e}/v_\mathrm{rms} = A\ \mathrm{Ri_B}^{-n}$. Figure taken from Rizzuti et al. (2023).

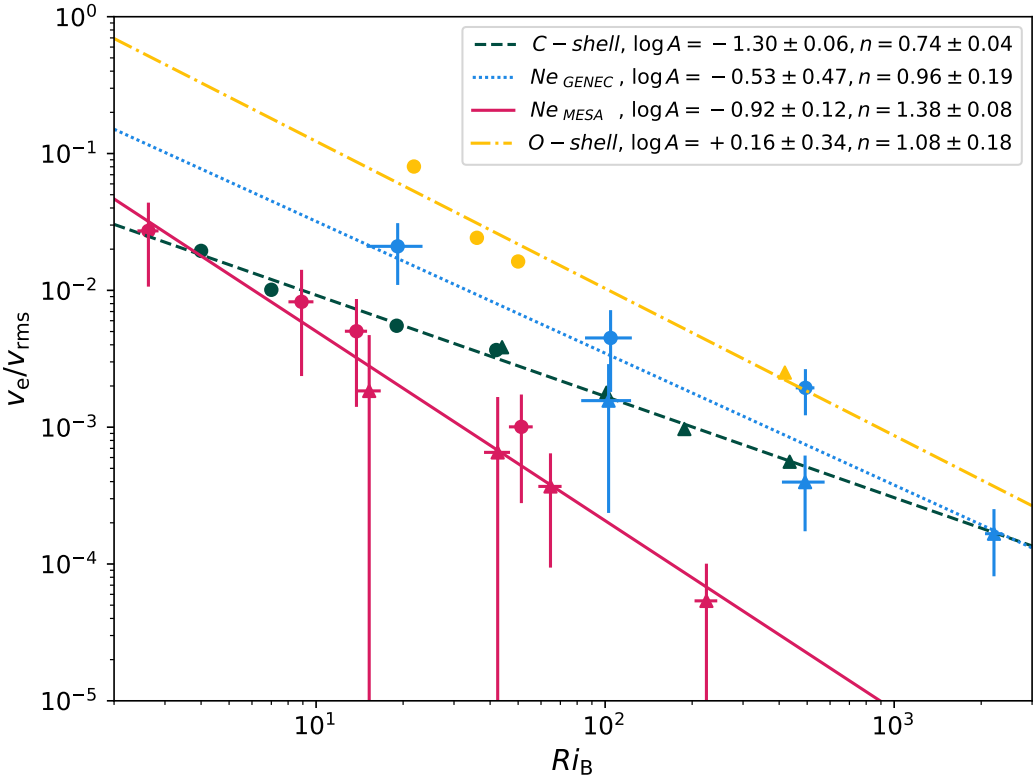

Figure 5.9: Same as Fig. 5.8, but comparison between different `PROMPI` simulations: "`MESA`" Ne-shell from this study (red, solid), "`GENEC`" Ne-shell from Chapter 4 (blue, dotted), C-shell from Cristini et al. (2019) (green, dashed), O-shell from Meakin & Arnett (2007) (yellow, dot-dashed). In the legend, parameter estimates for the entrainment law $v_e/v_{rms} = A\ \mathrm{Ri}_B^{-n}$. Figure taken from Rizzuti et al. (2023).

at larger Ri_B, in very good agreement with 1D models of the convective core. This new-found convergence between 1D and 3D stellar models is a direct result of the improvements implemented in the hydrodynamic models and in the initial conditions they were started from. The two sets of hydrodynamic simulations shown in Fig. 5.8 are both of a Ne-burning shell, with the same nuclear burning reactions and energy release, but the initial conditions were assumed from two very different 1D models: in Chapter 4, I used a `GENEC` model with

no CBM in this phase, while in this chapter I employed a `MESA` model with strong CBM for all phases. The stellar mass is also different, but previous hydrodynamic simulations of massive stars do no show any dependence of the entrainment law parameters on the stellar mass (see Fig. 5.9). Furthermore, the present set of simulations has been run for an entire evolutionary time-scale, which has never been done before.
The conclusion from the results presented in this section is that, when a hydrodynamic simulation is started from a 1D model that includes an up-to-date CBM prescription, the entrainment rate predicted from the 3D model is significantly more in agreement with the one from the 1D input model than simulations started from initial conditions with absent or underestimated CBM.

5.4 Nucleosynthesis and time evolution of the isotopes

In the set of simulations I present here, it is possible to study the time evolution and space distribution of the different isotopes included in the nuclear network. We have seen in the previous sections how the simulations evolve towards the complete depletion of neon and consequent decline of convection. To track the neon consumption, Figure 5.10 shows the time evolution of the neon abundance inside the convective zone, for the four simulations with different boosting factors `r256e1`, `r256e5`, `r256e10`, and `r256e50`. During the first $\sim$100 s, the fluctuations in neon abundance come from the propagation of convection throughout the convective region and the entrainment of some material from the neon-rich layers above; this initial trend is different in `r256e50` because neon is also consumed due to the high energy boosting. After this initial transient phase, the simulations consume neon on different time-scales but all with the same trend.
The chemical abundances can be studied with a mean-field statistical analysis,

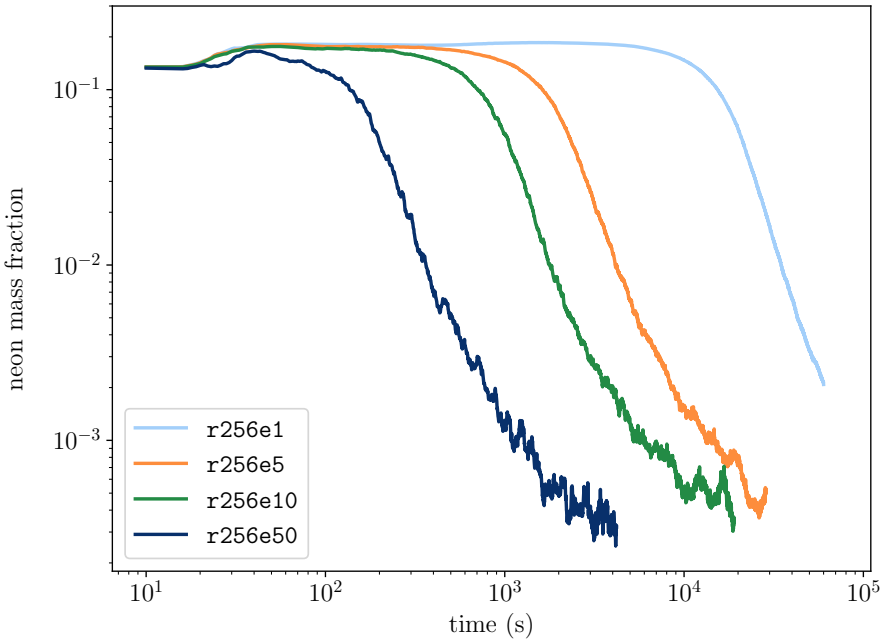

Figure 5.10: Time evolution of the ^{20}Ne mass fraction inside the convective region, for the four simulations with different boosting factors `r256e1`, `r256e5`, `r256e10`, and `r256e50`. Figure taken from Rizzuti et al. (2023).

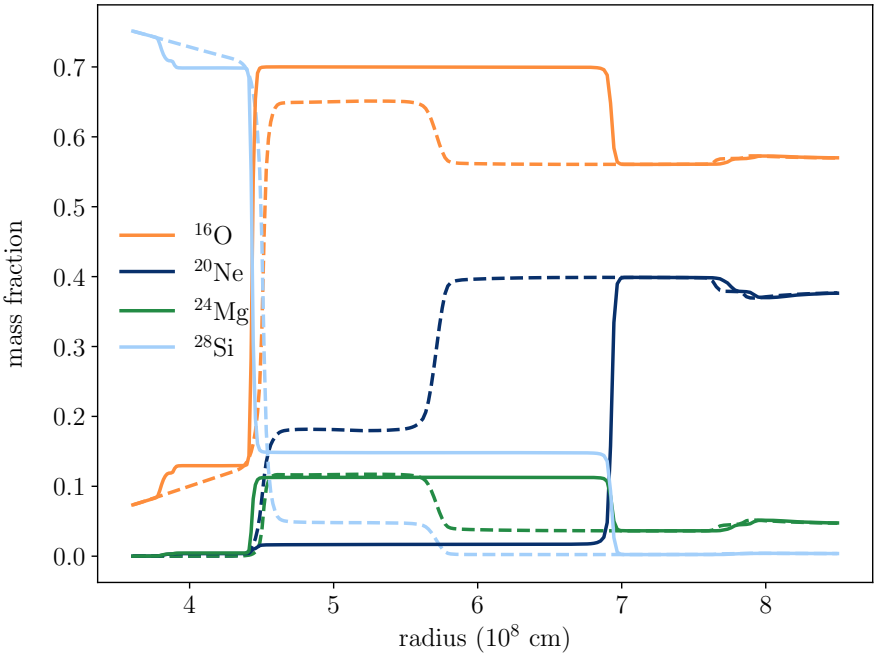

Figure 5.11: Angularly averaged mass fractions of ^{16}O, ^{20}Ne, ^{24}Mg, ^{28}Si as function of the stellar radius, at the beginning of the `r256e1` simulation (dashed) and after 8 hours (solid), towards the end of the convective phase.

employing the tools I presented in Sec. 3.5.2. I plot in Fig. 5.11 the initial and final mass fraction profiles, as dashed and solid lines respectively, of the four isotopes involved in neon burning from the simulation `r256e1`. The convective zone is identified by the central plateaus in the abundance profiles. We can see that at the beginning of the simulation the convective region extends from 4.5 to 5.8×10^8 cm, but by the end of the simulation it has almost doubled in size, as also visible in Fig. 5.6. Concerning the individual isotopes, the plot shows that ^{20}Ne has been completely consumed in the convective zone, due to the neon-burning reactions $^{20}\mathrm{Ne}(\gamma,\alpha)^{16}\mathrm{O}$ and $^{20}\mathrm{Ne}(\alpha,\gamma)^{24}\mathrm{Mg}$, therefore ^{16}O and ^{24}Mg have been produced as a result, but part of the ^{24}Mg has been converted to ^{28}Si according to $^{24}\mathrm{Mg}(\alpha,\gamma)^{28}\mathrm{Si}$.

We can also study the transport of the isotopes across the layers by plotting the

radial flux profiles, defined as $f_i = \overline{\varrho}\,\widetilde{X_i'' v_r''}$ for each species i. Figure 5.12 shows the flux profiles from the high-resolution `r1024e1` simulation, averaged over 3 convective turnovers. In this plot, positive and negative values of the flux represent upward and downward flows, respectively. The flux is dominated by the downward transport of ^{20}Ne towards the bottom of the convective zone, where the nuclear burning is taking place, while ^{16}O, ^{24}Mg and ^{28}Si are produced at the bottom and transported upwards, hence their positive fluxes. Outside the convective region, there is no mixing therefore no transport of species. However, immediately below the convective zone the flux is slightly positive for silicon and negative for oxygen and magnesium; this is because silicon is more abundant below the boundary so it is brought inside the convective zone by entrainment, while oxygen and magnesium are produced and more abundant above the boundary so they are transported downwards. Finally, the black line in Fig. 5.12 represents the sum of all the fluxes for the 12 isotopes included in the simulations, and it is always equal to zero, confirming that the sum of the mass fractions is conserved.

So far we have only seen angularly averaged quantities, but it is also interesting to study the horizontal fluctuations of the chemicals. For this purpose, I plot in Fig. 5.13 the standard deviation profiles of the mass fraction for ^{16}O, ^{20}Ne, ^{24}Mg, ^{28}Si, defined as $\sigma_i = (\widetilde{X_i'' X_i''})^{1/2}$ for a species i, with σ_i in the top panel and the normalized $\sigma_i/\bar{X}_i$ in the bottom panel of Fig. 5.13. The standard deviations represent the dispersion of the chemicals as function of the radius, therefore they can be used to measure the difference from a perfect spherical symmetry, as in the case of 1D models. The largest deviations can be found at the convective boundaries, due to the deformation of the boundary under the effects of entrainment and convective motions. Instead, inside the convective zone the mixing makes the composition homogeneous and reduces the dispersion. Small deviations are also present below the convective region, due to the fluctuations generated by entrainment and internal gravity waves.

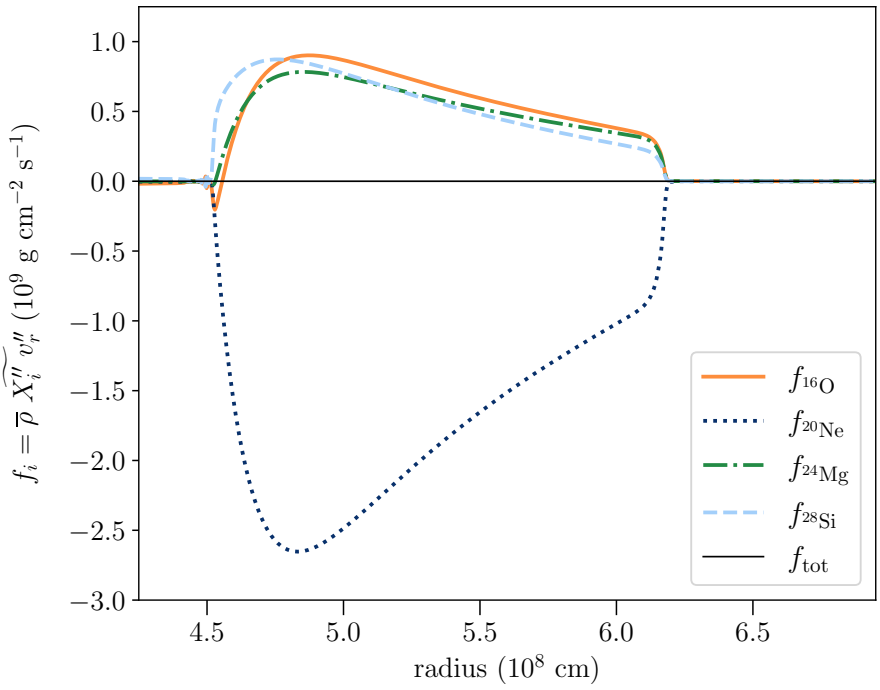

Figure 5.12: Flux profiles of ^{16}O, ^{20}Ne, ^{24}Mg, ^{28}Si as function of the stellar radius, from simulation `r1024e1`. The black line is the sum of the flux profiles for all the 12 isotopes in the network. Figure taken from Rizzuti et al. (2023).

The presence of an angular distribution of the chemicals can have a significant impact on the stellar nucleosynthesis. In these plots, the standard deviations are generally small, so there are no major differences from a perfect spherical symmetry, as expected for nucleosynthesis in normal convective burning episodes. The situation is different in more dynamic contexts, like in merging shells (e.g. Mocák et al., 2018, see also Chapter 6) or in cases where fuel is ingested into an unusual burning region (e.g. carbon ingestion into an oxygen-burning shell, Andrassy et al., 2020).

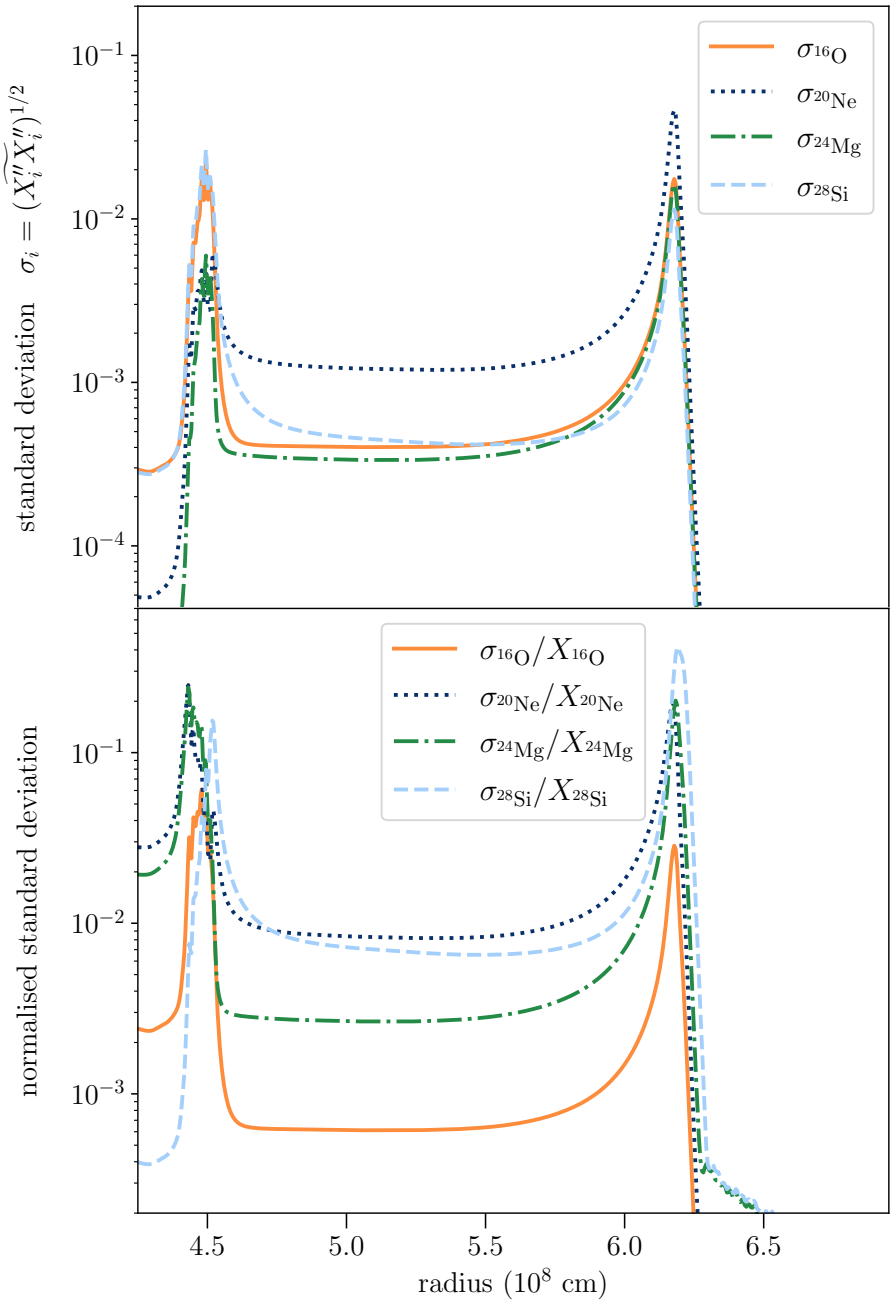

Figure 5.13: Standard deviation profiles σ_i (top panel) and normalized standard deviation profiles $\sigma_i/\bar{X}_i$ (bottom panel) of the mass fractions for ^{16}O, ^{20}Ne, ^{24}Mg, ^{28}Si, from simulation `r1024e1`. Figures taken from Rizzuti et al. (2023).

6 Shell merging and nucleosynthesis in 3D hydrodynamic simulations

6.1 Motivations and overview

The 1D stellar evolution model presented in Sec. 5.1.1, from which the 3D simulations of Chapter 5 have been started, shows a very interesting occurrence in the evolution of the star: the merging of multiple convective shells into a single convective region (see Fig. 5.1). This is a challenging environment to study, due to the complex interaction between convection, nuclear burning and entrainment, resulting in alternative dynamics and nucleosynthesis paths that are difficult to include in 1D models using simplifying prescriptions. These differences are expected to have a deep impact on the structure and chemical composition of the star, affecting the possible supernova explosion and chemical enrichment of the interstellar medium.

A major source of uncertainty related to the formation and evolution of convective shell mergers is the limited literature that investigates these episodes. 1D stellar evolution models have been reporting the occurrence of convective carbon-oxygen shell merging for a long time (Rauscher et al., 2002; Tur, Heger & Austin, 2007). These studies suggest that shell-merging events in evolved massive stars can be responsible for the production of isotopes that are difficult to explain otherwise, both during these convective phases and later on in the supernova explosions. Carbon-oxygen merging shells can be a principal source for the nucleosynthesis of the odd-Z elements P, Cl, K, and Sc, whose production is currently underestimated by Galactic chemical evolution models (see e.g. Cescutti et al., 2012 for the origin of phosphorus). Indeed, the heating of ingested carbon at oxygen-burning temperatures can trigger a sequence of γ-reactions, among which (γ, p) that release free protons and can produce odd-Z elements; this is sometimes called "p-process". Additionally, during the ex-

plosive nucleosynthesis in core-collapse supernovae, the carbon-oxygen merger sites can explain the production of rare proton-rich isotopes beyond iron. In this case, it is the collapse of the star that triggers the photodisintegration of heavy isotopes, which can produce in these layers the p-nuclei through a chain of photodisintegrations, also called "γ-process" (see Roberti et al., 2023).

Recently, a few works also started studying these events employing hydrodynamic models. Ritter et al. (2018) have performed 3D hydrodynamic simulations of carbon ingestion from a stable layer into a convective oxygen-burning shell, assuming a stratification based on a 25 $M_\odot$ stellar evolution model. The nucleosynthesis in their simulations, computed with a 1D multi-zone post-processing code, confirms that the high entrainment rates boost the production of the odd-Z elements ^{31}P, ^{35}Cl, ^{39}K, and ^{45}Sc through (γ, p) reactions. Their study also shows that the consequent explosive nucleosynthesis does not reprocess these elements, indicating that their principal production sites are the convective merging shells.

Andrassy et al. (2020) further investigated the ingestion of carbon into a convective oxygen-burning shell using 3D simulations that include explicit carbon- and oxygen-burning reactions. In addition to confirming the entrainment rates found in Ritter et al. (2018), they estimate that the carbon-burning inside the oxygen shell can contribute to 14 - 33 per cent of the total luminosity of the shell, showing how impactful the extra burning can be.

Finally, Mocák et al. (2018) have studied the merging of neon and oxygen shells in a 23 $M_\odot$ star, simulating the ingestion of neon into a convective oxygen-burning shell with the `PROMPI` code in spherical geometry. They included an explicit 25-isotope network that can reproduce the energy release dominated by oxygen- and neon-burning inside the convective shell. In particular, the neon burning results from the mixing of entrained material into the convective oxygen layers, while oxygen burning is enhanced by the additional fuel mixed from the stable regions. As a result, a new quasi-steady state is reached and the simulation predicts two burning shells within a single convective zone, with

two distinct peaks in nuclear energy generation.
As ground-breaking as these studies are, they focus their attention on situations where an alternative fuel is ingested from a stable region into a convective one, affecting its nucleosynthesis; this represents the merging of a convective region with a stable one. Instead, the 1D model of Fig. 5.1, representative of many other stellar simulations, shows the merging of multiple shells of different composition, but all convective. The evolution of convective shells that begin their life as separate and later merge has never been explored in the literature with multi-D simulations. Nevertheless, it is an interesting environment to simulate, not only for the peculiar nucleosynthesis paths that it can enable, but also for the effects of these extreme dynamics on the stellar structure, as visible from the large convective shell generated by the merging in Fig. 5.1.
In this chapter, I present results from a set of 3D hydrodynamic simulations of a shell merging event predicted by the 321D-guided model introduced earlier. Analysing both the dynamics and nucleosynthesis of this environment allows me to shed light on the relatively unexplored shell-merging events, drawing conclusions of great interest for the stellar structure and chemical evolution theory. Additionally, I used this opportunity to push the `PROMPI` code towards an even more realistic setup, implementing a nearly 4π geometry in addition to a spherical system of coordinates, a 12-isotope network for nuclear burning, and the high resolution common to the simulations presented in the previous chapters.

6.1.1 Setup of the simulations

As mentioned above, the initial conditions for the new 3D simulations presented in this chapter have been assumed from the same 20 $M_\odot$ 1D stellar evolution model used in Chapter 5; see Sec. 5.1.1 for a description. I focus my attention here on the time interval in Fig. 5.1 between 10^{-2} - 10^{-4} yr before the predicted collapse of the star; I present a zoom-in of this region in Fig. 6.1.

From this plot, it is possible to see that three distinct convective regions exist at the start of the 3D simulations, and they all are predicted to merge after 10 000 s. A fourth convective shell is predicted to form below the others after the 3D simulation starting time, but it does not merge with the others and halts around 10 000 s. One first question that the hydrodynamic simulations shall answer is whether a merging takes place in the 3D model within the simulated time range or not. Furthermore, Figure 6.1 shows from the isomass contours that no major expansion is predicted to occur during the time range of the 3D simulations; even if an expansion of the layers takes place during the shell merging in 3D, the large radial extent selected for the simulations is expected to contain this problem.

The remapping of variables from 1D to 3D has been carried out exactly as described in Sec. 5.1.1 for the previous set of simulations, including adding seed perturbations between 6 - 7 $\times$ 10^8 cm and between 9.5 - 12 $\times$ 10^8 cm. For this study, I present two different simulations in spherical geometry, starting from the same initial conditions. Both simulations have a radial extent of $0.3 < r < 6.8 \times 10^9$ cm, as also shown in Fig. 6.1, but the angular range covered by θ and φ is different. One setup is a 3D wedge with the same angular size of 60° in both θ and φ, and resolution 768×256^2 in r, θ and φ; I code-name it `a60n256` after its angular size and resolution. The other setup has instead a size of 90° in θ and 360° in φ, and resolution $512 \times 256 \times 1024$ in r, θ and φ; I code-name it `a360n1024`. The reason for running these two simulations is to study the evolution of the same initial conditions in the two different geometries. In particular, `a60n256` has a higher local resolution but more limited spatial extent, while `a360n1024` is closer to a 4π solid angle, covering over 70 per cent of the spherical surface, at the cost of a slightly lower local resolution. The reason why the `PROMPI` code cannot perform full 4π simulations is explained in Sec. 3.4.2: the spherical grid presents singularities at the centre and along the polar axis of the sphere, therefore artefacts are produced by the code the closer the domain approaches these points in space. However, it

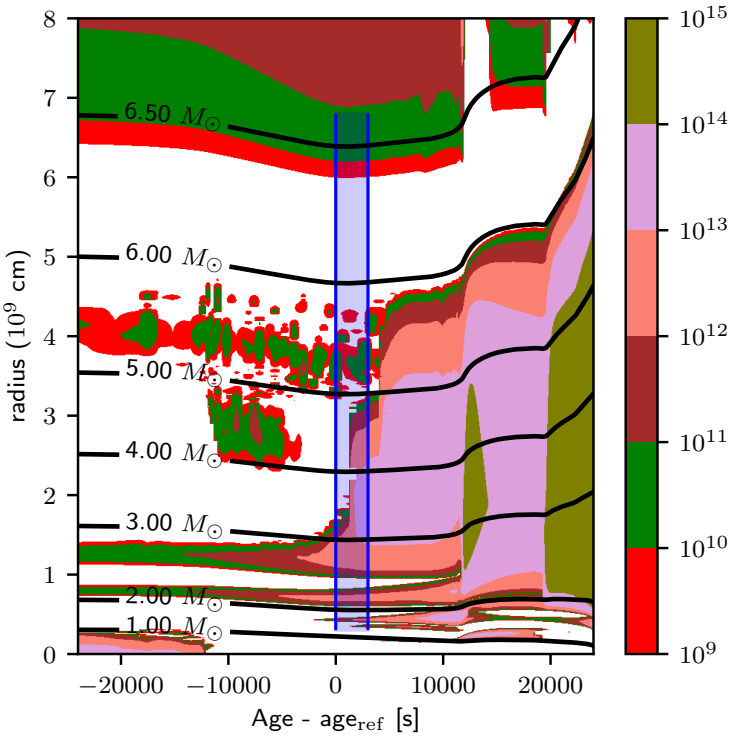

Figure 6.1: Zoom-in on the convective shells used as initial conditions, as a function of the time in seconds from the start of the 3D simulations. In colour scale, the squared convective velocity. Isomass contours are shown as black lines. The vertical blue bars show the radial extent of the 3D model, at the starting and ending time of the simulations.

is important to go beyond the box-in-a-star setup and towards fully spherical simulations, in order to correctly reproduce the fluid motions especially in case of large convective regions.

A velocity-damping region has been included at the upper domain for $r > 6 \times 10^9$ cm to dissipate the gravity waves, in particular at the beginning of the simulation when the equilibrium state has not been reached yet; no damping could be included at the lower domain due to the close presence of convective regions. Periodic boundary conditions have been implemented in φ, but for θ reflective boundary conditions have been chosen instead. This is justified by the proximity to the polar axis, where periodic conditions are no longer realistic and can create an excess of kinetic energy, therefore it is more physical to assume that the flow cannot cross the axis (see Müller, 2020).

The 12-isotope network employed for energy generation is particularly appropriate for this environment: as explained in Sec. 3.4.5, this network can cover carbon, neon and oxygen burning, which are the most important reactions expected to take place in these convective shells. These events are dynamical enough that it is not required to implement any boosting of the driving luminosity, as it was the case in the previous chapters; this ensures that no artefacts result from changes in the energy generation.

6.2 Dynamics of the shell merging

I present in Table 6.1 the properties of the two hydrodynamic simulations of shell mergers included in this chapter. As explained before, the two simulations are started from the same initial conditions and run for the same time-scale, but with two different geometries, to test the dependence of results on the model setup. As I will show below, the evolution of the two simulations is very similar and in many parts of this chapter, when the analysis is not focused on the differences arising from the geometry, I will only show results from

Table 6.1: Properties of the two hydrodynamic simulations I present in this chapter: model code name; polar angular extent, $\Delta\theta$; azimuthal angular extent, $\Delta\varphi$; radial resolution, N_r; polar angle resolution, N_θ; azimuthal angle resolution, N_φ; ending time of the simulation, $t_{\rm end}$; and finally cost required to run the simulation in CPU core-hours.

name	$\Delta\theta$	$\Delta\varphi$	N_r	N_θ	N_φ	$t_{\rm end}$ (s)	cost (10^6 hr)
a60n256	60°	60°	768	256	256	3000	0.92
a360n1024	90°	360°	512	256	1024	3000	2.44

a360n1024, which is closer to a fully spherical geometry. To better display this, I show in Fig. 6.2 two cross-sections taken from a360n1024, one showing the equatorial plane (top panel) and one showing a vertical plane from two opposite sides of the polar axis (bottom panel). We can clearly see the effects of the geometry on the fluid motions: on the equatorial plane, large-scale structures have the possibility to form thanks to the large radial extent and the 360° range spanned by φ. In the vertical plane instead, large-scale eddies take up the entire domain: this is due to the reflective boundary conditions assumed in θ, that encourage the formation of one large eddy; additional tests show that periodic boundary conditions in θ encourage instead the formation of two large eddies in the same convective region.

We can now study the evolution and merging of the convective shells in the 3D simulations. To have a visual representation similar to the 1D model of Fig. 6.1, I present in Fig. 6.3 the time evolution of the angularly averaged kinetic energy (in colour scale) for the two models a360n1024 (top panel) and a60n256 (bottom panel). Thanks to the log scale applied to the radius, we can clearly identify the different convective shells and track their evolution. The main event in both simulations is the merging of the two outermost shells, the carbon- and the neon-burning shells, around 1200 s (much faster than in 1D), which generates a large increase in kinetic energy due to the burning of the

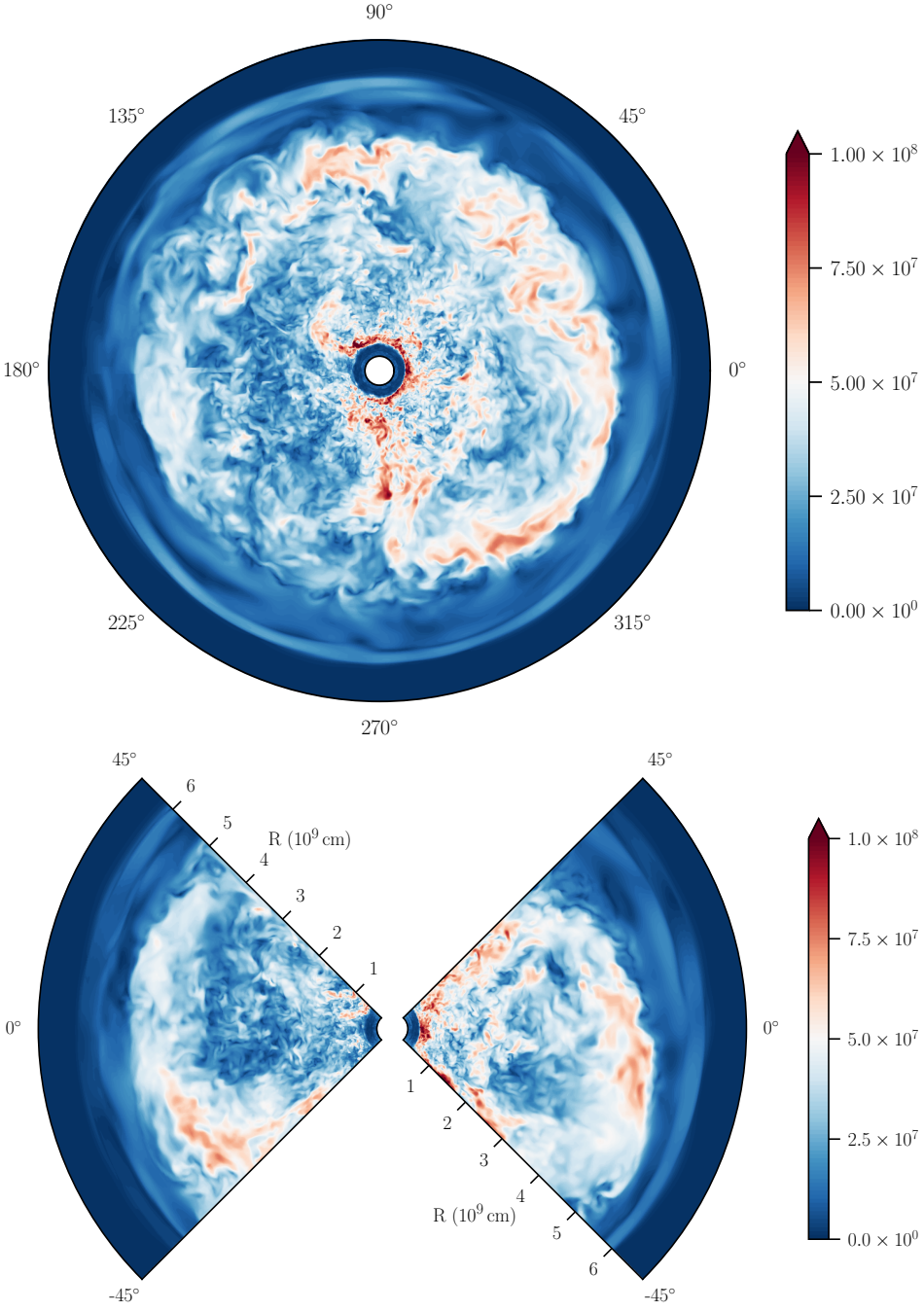

Figure 6.2: Equatorial (top panel) and vertical (bottom panel) cross-sections taken from `a360n1024` at 1500 seconds, with the fluid speed in colour scale in units of cm s^{-1}. The two frames show the 360° range in φ-angle (top) and the two opposite sides of the 90° range in θ-angle (bottom).

freshly engulfed material. The third shell, the oxygen-burning shell, displays a different behaviour: neither it rapidly mixes material with the upper merged shell, nor it effectively burns the fresh fuel producing the large energy release seen in the shell merging. Instead of merging with the other two shells as predicted by the 1D model, the entrainment from the merged shell proceeds slowly due to the strong entropy barrier, and it slowly turns off the nuclear burning in the oxygen shell, as also visible from the energy generation profiles (see Fig. 6.6). This trend is confirmed by a preliminary low-resolution test simulation that has been run up to 10 000 s, and that shows the death of convection in the oxygen-burning shell and the lack of a dynamical merging. However, it cannot be excluded that in the higher resolution simulations presented here a merging would eventually take place, considering that the oxygen shell does not completely die out by the end of the simulations, despite a temporary halt around 1500 s after the first impact with the merging shells above.

The most important difference between the two simulations is the lack in `a60n256` of a second oxygen-burning shell immediately above the lower domain of the model, which is present instead in `a360n1024`. Differently from the other shells, this is the only one that is not present in the initial conditions, but is expected to form afterwards, as visible in Fig. 6.1. The low-resolution test simulation, similar in geometry to `a60n256`, shows that a second oxygen-burning shell does form eventually, but around 4000 s. This delay can be therefore attributed to the "wedge" geometry, that apparently delays the correct development and evolution of the shells. Indeed, the comparison between the two geometries in Fig. 6.3 shows how much smoother the evolution of the shells is in `a360n1024` compared to `a60n256`, where convection in the shells can temporarily fade to reappear later.

The time evolution of the spatially integrated kinetic energy for the hydrodynamic simulations is shown in Fig. 6.4, alongside the same quantity for the 1D input model. `a360n1024` and `a60n256` share a very similar evolution, with

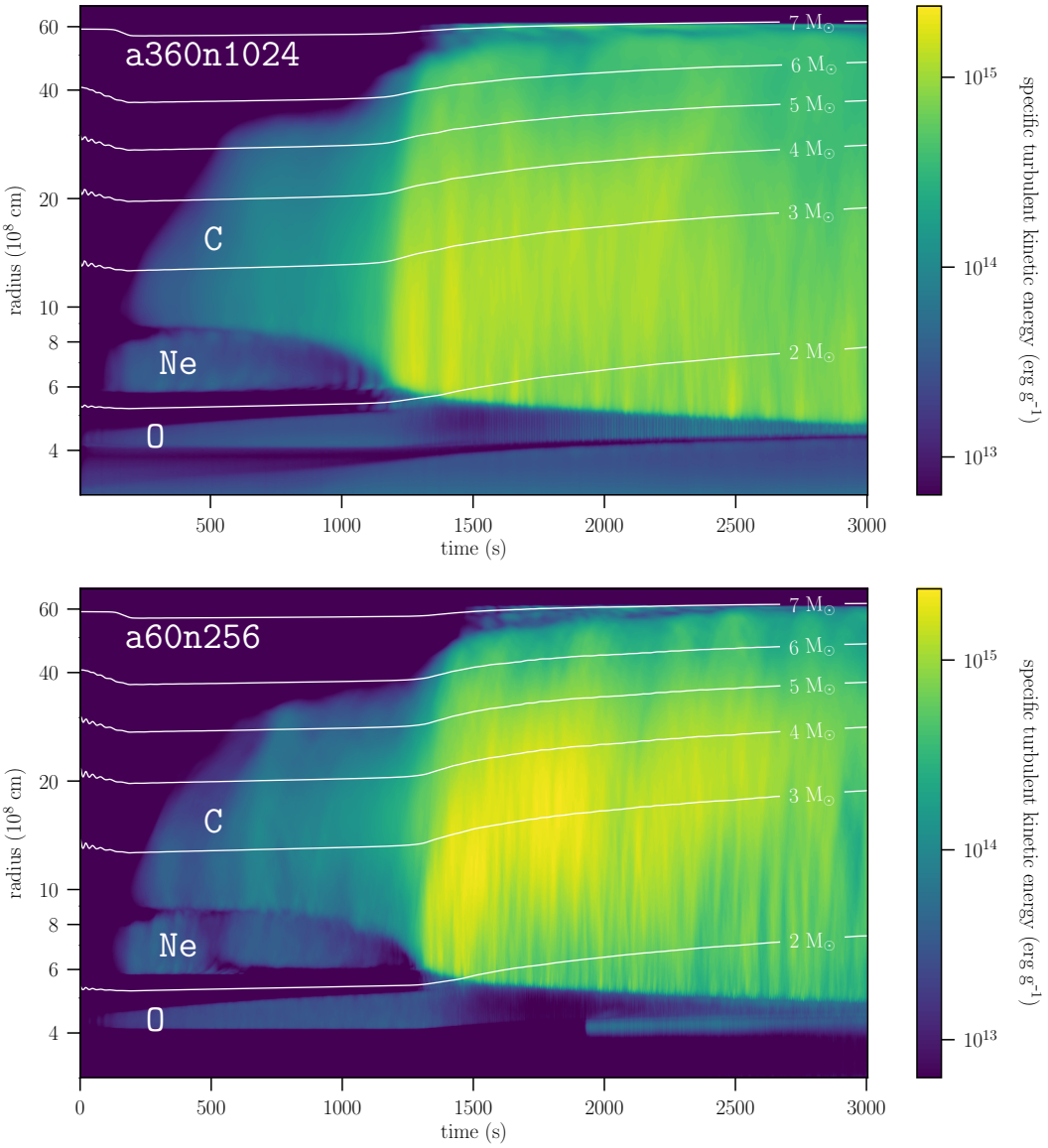

Figure 6.3: Time evolution of the angularly averaged kinetic energy in colour scale for simulations `a360n1024` (top panel) and `a60n256` (bottom panel). Overlaid in white are the isomass contours. The log scale applied to the radius on the y-axis provides a comprehensive view of all the convective shells.

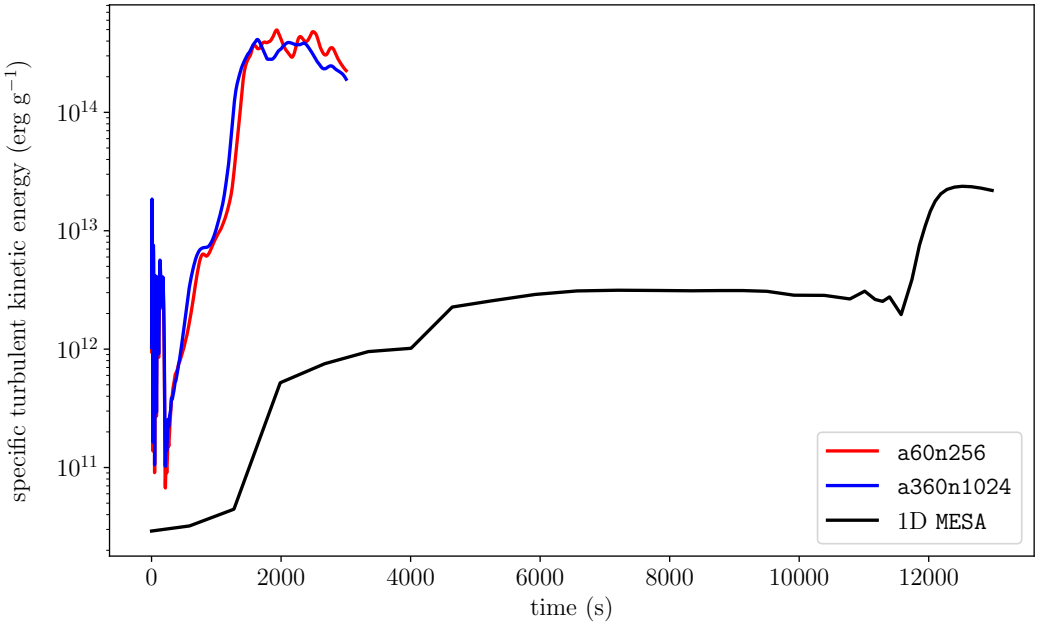

Figure 6.4: Specific turbulent kinetic energy integrated across the entire domain for simulations `a360n1024` and `a60n256` compared to the evolution of the 1D `MESA` model.

sharp increases in kinetic energy after an initial transient, interrupted by two plateaus around 750 and 2000 s right before and after the main merging event, respectively. The 1D model also shares a similar evolution, but on a time-scale that is about 5 times slower; this is the same effect that we have seen and analysed in the simulations of Chapter 5. I concluded in Sec. 5.2.1 that this is due to the closed boundary domains and limited expansion that characterize the 3D simulations; the same seems to be occurring here, despite the large radial extent selected to contain this problem.

As another way of highlighting the differences in geometry between the two simulations, I computed the power spectra of the kinetic energy with 2D Fourier transforms as previously described in Sec. 5.2.2 for a spherical geometry. The results are shown in Fig. 6.5, for `a360n1024` in the top panel and `a60n256` in the bottom panel, at a radius inside the main shell merging

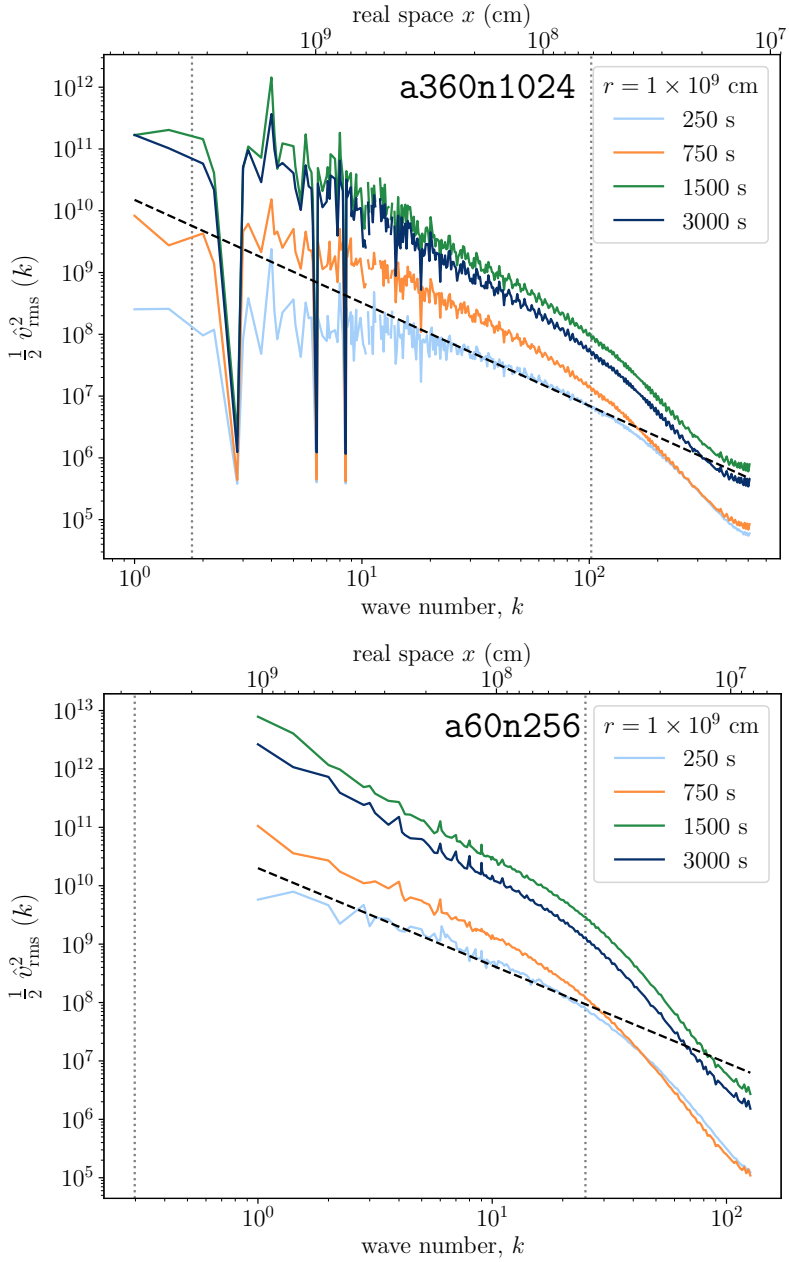

Figure 6.5: Spectra of the specific kinetic energy as function of the wave number k and the real space x, taken at $r = 1 \times 10^9$ cm in the middle of the main shell merging event, for `a360n1024` (top panel) and `a60n256` (bottom panel), at four key time-steps in the simulations (see Table 6.2). The dashed black line is the Kolmogorov scaling $k^{-5/3}$; the vertical dotted line on the left is the average size of the merged shell, and the one on the right is the size of 10 cells.

event. Both spectra follow the expected Kolmogorov scaling at most scales, but the one for `a360n1024` can reach higher k due to its larger number of cell, and larger scales x due to its larger domain. In real space, `a60n256` follows the Kolmogorov scaling for a larger range (4×10^7 - 4×10^8 cm) compared to `a360n1024` (6×10^7 - 4×10^8 cm), due to the higher local resolution of `a60n256` that induces the dissipation at smaller spatial scales. Additionally, some strong absorption frequencies are present in the spectrum of `a360n1024`, but the fact that they stay constant in time and do not appear in `a60n256` gives strong indications that they are an effect of the model geometry, which is close to but not exactly a full sphere.

I focus my attention now on the analysis of `a360n1024`. Table 6.2 shows the convective velocity, radial size and convective turnover time of each shell displayed in Fig. 6.3 for `a360n1024` at four key time-steps, chosen to represent the initial situation with separate shells (250 s), right before and after the merging (750 s and 1500 s), and the final state (3000 s) of the simulation. It is not easy to perform a statistical analysis of convective shells that have such different properties across time and between each other: the carbon and neon merging shells increase their convective velocity by almost one order of magnitude in time, reaching a maximum right after the merging before starting decreasing again. The convective velocity in these shells can be up to 10 times larger than in the oxygen shell. As a result, the convective turnover time assumes a wide range of values across the different shells, requiring attention when choosing the time windows for the statistical analysis.

Some radial profiles from `a360n1024` are shown in Fig. 6.6 at different times throughout the simulation: nuclear energy generation rate (top panel), temperature and entropy (bottom panel). These quantities help us interpret the evolution of the simulations presented in the figures before: the three convective shells at the beginning of the simulation at $r \lesssim 10 \times 10^8$ cm are fuelled by an equal number of peaks in energy generation, but as time passes the two outermost peaks, i.e. the carbon- and neon-burning shells, merge into a single

Table 6.2: Properties of the `a360n1024` shell-merger simulation presented in this chapter, for the three convective shells burning carbon, neon, and oxygen (refer to Fig. 6.3) at different key times in the simulations: convective velocity $v_{\rm rms}$; shell size Δr; convective turnover time $\tau_{\rm c}$. The carbon and neon shells share the same values after the merging.

convective velocity $v_{\rm rms}$ (10^6 cm s^{-1})			
time \ shell	C	Ne	O
250 s	6.81	8.49	6.68
750 s	15.2	7.33	8.41
1500 s	56.4		5.26
3000 s	41.3		–

shell size Δr (10^8 cm)			
time \ shell	C	Ne	O
250 s	5.12	2.28	0.56
750 s	25.7	1.04	0.85
1500 s	46.0		0.44
3000 s	52.0		–

convective turnover time $\tau_{\rm c}$ (s)			
time \ shell	C	Ne	O
250 s	150	53.7	16.8
750 s	338	28.4	20.2
1500 s	163		16.7
3000 s	252		–

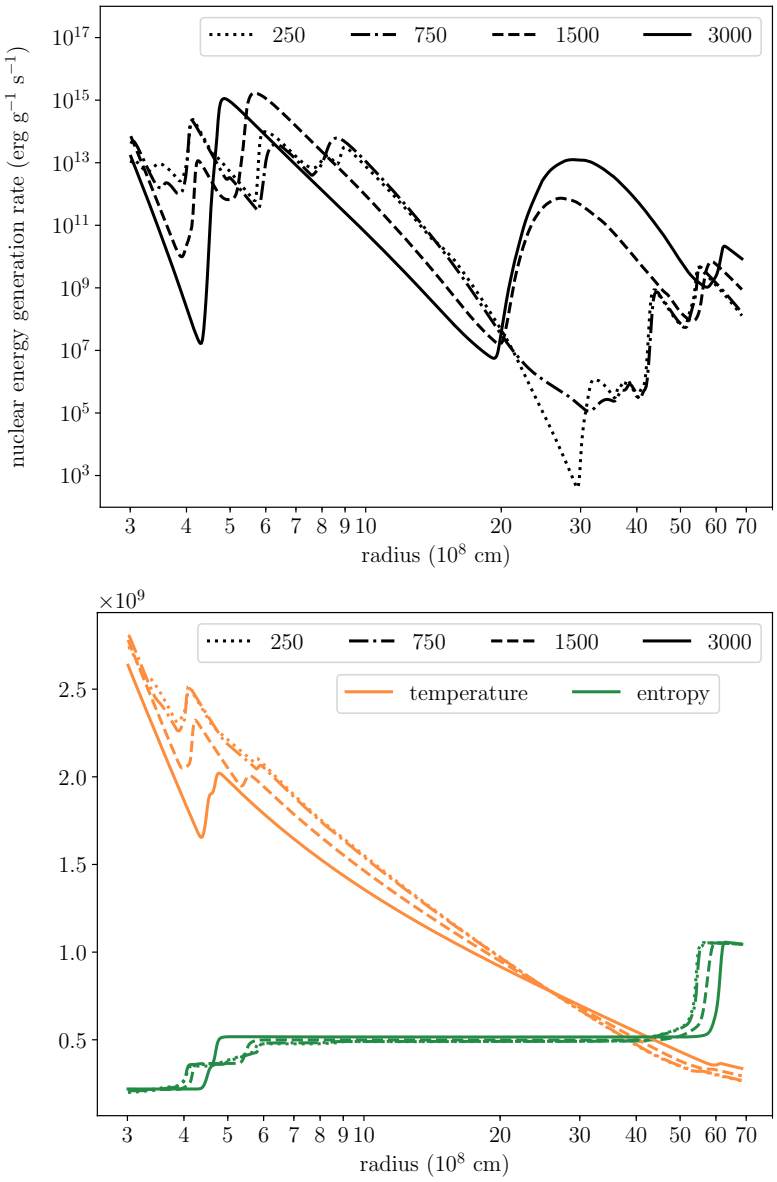

Figure 6.6: Angularly averaged radial profiles from `a360n1024` taken at different times throughout the simulation: nuclear energy generation rate (top panel), temperature and entropy (bottom panel).

larger peak, while the innermost oxygen-burning shell reduces its energy release with time until it completely disappears. This same behaviour is reflected by the evolution of the temperature. Additionally, some nuclear burning starts taking place also in the outer layers after the shells merge ($r > 20 \times 10^8$ cm), due to the entrainment of helium and carbon from the upper layers at $r > 40 \times 10^8$ cm (see Fig. 6.8). This is the same situation reached in the simulation of Mocák et al. (2018), with two different burning shells present within the same convection zone. However, its energy generation is at least two orders of magnitude lower than in the main event, so its contribution is not significant. Finally, the evolution of the entropy profiles shows that the convective shells are dynamical enough to mix entropy rapidly and efficiently.

6.3 Evolution of the chemical composition

As interesting and important as it is to study the evolution of the abundances in these simulations of merging shells, it can also be very challenging to have a clear picture of what exactly is happening across the multiple convective regions, considering the contributions from convective mixing, nuclear burning and entrainment. I will present in this section the time evolution and radial distribution of the chemical abundances in order to provide a description of the nucleosynthesis in the shell merger environment.

In Fig. 6.7, I present the time evolution of ^{12}C, ^{16}O, ^{20}Ne, ^{24}Mg, and ^{28}Si at a radius of 1×10^9 cm, i.e. inside the carbon-burning shell first and the merged shells later, for simulation `a360n1024`. It is not easy to disentangle the two main processes that contribute to the variation of these abundances, which are the nuclear reactions and the radial transport of species. Before the merging event, which occurs around 1200 s, ^{12}C stays relatively constant inside the shell because its consumption is rapidly compensated by the strong convective mixing across the region, while ^{20}Ne slightly decreases due to its consumption and

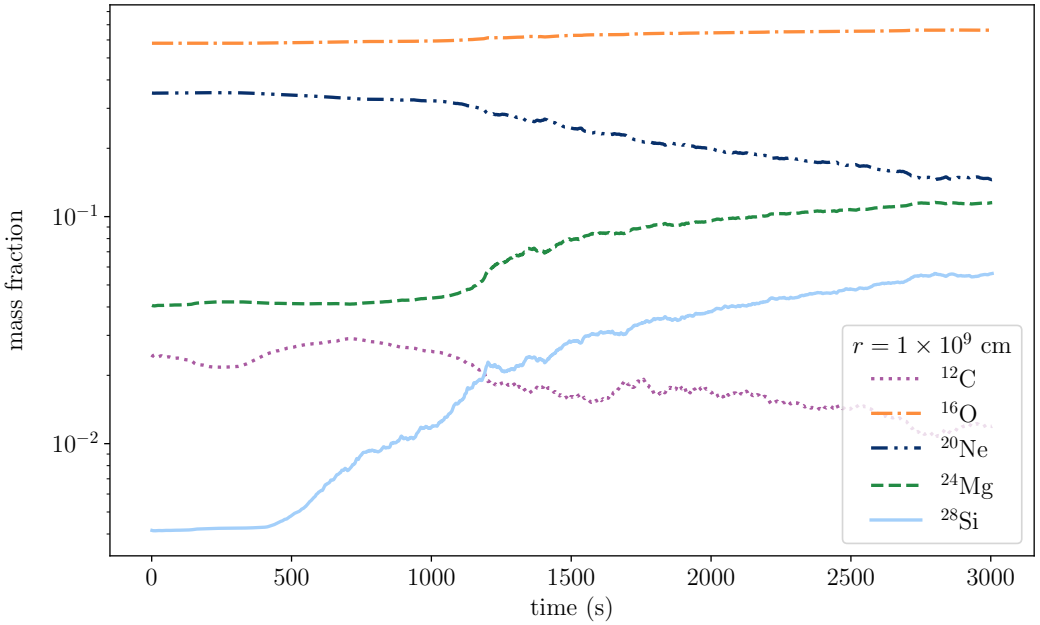

Figure 6.7: Time evolution of the mass fractions of key isotopes at radius 1×10^9 cm, inside the merging shells, throughout simulation `a360n1024`.

transport to the neon-burning region immediately below. ^{16}O, ^{24}Mg and ^{28}Si slightly increase thanks to their production by these reactions. These trends are strongly enhanced after the shell merging ($t \gtrsim 1200$ s), due to the efficient carbon and neon burning that occurs in the newly formed shell; specifically, ^{12}C and ^{20}Ne are more rapidly consumed, leading to a strong production of ^{16}O, ^{24}Mg and ^{28}Si. No destruction of oxygen is observed in this shell.

We can also study the spatial distribution of the isotopes at different time-steps by plotting their angularly averaged radial profiles, as I do in Fig. 6.8 for different combinations of isotopes. From the abundances we can easily identify the three initial convective shells, indicated by the plateaus in ^{16}O between 4 - 5×10^8 cm, in ^{12}C between 9 - 14×10^8 cm, and the gradient in ^{20}Ne (bottom panel) between 6 - 8×10^8 cm due to its fast consumption and mixing. After the merging at $t \sim 1200$ s, a single large plateau is dominating most of the

domain, extending inwards due to entrainment and mixing of material, and decreasing the abundance of ^{12}C and ^{20}Ne due to their burning in the shell, with an increase of ^{16}O and ^{24}Mg as a result. Entrainment of ^{4}He and ^{12}C from the rich upper layers $r > 40 \times 10^8$ cm is also visible in the top panel, contributing to the secondary peak in energy generation visible in Fig. 6.6.

It is also possible to study the radial transport of the isotopes employing the mean-field analysis tools I have introduced in Sec. 3.5.2 and applied in Sec. 5.4. The radial flux profiles, defined as $f_i = \overline{\varrho}\ \widetilde{X_i'' v_r''}$ for a species i, are shown in Figs. 6.9 and 6.10 for the most important isotopes of simulation `a360n1024` at the usual four time-steps. It is very useful to look at the evolution of these quantities, because they represent the mixing of material that brings the fuel towards the burning regions and the ashes away from them. As before, positive and negative values of the flux represent upward and downward transport of species, respectively. At the beginning of the simulation (Fig. 6.9, top panel) the four convective regions are clearly indicated by the peaks and valleys in flux, corresponding to upward and downward transport of ashes and fuel, respectively, as it was the case in the simulations analysed in Sec. 5.4. Specifically, the two innermost shells are burning mainly oxygen to produce silicon, while the central shell between 6 - 8 $\times 10^8$ cm is burning mostly neon to produce oxygen and silicon, and the outermost shell is burning carbon to produce neon. We can see that when the two shells merge (t = 750 - 1500 s, Fig. 6.9 bottom and Fig. 6.10 top), a single convective zone forms in the middle of the domain, and it is burning both neon and carbon to generate oxygen, magnesium and silicon. The magnitude of the flux greatly increases right after the merging, but with time it starts reducing again following the decrease in kinetic energy, as visible in Fig. 6.10, bottom panel.

Finally, I show in Fig. 6.11 the normalized standard deviation profiles of the mass fraction, defined as $\sigma_i/\bar{X}_i = (\widetilde{X_i'' X_i''})^{1/2}/\bar{X}_i$ for a species i, for the same isotopes as before, and at two time-steps before and after the shell merging. It can be challenging to recognise precise shapes in these plots, but neverthe-

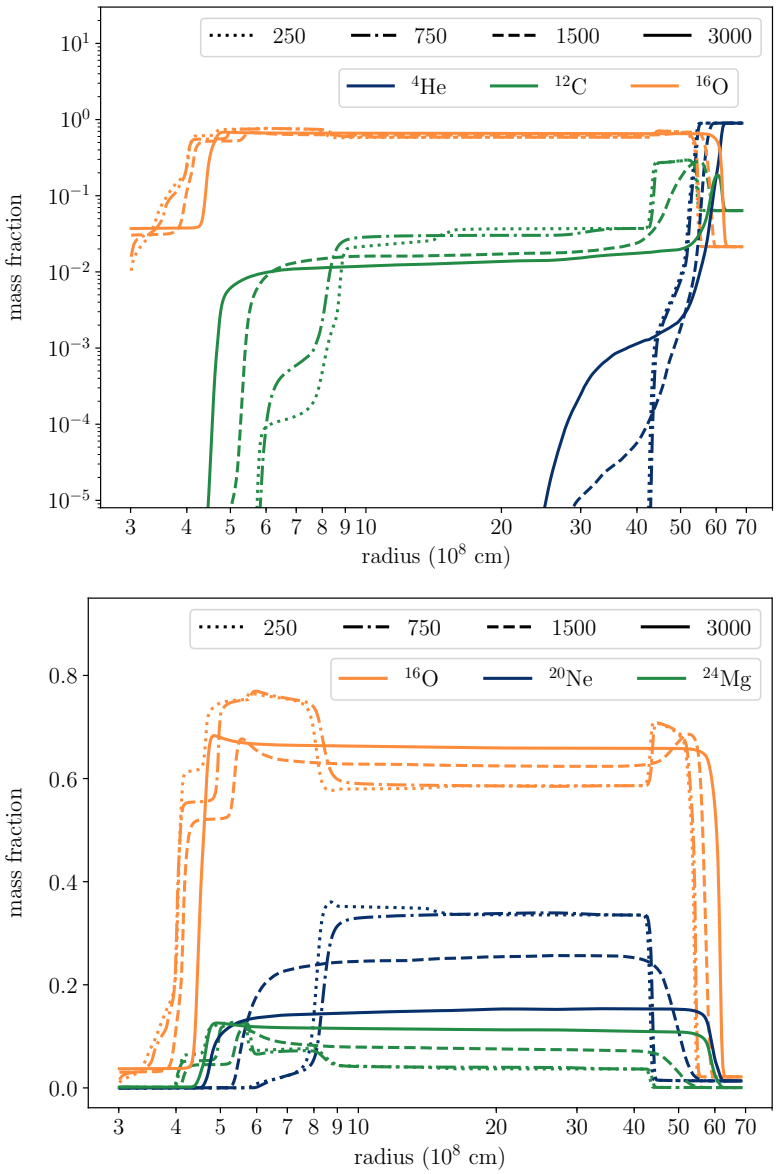

Figure 6.8: Angularly averaged radial profiles of mass fraction, at four key time-steps (different line styles), for simulation `a360n1024`. Top panel: ^{4}He, ^{12}C, ^{16}O in log scale. Bottom panel: ^{16}O, ^{20}Ne, ^{24}Mg in linear scale.

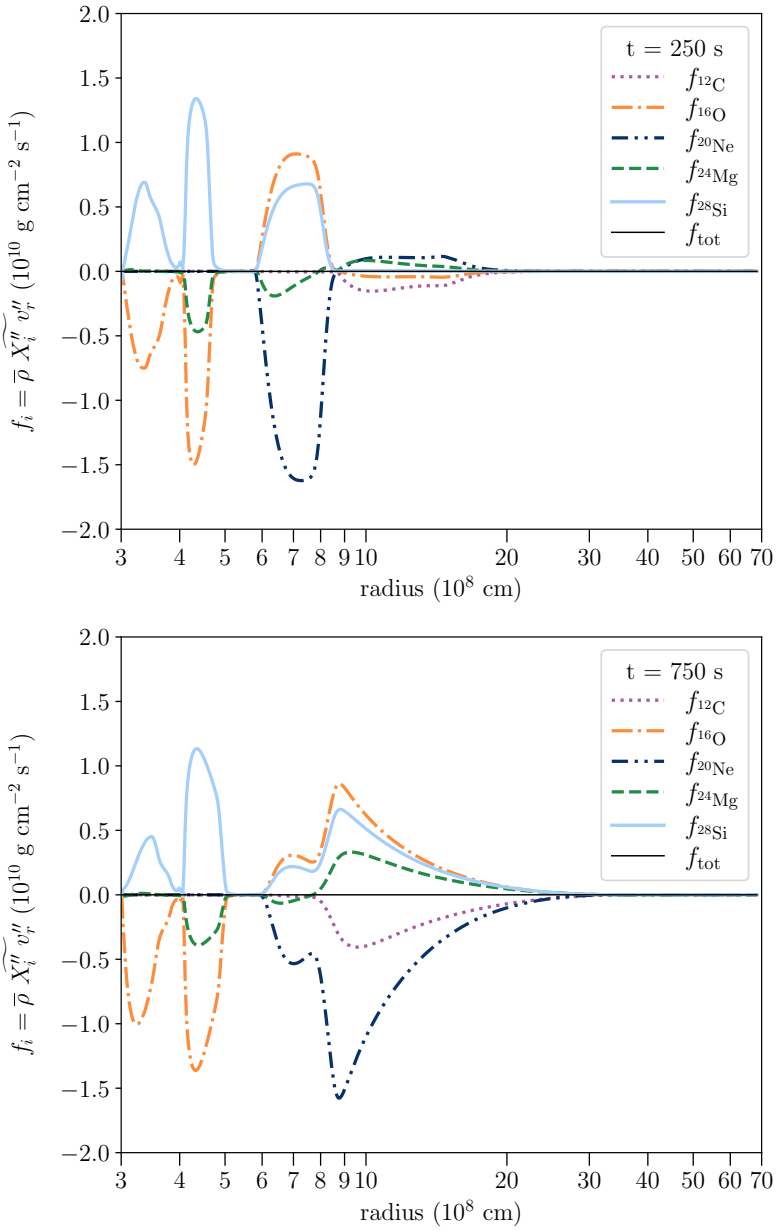

Figure 6.9: Flux profiles of ^{12}C, ^{16}O, ^{20}Ne, ^{24}Mg, and ^{28}Si as a function of the stellar radius, from simulation `a360n1024` at 250 s (top panel) and 750 s (bottom panel), averaged over 150 s and 333 s respectively. The black line is the sum of the flux profiles for all the 12 isotopes in the network.

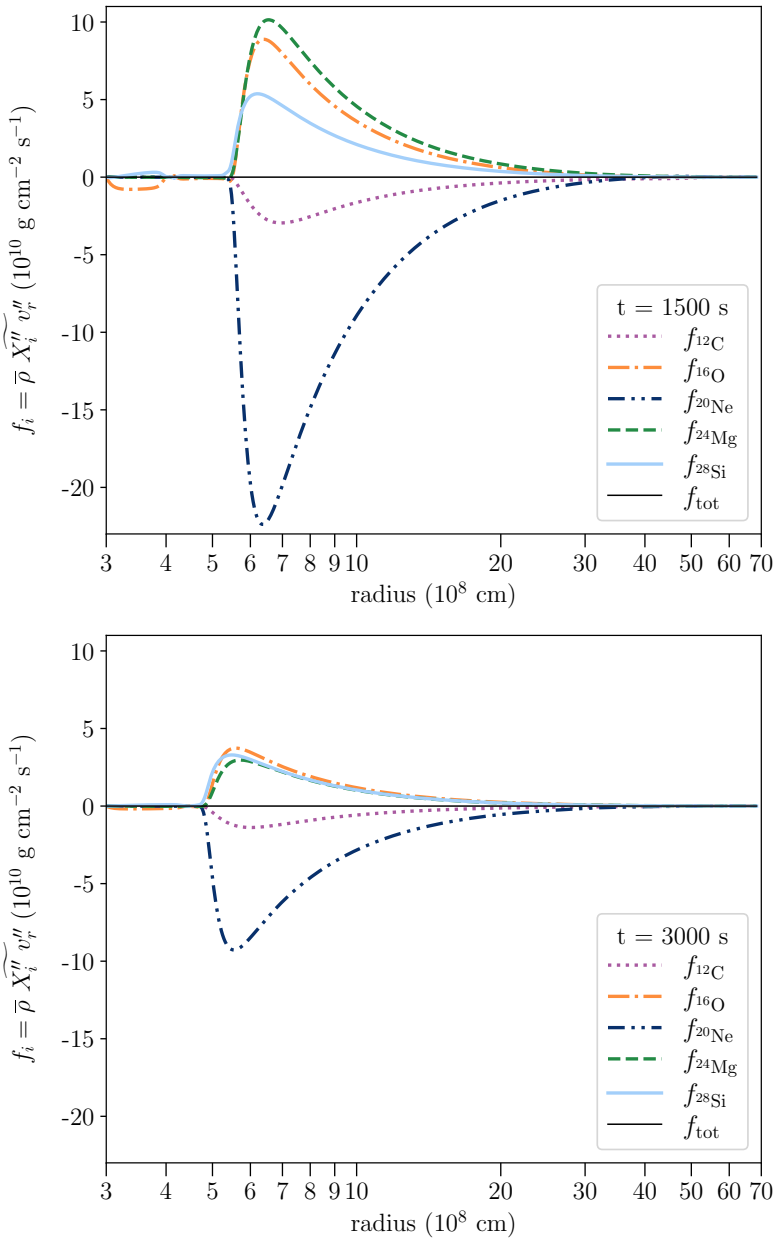

Figure 6.10: Same as Fig. 6.9, but at time 1500 s (top panel) and 3000 s (bottom panel), averaged over 200 s and 500 s respectively.

less they can provide an idea of the magnitude of the chemical dispersion in the layers, i.e. the deviation from spherical symmetry assumed in 1D models. Before the merging, the peaks of normalized dispersion at the shell boundaries can reach up to 200 per cent, but inside the convective carbon-burning region (9 - 14×10^8 cm) they are closer to 10 per cent for carbon and up to a few per cent for the other isotopes. Immediately after the merging, the new peaks in normalized deviation go beyond 300 per cent, and the values inside the merged region have also increased to 30 per cent for carbon and silicon, and at least 10 per cent for neon and magnesium. Overall, these values are rather large, especially if compared to the dispersions from more conventional burning phases like the one simulated in Chapter 5. This is an effect of the highly dynamical environment found in the shell mergers, and it shows the significant impact that these events can have on the nucleosynthesis processes already during the evolution of the star, before the supernova explosion.

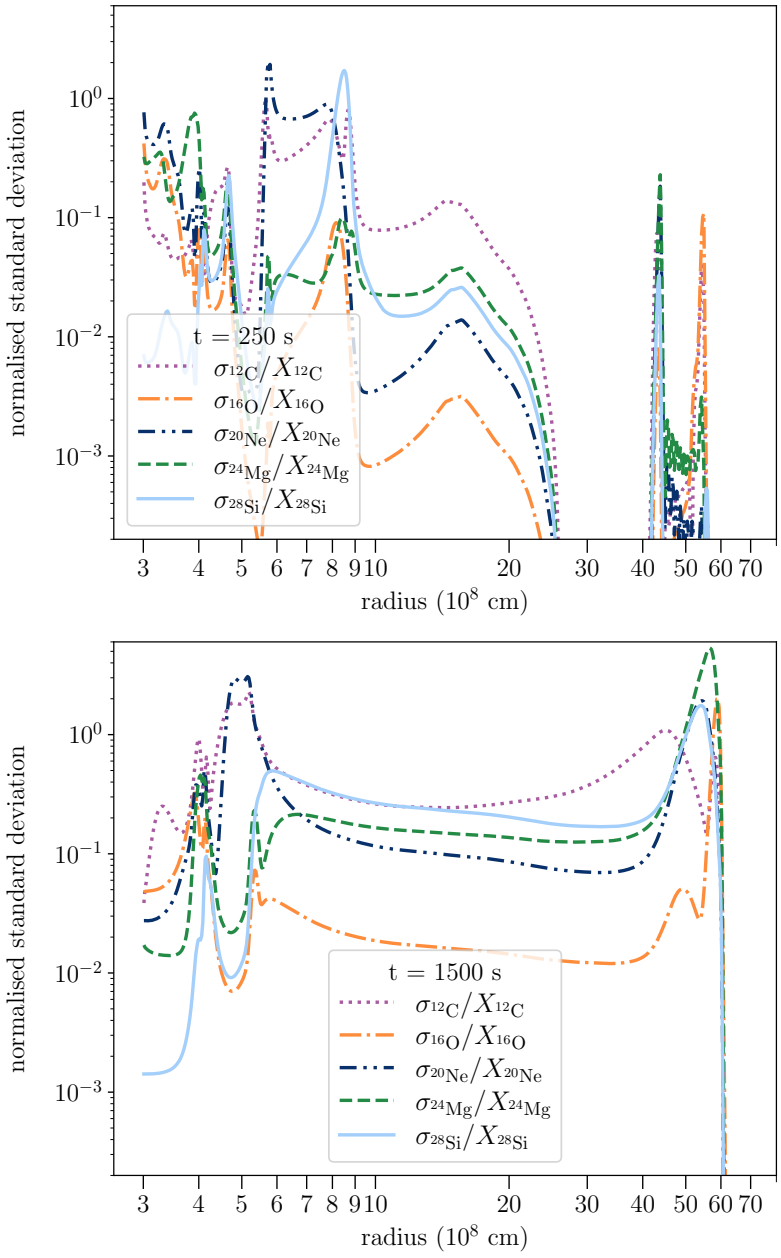

Figure 6.11: Normalized standard deviation profiles of ^{12}C, ^{16}O, ^{20}Ne, ^{24}Mg, and ^{28}Si as a function of the stellar radius, from simulation `a360n1024` at 250 s (top panel) and 1500 s (bottom panel), averaged over 150 s and 200 s respectively.

7 Conclusions and future work

A good understanding of the structure and evolution of massive stars is of crucial importance for many different fields in Astrophysics. This is why it is necessary to improve our knowledge and ability to relate observations to accurate models of stars. This is particularly challenging when it comes to studying the internal structure of stars, since observations are generally limited to the stellar surface and can only give indirect information on the interiors. For massive stars, the question is complicated even more by the fact that towards the end of the stellar life the internal structure is organised in concentric shells with multiple convective regions. Nevertheless, it is important to have a good understanding of these environments, especially for their impact on studies of supernova progenitors and explosion mechanisms, predictions on the nature and physics of the remnant, nucleosynthesis and galactic chemical evolution.
Stellar models represent a precious tool for producing accurate predictions of the structure and evolution of stars. Simulating the complete evolution of an entire star will probably never be possible in more than one dimension, given the high computational cost of multi-dimensional models. Therefore, the 1D models will remain the main tool for predicting and explaining the stellar evolution. Since these models are largely based on simplifying assumptions that reproduce the complex multi-D processes inside stars, it is crucial that the physics implemented is always accurate and up to date. Nowadays, there are still many uncertainties related to these processes, with one of the most important being the extent of convective zones in stellar interiors.
More light on these uncertainties can be shed by multi-D simulations of specific parts of the stellar interiors, produced employing numerical models. The results can give very detailed information on the dynamics of the stellar convective layers, improving the physics and parametrization of 1D models. However, multi-D models are computationally very expensive, so it is difficult to

reproduce a significant portion of the stellar lifetime in more than one dimension. Therefore, it is the interplay between 1D and multi-D models that really pushes forwards our knowledge of stellar evolution.

In this thesis, I presented the results of different sets of hydrodynamic simulations, run and analysed with the goal of improving the understanding of turbulent dynamics and nucleosynthesis in evolved massive stars. Three different environments have been explored: a neon-burning shell from a 15 $M_\odot$ star in Chapter 4, a neon-burning shell from a 20 $M_\odot$ star in Chapter 5, and a shell merging event from a 20 $M_\odot$ star in Chapter 6. Each of these scenarios has been studied to probe different aspects of the stellar evolution, and the conclusions drawn are diverse and of general interest for stellar evolution theory and other fields of Astrophysics.

The convective neon shell simulated in Chapter 4 (Rizzuti et al., 2022) is one of the few cases in the literature of 3D stellar simulations at nominal luminosity, i.e. the energy generation has not been altered. As a burning phase, the neon burning is still distant from the final collapse of the star. The simulations clearly show the evolution of the convective zone and its growth in time due to entrainment of material from the stable regions. Having run multiple simulations from the same initial conditions but with different luminosity boosting, and having extracted the entrainment rates from both the upper and lower convective boundaries, I parametrized entrainment with a simple law that can be used for 1D models. The law is consistent with previous parametrizations from hydrodynamic simulations, but not with the results from 1D stellar evolution models. This is a well-known problem in stellar evolution theory, but the new simulations presented here show that the large entrainment rates found by multi-D models are not an effect of the luminosity boosting, but a natural result of the turbulent dynamics.

The simulations presented in Chapter 5 (Rizzuti et al., 2023) have been started instead from initial conditions assumed from a "321D-guided" stellar model, which includes overshooting prescriptions that are stronger than what is nor-

mally used in these models. A neon-burning shell from this 1D model has been simulated in 3D until the complete exhaustion of fuel and the death of convection. The simulations, that as in the previous case have been run with and without boosted luminosity, show again large entrainment rates, but the entrainment law parametrized from these data is significantly more in agreement with the measurements from 1D models of main-sequence stars. This finding is a promising sign of convergence in overshooting prescriptions between 1D and multi-D models. Additionally, abundance variations have been studied in these simulations, showing strong radial fluxes that transport species across the convective zone, but only a modest dispersion of species as a function of the radius.

Finally, I presented in Chapter 6 simulations of a more peculiar event, the merging of two convective shells into a larger one. This scenario is of great interest for the evolution of the stellar structure towards its final phases and the nucleosynthesis paths that it can enable. Initial conditions were assumed from the "321D-guided" stellar model that predicts the merging of multiple convective shells. The corresponding 3D simulations confirm the merging of a carbon-burning with a neon-burning shell, with a strong increase of the fluid kinetic energy. The new merged shell becomes an important site for nucleosynthesis, presenting an efficient nuclear burning of both carbon and neon. The dispersion of species as a function of the radius is very large as a result of the highly dynamical environment. Additionally, these simulations have been run with two different geometries to compare the effects on the results, concluding that moving towards a full 4π setup encourages a smoother evolution of convective regions on large scales.

Future research will make further progress in understanding the processes that occur in stellar interiors. 1D stellar evolution models will need to revise their modelling of convection, in particular concerning the size of convective zones, which are found to be larger than current implementations by numerical simulations. This issue also encompasses the question of what shape the con-

vective boundaries should have in 1D, since 3D results show the mixing of both chemical composition and entropy. On the other hand, multi-D hydrodynamic simulations of stellar interiors still need to improve the realism of the environments they simulate. Recent studies are starting implementing solver schemes for magnetohydrodynamic equations (Varma & Müller, 2021; Leidi et al., 2022), allowing the simulations to include magnetic fields coming from dynamo effects; this will put important constraints on the amount of kinetic energy and turbulent motions that the fluid can build up. Additionally, recent works are showing that a continuously increasing number of chemical species can be now included directly into the numerical simulations (Couch et al., 2015; Müller et al., 2016; Mocák et al., 2018; Yoshida et al., 2019), contributing to the energy release and the production of new species; this is extremely interesting for studies of nucleosynthesis and galactic chemical evolution. My work also shows that the model geometry can have an impact on the evolution of the simulations, therefore employing a fully spherical geometry should be preferred in the cases when convection occurs on large scales. Finally, with the advent of large computing facilities, new types of processing units, and progress in numerical solver schemes, it will be possible to run simulations of stellar interiors with increasing resolution and time-scales. This will allow to have more detailed predictions of the fluid motions and their evolution in time. There are several aspects I would like to explore further to continue the work of this thesis. Given the large uncertainties of convection and convective boundary mixing linked to the extrapolation from boosted-luminosity simulations, it will be crucial to extend the repository of hydrodynamic simulations run at nominal luminosity, in order to better understand the impact of the boosting on the stellar physics. This can include late stellar burning phases such as carbon, neon or oxygen burning. Additionally, it would be also important to further improve and extend the implementation of explicit nuclear networks into hydrodynamic codes, which is particularly interesting for the late burning phases characterized by different nuclear species contributions. This will allow

me to study not only the nucleosynthesis in multi-D stellar environments, but also the evolution of convection over a nuclear burning time-scale. Finally, I would be interested in investigating the effects of magnetic fields on convection, employing magnetohydrodynamic simulations that include amplification effects from the small-scale dynamo mechanism. I expect magnetic fields to influence the fluid motions by damping the velocities on small scales through the Lorentz force; this will cast new light on the effects of magnetic fields on stellar convection and convective boundary mixing.

Considering these premises, the road ahead seems to hold many stimulating challenges and exciting possibilities for future research on stellar modelling, and additional simulations and analysis will further broaden our knowledge of the life and death of stars.

Bibliography

Aerts C., Mathis S., Rogers T. M., 2019, ARA&A, 57, 35

Anders E. H., Pedersen M. G., 2023, Galaxies, 11

Andrassy R., Herwig F., Woodward P., Ritter C., 2020, MNRAS, 491, 972

Andrassy R., et al., 2022, A&A, 659, A193

Andrassy R., Leidi G., Higl J., Edelmann P. V. F., Schneider F. R. N., Roepke F. K., 2023, preprint (arXiv:2307.04068)

Arnett D., 1996, Supernovae and Nucleosynthesis: An Investigation of the History of Matter from the Big Bang to the Present, Princeton Univ. Press, Princeton, NJ

Arnett W. D., Meakin C., 2016, Rep. Prog. Phys., 79, 102901

Arnett W. D., Thielemann F. K., 1985, ApJ, 295, 589

Arnett D., Meakin C., Young P. A., 2009, ApJ, 690, 1715

Arnett W. D., et al., 2018, preprint (arXiv:1810.04659)

Asplund M., Grevesse N., Sauval A. J., Scott P., 2009, ARA&A, 47, 481

Baraffe I., Pratt J., Goffrey T., Constantino T., Folini D., Popov M. V., Walder R., Viallet M., 2017, ApJ, 845, L6

Baraffe I., et al., 2023, MNRAS, 519, 5333

Battino U., et al., 2016, ApJ, 827, 30

Beaudet G., Petrosian V., Salpeter E. E., 1967, ApJ, 150, 979

Berberich J. P., Chandrashekar P., Klingenberg C., 2021, Computers & Fluids, 219, 104858

Bethe H. A., 1990, Rev. Mod. Phys., 62, 801

Bethe H. A., Brown G. E., Applegate J., Lattimer J. M., 1979, Nuclear Phys. A, 324, 487

Biermann L., 1932, Z. Astrophys., 5, 117

Böhm-Vitense E., 1958, Z. Astrophys., 46, 108

Bowman D. M., 2020, Frontiers Astron. Space Sci., 7, 70

Bowman D. M., et al., 2019a, Nature Astronomy, 3, 760

Bowman D. M., et al., 2019b, A&A, 621, A135

Brott I., et al., 2011, A&A, 530, A115

Browning M. K., 2008, ApJ, 676, 1262

Browning M. K., Brun A. S., Toomre J., 2004, ApJ, 601, 512

Brummell N. H., Clune T. L., Toomre J., 2002, ApJ, 570, 825

Burns K. J., Vasil G. M., Oishi J. S., Lecoanet D., Brown B. P., 2020, Phys. Rev. Res., 2, 023068

Burrows A., Vartanyan D., 2021, Nature, 589, 29

Castro N., Fossati L., Langer N., Simón-Díaz S., Schneider F. R. N., Izzard R. G., 2014, A&A, 570, L13

Cescutti G., Matteucci F., Caffau E., François P., 2012, A&A, 540, A33

Cescutti G., Chiappini C., Hirschi R., Meynet G., Frischknecht U., 2013, A&A, 553, A51

Chabrier G., Baraffe I., 1997, A&A, 327, 1039

Chandrasekhar S., 1931, ApJ, 74, 81

Chandrasekhar S., 1935, MNRAS, 95, 207

Chandrasekhar S., 1961, Hydrodynamic and hydromagnetic stability, Oxford: Clarendon

Christensen U., et al., 2001, Phys. Earth Planet. Int., 128, 25

Claret A., Torres G., 2016, A&A, 592, A15

Clarke C., Carswell B., 2007, Principles of Astrophysical Fluid Dynamics, Cambridge University Press

Clune T., Elliott J., Miesch M., Toomre J., Glatzmaier G., 1999, Parallel Computing, 25, 361

Colella P., Glaz H. M., 1985, J. Comput. Phys., 59, 264

Colella P., Woodward P. R., 1984, J. Comput. Phys., 54, 174

Colgate S. A., White R. H., 1966, ApJ, 143, 626

Colgate S. A., Grasberger W. H., White R. H., 1961, AJ, 66, 280

Couch S. M., Ott C. D., 2015, ApJ, 799, 5

Couch S. M., Chatzopoulos E., Arnett W. D., Timmes F. X., 2015, ApJ, 808, L21

Courant R., Friedrichs K., Lewy H., 1928, Math. Ann., 100, 32

Cristallo S., Straniero O., Gallino R., Piersanti L., Domínguez I., Lederer M. T., 2009, ApJ, 696, 797

Cristini A., Meakin C., Hirschi R., Arnett D., Georgy C., Viallet M., Walkington I., 2017, MNRAS, 471, 279

Cristini A., Hirschi R., Meakin C., Arnett D., Georgy C., Walkington I., 2019, MNRAS, 484, 4645

Cyburt R. H., et al., 2010, ApJS, 189, 240

de Jager C., Nieuwenhuijzen H., van der Hucht K. A., 1988, A&AS, 72, 259

Durst F., Ünsal B., 2006, J. Fluid Mech., 560, 449

Edelmann P. V. F., Horst L., Berberich J. P., Andrassy R., Higl J., Leidi G., Klingenberg C., Röpke F. K., 2021, A&A, 652, A53

Eggenberger P., Meynet G., Maeder A., Hirschi R., Charbonnel C., Talon S., Ekström S., 2008, Ap&SS, 316, 43

Ekström S., et al., 2012, A&A, 537, A146

Featherstone N. A., Hindman B. W., 2016, ApJ, 818, 32

Fernando H. J. S., 1991, Annu. Rev. Fluid Mech., 23, 455

Fewell M. P., 1995, American Journal of Physics, 63, 653

Freytag B., Ludwig H. G., Steffen M., 1996, A&A, 313, 497

Fryxell B., Müller E., Arnett D., 1989, in Hydrodynamics and nuclear burning, Max-Planck-Institut für Physik und Astrophysik, 449

Fryxell B., et al., 2000, ApJS, 131, 273

Garaud P., 2018, Annual Review of Fluid Mechanics, 50, 275

Garnier E., Adams N., Sagaut P., 2009, Large Eddy Simulation for Compressible Flows, Springer, Dordrecht

Ghosal S., 1996, Journal of Computational Physics, 125, 187

Gilet C., Almgren A. S., Bell J. B., Nonaka A., Woosley S. E., Zingale M., 2013, ApJ, 773, 137

Godunov S. K., Bohachevsky I., 1959, Matematičeskij sbornik, 47(89), 271

Hayashi C., 1961, PASJ, 13, 450

Heger A., Woosley S. E., 2002, ApJ, 567, 532

Henyey L. G., Wilets L., Böhm K. H., Lelevier R., Levee R. D., 1959, ApJ, 129, 628

Herwig F., 2000, A&A, 360, 952

Herwig F., Freytag B., Fuchs T., Hansen J. P., Hueckstaedt R. M., Porter D. H., Timmes F. X., Woodward P. R., 2007, in Kerschbaum F., Charbonnel C., Wing R. F., eds, ASP Conf. Ser. Vol. 378, Why Galaxies Care About AGB Stars: Their Importance as Actors and Probes. p. 43

Herwig F., Pignatari M., Woodward P. R., Porter D. H., Rockefeller G., Fryer C. L., Bennett M., Hirschi R., 2011, ApJ, 727, 89

Herwig F., Woodward P. R., Lin P.-H., Knox M., Fryer C., 2014, ApJ, 792, L3

Herwig F., et al., 2023, MNRAS, stad2157

Hirschi R., Meynet G., Maeder A., 2004, A&A, 425, 649

Horst L., Hirschi R., Edelmann P. V. F., Andrássy R., Röpke F. K., 2021, A&A, 653, A55

Hoyle F., 1954, ApJS, 1, 121

Hurlburt N. E., Toomre J., Massaguer J. M., Zahn J.-P., 1994, ApJ, 421, 245

Janka H.-T., Melson T., Summa A., 2016, Annual Review of Nuclear and Particle Science, 66, 341

Jermyn A. S., Anders E. H., Lecoanet D., Cantiello M., 2022, ApJS, 262, 19

Jones S., Hirschi R., Pignatari M., Heger A., Georgy C., Nishimura N., Fryer C., Herwig F., 2015, MNRAS, 447, 3115

Jones S., Andrassy R., Sandalski S., Davis A., Woodward P., Herwig F., 2017, MNRAS, 465, 2991

Kageyama A., Sato T., 2004, Geochemistry Geophysics Geosystems, 5, 9

Kaiser E. A., Hirschi R., Arnett W. D., Georgy C., Scott L. J. A., Cristini A., 2020, MNRAS, 496, 1967

Kippenhahn R., Weigert A., Weiss A., 2012, Stellar Structure and Evolution, Springer, Berlin

Kolmogorov A., 1941, Akademiia Nauk SSSR Doklady, 30, 301

Landau L. D., Lifshitz E. M., 1987, Fluid Mechanics, Butterworth-Heinemann

Langanke K., et al., 2003, Phys. Rev. Lett., 90, 241102

Ledoux P., 1947, ApJ, 105, 305

Leidi G., Birke C., Andrassy R., Higl J., Edelmann P. V. F., Wiest G., Klingenberg C., Röpke F. K., 2022, A&A, 668, A143

Lentz E. J., et al., 2015, ApJ, 807, L31

LeVeque R. J., 2002, Finite Volume Methods, Cambridge University Press

Liebendörfer M., Mezzacappa A., Thielemann F.-K., Messer O. E., Hix W. R., Bruenn S. W., 2001, Phys. Rev. D, 63, 103004

Limongi M., Straniero O., Chieffi A., 2000, ApJS, 129, 625

Ludwig H.-G., Freytag B., Steffen M., 1999, A&A, 346, 111

Maeder A., 1975, A&A, 43, 61

Maeder A., Meynet G., 1989, A&A, 210, 155

Matteucci F., 2012, Chemical Evolution of Galaxies, Astronomy and Astrophysics Library, Springer-Verlag, Berlin, Heidelberg

Meakin C. A., Arnett D., 2007, ApJ, 667, 448

Miczek F., 2013, Dissertation, Technische Universität München, Germany

Mocák M., Campbell S. W., Müller E., Kifonidis K., 2010, A&A, 520, A114

Mocák M., Meakin C., Viallet M., Arnett D., 2014, preprint (arXiv:1401.5176)

Mocák M., Meakin C., Campbell S. W., Arnett W. D., 2018, MNRAS, 481, 2918

Müller B., 2020, Living Reviews in Computational Astrophysics, 6, 3

Myra E. S., Bludman S. A., 1989, ApJ, 340, 384

Müller B., 2015, MNRAS, 453, 287

Müller E., Steinmetz M., 1995, Computer Physics Communications, 89, 45

Müller B., Viallet M., Heger A., Janka H.-T., 2016, ApJ, 833, 124

Müller B., Melson T., Heger A., Janka H.-T., 2017, MNRAS, 472, 491

Nugis T., Lamers H. J. G. L. M., 2000, A&A, 360, 227

O'Connor E., Ott C. D., 2011, ApJ, 730, 70

Oppenheimer J. R., Volkoff G. M., 1939, Physical Review, 55, 374

Pavelyev A. A., Reshmin A. I., Teplovodskii S. K., Fedoseev S. G., 2003, Fluid Dynamics, 38, 545

Paxton B., Bildsten L., Dotter A., Herwig F., Lesaffre P., Timmes F., 2011, ApJS, 192, 3

Paxton B., et al., 2013, ApJS, 208, 4

Paxton B., et al., 2018, ApJS, 234, 34

Paxton B., et al., 2019, ApJS, 243, 10

Pedersen M. G., et al., 2021, Nature Astronomy, 5, 715

Phillips A. C., 1994, The physics of stars, John Wiley & Sons, New York

Rauscher T., Heger A., Hoffman R. D., Woosley S. E., 2002, ApJ, 576, 323

Renzini A., 1987, A&A, 188, 49

Reynolds O., 1883, Philosophical Transactions of the Royal Society of London Series I, 174, 935

Ritter C., Andrassy R., Côté B., Herwig F., Woodward P. R., Pignatari M., Jones S., 2018, MNRAS, 474, L1

Rizzuti F., Cescutti G., Matteucci F., Chieffi A., Hirschi R., Limongi M., 2019, MNRAS, 489, 5244

Rizzuti F., Cescutti G., Matteucci F., Chieffi A., Hirschi R., Limongi M., Saro A., 2021, MNRAS, 502, 2495

Rizzuti F., Hirschi R., Georgy C., Arnett W. D., Meakin C., Murphy A. S., 2022, MNRAS, 515, 4013

Rizzuti F., Hirschi R., Arnett W. D., Georgy C., Meakin C., Murphy A. S., Rauscher T., Varma V., 2023, MNRAS, 523, 2317

Roberti L., Pignatari M., Psaltis A., Sieverding A., Mohr P., Fülöp Z., Lugaro M., 2023, A&A, 677, A22

Rogers T. M., Lin D. N. C., McElwaine J. N., Lau H. H. B., 2013, ApJ, 772, 21

Rolfs C. E., Rodney W. S., 1988, Cauldrons in the Cosmos, Chicago University Press

Roxburgh I. W., 1978, A&A, 65, 281

Roxburgh I. W., 1989, A&A, 211, 361

Salaris M., Cassisi S., 2005, Evolution of Stars and Stellar Populations, John Wiley & Sons, New York

Schaller G., Schaerer D., Meynet G., Maeder A., 1992, A&AS, 96, 269

Schwarzschild M., 1958, Structure and Evolution of Stars, Princeton University Press

Scott L. J. A., Hirschi R., Georgy C., Arnett W. D., Meakin C., Kaiser E. A., Ekström S., Yusof N., 2021, MNRAS, 503, 4208

Shaviv G., Salpeter E. E., 1973, ApJ, 184, 191

Shu F., 1982, The Physical Universe: An Introduction to Astronomy, University Science Books, Herndon

Singh H. P., Roxburgh I. W., Chan K. L., 1995, A&A, 295, 703

Skinner M. A., Dolence J. C., Burrows A., Radice D., Vartanyan D., 2019, ApJS, 241, 7

Smartt S. J., Eldridge J. J., Crockett R. M., Maund J. R., 2009, MNRAS, 395, 1409

Staritsin E. I., 2013, Astronomy Reports, 57, 380

Stothers R. B., Chin C.-W., 1992, ApJ, 390, 136

Straniero O., Chieffi A., Limongi M., Busso M., Gallino R., Arlandini C., 1997, ApJ, 478, 332

Thielemann F. K., Arnett W. D., 1985, ApJ, 295, 604

Timmes F. X., Arnett D., 1999, ApJS, 125, 277

Timmes F. X., Swesty F. D., 2000, ApJS, 126, 501

Townsend R. H. D., Teitler S. A., 2013, MNRAS, 435, 3406

Tur C., Heger A., Austin S. M., 2007, ApJ, 671, 821

Varma V., Müller B., 2021, MNRAS, 504, 636

Viallet M., Meakin C., Arnett D., Mocák M., 2013, ApJ, 769, 1

Viallet M., Meakin C., Prat V., Arnett D., 2015, A&A, 580, A61

Viallet M., Goffrey, T. Baraffe, I. Folini, D. Geroux, C. Popov, M. V. Pratt, J. Walder, R. 2016, A&A, 586, A153

Vink J. S., de Koter A., Lamers H. J. G. L. M., 2000, A&A, 362, 295

Vink J. S., de Koter A., Lamers H. J. G. L. M., 2001, A&A, 369, 574

Weaver T. A., Zimmerman G. B., Woosley S. E., 1978, ApJ, 225, 1021

Wongwathanarat A., Hammer N. J., Müller E., 2010, A&A, 514, A48

Woodward P. R., Herwig F., Lin P.-H., 2014, ApJ, 798, 49

Woosley S. E., Bloom J. S., 2006, ARA&A, 44, 507

Woosley S., Janka T., 2005, Nature Physics, 1, 147

Woosley S. E., Heger A., Weaver T. A., 2002, Rev. Mod. Phys., 74, 1015

Yoshida T., Takiwaki T., Kotake K., Takahashi K., Nakamura K., Umeda H., 2019, ApJ, 881, 16

Yoshida T., Takiwaki T., Aguilera-Dena D. R., Kotake K., Takahashi K., Nakamura K., Umeda H., Langer N., 2021, MNRAS, 506, L20

Zahn J. P., 1991, A&A, 252, 179